“I believe in intuition and inspiration. Imagination is more important than knowledge. For knowledge is limited, whereas imagination embraces the entire world, stimulating progress, giving birth to evolution. It is, strictly speaking, a real factor in scientific research”

Albert Einstein

University of Alberta

Anode materials for H_2S containing feeds in a solid oxide fuel cell

by

Milad Roushanafshar

A thesis submitted to the Faculty of Graduate Studies and Research
in partial fulfillment of the requirements for the degree of

Doctor of Philosophy

in

Materials Engineering

Chemical and Materials Engineering

Spring 2013
Edmonton, Alberta

Abstract

SOFCs which can directly operate under high concentration of H_2S would be economically beneficial as this reduces the cost of gas purification. H_2S is highly reactive gas specie which can poison most of the conventional catalysts. As a result, developing anode materials which can tolerate high concentrations of H_2S and also display high activity toward electrochemical oxidation of feed is crucial and challenging for this application.

The performance of $La_{0.4}Sr_{0.6}TiO_{3\pm\delta}$-$Y_{0.2}Ce_{0.8}O_{2-\delta}$ (LST-YDC) composite anodes in solid oxide fuel cells significantly improved when 0.5% H_2S was present in syngas (40% H_2, 60% CO) or hydrogen. Gas chromatography and mass spectrometry analyses revealed that the rate of electrochemical oxidation of all fuel components improved when H_2S containing syngas was present in the fuel. Electrochemical stability tests performed under potentiostatic condition showed that there was no power degradation for different feeds, and that there was power enhancement when 0.5% H_2S was present in various feeds. The mechanism of performance improvement by H_2S was discussed.

Active anodes were synthesized via wet chemical impregnation of different amounts of $La_{0.4}Ce_{0.6}O_{1.8}$ (LDC) and $La_{0.4}Sr_{0.6}TiO_3$ (L4ST) into porous yttria-stabilized zirconia (YSZ). Co-impregnation of LDC with LS4T significantly improved the performance of the cell from 48 $mW.cm^{-2}$ (L4ST) to 161 $mW.cm^{-2}$ (LDC-L4ST) using hydrogen as fuel at 900 °C. The contribution of LDC to this improvement was investigated using electrochemical impedance spectroscopy (EIS), scanning electron microscopy (SEM) as well as transmission electron microscopy (TEM). EIS measurements using symmetrical cells showed that the polarization

resistance decreased from 3.1 $\Omega.cm^2$ to 0.5 $\Omega.cm^2$ when LDC was co-impregnated with LST, characterized in humidified H_2 (3% H_2O) at 900 °C. In addition, the microstructure of the cell was modified when LDC was impregnated prior to L4ST into the porous YSZ. TEM and SEM results showed that the L4ST particles were finely distributed into the anode structure in the presence of LDC when compared to the L4ST alone.

The rate of electrochemical oxidation of H_2 and CH_4 feeds over $L_{0.4}Sr_{0.6}TiO_{3\pm\delta}$ and $La_{0.4}Ce_{0.6}O_{1.8}$-$La_{0.4}Sr_{0.6}TiO_{3\pm\delta}$ impregnated solid oxide fuel cell anodes increased significantly when H_2S (0.5%) was present. There was recovery of the fuel cell under galvanostatic conditions at 40 $mA.cm^{-2}$ and 800 °C in both H_2S (0.5%)-H_2 and H_2S (0.5%)-CH_4 after switching to H_2 as fuel. Mass spectrometry analysis revealed the effect of H_2S (0.5%) on the enhancement of CH_4 electrochemical oxidation.

Acknowledgement

I would like to give my sincere gratitude to my supervisor, Dr. Jing-Li Luo, whose knowledge, guidance, support and help from the beginning to the end, enabled me to understand the subject. With her great discipline, effort, encouragement and great advice, she truly inspired me to finish this dissertation.

A special thanks to my committee members for the time, effort and help you have taken to this dissertation.

I am heartily grateful to thank Dr. Alan Sanger, for his invaluable time, efforts and knowledge he has given me throughout my research and education. Thank you Alan, what you did was precious to me.

I also wish to thank my previous supervisors, Dr. Mohammad Ghorbani from Sharif University of Technology and Dr. Mohammad Hossein Paydar from Shiraz University, who helped and encouraged me to pursue my education.

I am indebted to my many colleagues and friends at University of Alberta for providing fun environment I which to learn and grow. I am especially thankful to my best friends Adrien Vincent, Ali Torabi and Guihua Zhou, Yashar Behnamian my best friends and colleagues for their knowledge, support, help and encouragement throughout my stay at the University of Alberta.

I am grateful to my group members past and present, Juri, Cheng, Vitaly, Nemanja, XianZhu, Xiaoxiong, Ning, Jianhui, Alfonso, Qing Xun, for your suggestions, supports and help. Without you this would not have been possible.

Last, and most importantly, I wish to thank my family for their unconditional help, support, encouragement and love, they have given me through my life.

Milad Roushanafshar

April 2012-04-01

Contents

List of Tables

List of Figures

List of Abbreviations

AFC	**Alkaline fuel cell**
ASR	**Area specific resistance**
DF	**Dark field**
DMFC	**Direct methanol fuel cell**
EIS	**Electrochemical impedance spectroscopy**
EMF	**Electromotive force**
FE-SEM	**Field emission scanning electron microscopy**
GC	**Gas chromatographic**
GDC	**Gadolinium doped ceria**
GDP	**Gross domestic product**
LDC	**Lanthanum doped ceria**
LSCF	**Lanthanum strontium chromium ferrite**
LSCM	**Lanthanum strontium chromium manganese**
LST	**Lanthanum doped strontium titanate**
MCFC	**molten carbonate fuel cell**
MEAs	**Membrane electrode assemblies**

MIECs	**Mixed ionic electronic conductors**
MS	**Mass spectrometric**
OCV	**Open circuit voltage**
PEMFC	**Polymer electrolyte membrane fuel cell**
PAFC	**Phosphoric acid fuel cell**
PD	**Potentiodynamic**
PDF	**Powder diffraction file number**
PS	**Potentiostatic**
PVB	**Poly(vinyl butyral-co-vinyl alcohol-co-vinyl acetate)**
SAD	**Selected area diffraction**
SCD	**Sulfur chemiluminescence detector**
SDC	**Samarium doped ceria**
SEM	**scanning electron microscopy**
SOFCs	**Solid oxide fuel cells**
SSZ	**Scandia stabilized Zirconia**
TEC	**Thermal expansion coefficient**
TEM	**Transmission electron microscopy**

TPBs	**Triple phase boundaries**
TPO	**temperature program oxidation**
XRD	**X-ray diffraction**
YST	**Yttria doped strontium titanate**
YSZ	**Yttrium stabilized Zirconia**

Chapter 1

Introduction

1.1 Motivation

Population growth, on-going industrialization process, industrial production relocation into Asian countries, the expansion of transportation infrastructure and the rise in standard of living are all drivers for this energy demand reported by the World Energy Council. Therefore, providing secure energy for economic development with the huge investment of 1.4% of global gross domestic product (GDP) per year by 2030 along with protecting the environment and promoting social equity and universal access to energy are all long term challenges ahead of energy problems. As a result, expanding the energy resources is necessary to meet these requirements. Renewable energy development is one of the solutions fulfilling energy demand and environmental issues [1–3]. Biomass, hydropower, geothermal, solar, wind and marine energies are all viable types of renewable energies which can also expand the availability of the global energy sources. However the promotion of clean energies is necessary, fossil fuels in any forms still meet 80% of the world energy demand. Consequently, design and development of more efficient energy technologies are needed; fuel cells, in any form especially solid oxide fuel cells (SOFCs), are potential candidates to meet these requirements.

1.2 Fuel Cells

A fuel cell is like a nonstop factory which is able to churn out product as long as provided by fuel unlike consumable batteries which should be replaced. In comparison to heat engines which convert chemical energy to electricity by running mechanical devices, fuel cells produce electricity directly from chemical reactions between reactants and make the harnessing of electrons possible by separating reactants from each other. Consequently, the efficiency increases by employing fuel cells and even can be increased further by joining it to other types of systems like heat engines or solar cells. Fuel cells have some advantages over combustion engines and batteries such as higher efficiency, cleanness, pollution free, silence, long-lasting system and higher capacity. However, they also have some disadvantages such as lower power density, fuel availability and storage as well as lower durability and cost which are challenging problems prior to extending the applications of these devices. Hydrogen is the best fuel for a fuel cell application but has a low volumetric capacity, is not easily available and storage is a problem; consequently, finding alternative fuels with higher volumetric capacity like gasoline, methanol, ethanol, methane, is a good way to solve some of these problems. However, using these kinds of fuels is not simple and is a minefield issue in fuel cell technology development [4].

Among different kinds of fuel cells, the solid oxide fuel cell has this ability to use a wide range of fuels based on its high temperature operating conditions but it still needs more development in terms of anode material selection in order to increase the activity and stability of

the cell towards different fuel components like hydrocarbons and corrosive impurities such as hydrogen sulfide.

1.3 History

The first fuel cell invented by Grove (1839) which was called gaseous voltaic battery in 1842 consisted of two platinum electrodes submerged in sulphuric acid and were covered by tubes while one tube contained oxygen and the other one stored hydrogen. At this condition, when the tubes were lowered, the galvanometer deflected because of electron flow in the external circuit. Afterwards, different gases, electrodes and electrolytes were used to figure out their effects on the cell current. Consequently, various types of fuel cells with different electrolytes, electrodes and fuels have been used and they can be categorized into six specific groups mainly based on electrolyte type and operating temperature: solid oxide fuel cell (SOFC, 1937), molten carbonate fuel cell (MCFC, 1946), alkaline fuel cell (AFC, 1946), polymer electrolyte membrane fuel cell (PEMFC, 1960), direct methanol fuel cell (DMFC, 1960s), and phosphoric acid fuel cell (PAFC, 1975) [5].

SOFC was invented in 1937 by Baur and Preis who used different compounds based on a zirconia tube as the electrolyte which was filled by carbon or iron as anode and covered by magnetite Fe_3O_4 as cathode while they were fed by hydrogen or carbon monoxide and oxygen, respectively. They obtained better results for yttrium stabilized zirconia (YSZ) compound which was invented by Nernst in 1890 who found that YSZ shows electrical conductivity at temperatures between 600 °C to 1000 °C and its electrical conductivity increases with

temperature contrary to metals behavior. However he could not explain this controversial behavior at that time; he reported that YSZ is an ionic conductive material based on oxygen vacancy mobility so that its ionic conductivity increases by temperature. Afterwards, Weissbart and Ruka (1962) used 85% ZrO_2 and 15% CaO as the electrolyte and Pt as anode and cathode while were fed by methane or hydrogen and oxygen, respectively. In fact, it was the first time that solid oxide fuel cell was used for hydrocarbon oxidation; however, its performance was not poor [6].

1.4 Electrochemistry, thermodynamics and kinetics

SOFC is basically a high temperature fuel cell which operates at temperature between 600 °C to 1000°C and offers the advantage of using a wide range of fuels with higher efficiency in comparison to other fuel cell types. The basic reactions occur in SOFC are reduction of O_2 molecules to O^{-2} ions at the cathode site and their oxidation reactions with hydrogen or carbon monoxide molecules at the anode site.

So the following reaction occurs at the cathode:

$$O_2 + 4e^- \leftrightarrow 2O^{2-} \quad (1.1)$$

If other kinds of fuels like H_2, CO, CH_4 or etc. are fed to the anode, the overall reaction changes:

$$H_2 + O_2 \leftrightarrow H_2O \quad (1.2)$$

$$CO + O_2 \leftrightarrow CO_2 \tag{1.3}$$

$$\left(CH_4 \xrightarrow{\text{yields}} CO + H_2\right) + O_2 \leftrightarrow CO_2 + H_2O \tag{1.4}$$

The electromotive force (EMF) or open circuit voltage (OCV) of SOFC is measured by the Nernst equation, which for equation (1.4) is given by:

$$E = E^0 + \frac{RT}{4F} \ln\left(\frac{a_{O_2}.a_{H_2}.a_{CO}}{a_{CO_2}.a_{H_2O}}\right) \tag{1.5}$$

where R is standard gas constant, T operating temperature, F Faraday constant and E_0 standard equilibrium cell potential which is given by:

$$E^0 = -\frac{\Delta G^0}{4F} \tag{1.6}$$

where ΔG^0 is standard Gibbs free energy of the cell reaction.

Although OCV represents ability of cell for converting chemical energy into electrical energy, the actual potential of the cell is lower than OCV of the cell because of polarization of the cell which restricts reaction rate and cell efficiency also. The actual potential of an SOFC is given by:

$$E_{actual} = E_{eq} - \eta_{ohmic} - \eta_{act(a)} - \eta_{act(c)} - \eta_{con} \tag{1.7}$$

where E_{actual} is the measured potential, E_{eq} the Nernst equilibrium potential, and η_{ohmic} η_{act}, η_{act}, and η_{conc} are ohmic polarization, anodic and cathodic and concentration polarizations of the cell,

respectively. The ohmic loss is based on total resistivity of the cell and represented by Ohm's law:

$$\eta_{ohmic} = iR_{ohmic} = i(R_{ionic} + R_{elec}) \tag{1.8}$$

where η_{ohmic} is the ohmic polarization of the cell, i the current, R_{ohmic} the total ohmic resistance of the cell, R_{ionic} and R_{elec} are the ionic and electronic resistances of the cell, respectively. Activation polarization is controlled by barrier energy for reaction at the electrode-electrolyte interfaces of either anode or cathode sites and controls the charge transfer process. In fact, activation polarization is represented as voltage loss to overcome barrier energy for electron transfer process and depends on exchange current density and charge transfer coefficient of the electrode-electrolyte-fuel system. The relationship between the current density –and activation polarization of an electrode is given by the Butler-Volmer equation:

$$i = i_0 \left(e^{\frac{\alpha n F \eta}{RT}} - e^{-\frac{(1-\alpha) n F \eta}{RT}} \right) \tag{1.9}$$

where, i_0 is the exchange current density of the electrode reaction, α is charge transfer coefficient, n number of electrons taking part in the electrochemical reaction and η is the overpotential of the reaction. Butler-Volmer equation is mainly applied for a reaction occuring at a metal surface which is in contact with a solution. In this case, a sharp potential variation occurs within a double layer with 1-2 nm thickness; this high potential gradient changes the energy barrier for the electrochemical reaction [7]. In contrast, a double layer does not exist for solid oxide electrodes with the potential gradient length in the range of 1 μm over the electrode-

electrolyte interface [6]. As a result, field gradients in solid oxide electrodes are small implying that this is not enough to change the barrier heights for most reactions [8]. In addition, the linearity of the I-V curves in solid oxide fuel cells implies that the potential independently varies with current, which changes Equation 1. 7 into:

$$E_{actual} = E_{eq} - i\left(R_{ohmic} + R_{act(a)} + R_{act(c)}\right) - \eta_{con} \tag{1.10}$$

Finally, concentration polarization restricts cell performance because of reactant depletion at the interface between catalyst and electrolyte which is mostly controlled by diffusion process of reactants from bulk to the vicinity of catalyst surface. The concentration polarization leads to the limiting current density where their concentrations theoretically dwindle to zero. Concentration polarization takes into account Nernstian and reaction losses based on reactant depletion and product concentration increase in comparison to their bulk concentration. Therefore, combination of these two losses lead to concentration loss and is represented by the equation:

$$\eta_{conc} = \left(\frac{RT}{nF}\right)\left(1 + \frac{1}{\alpha}\right)\ln\left(\frac{i_L}{i_L - i}\right) \tag{1.11}$$

where i_L is the limiting current density.

1.5 SOFC components

1.5.1 Basic requirements

SOFCs stacking consists of gas tight ionic conductor electrolyte, porous anode and cathode electrodes on each side of the electrolyte and interconnects which should be compatible with other parts and be stable at operating conditions. Therefore, the preliminary requirements for SOFC components are [6,9,10]:

1- Chemical stability at operating conditions; reducing atmosphere $pO_2 \sim 10^{-19}$ atm at anode side, $pO_2 \sim 1$ atm at cathode side while electrolyte and interconnect should be stable in both reducing and oxidizing conditions.
2- Phase and structural stability.
3- Chemical and mechanical compatibility between different components.
4- Reasonable mechanical properties like toughness and resistant towards cracking and thermal shock.
5- Competitive fabrication process and materials cost.

Several books and papers have been devoted to different SOFC's issues, especially materials selection. Brief discussion about different SOFC components is given in this section.

1.5.2 Electrolyte

In the SOFC systems, the electrolyte is an crucial part conducting oxygen ions at high temperature because of diffusion nature of process which needs activation energy to promote

vacancy positions inside the structure [9,11]. Therefore, ionic conductivity of electrolyte depends on available sites for oxygen diffusion and doping is a way to increase vacancy positions in order to enhance oxygen conduction of electrolyte:

$$\sigma = en\mu \tag{1. 12}$$

where e is the charge of a mobile ion, μ the mobility of oxygen vacancy, and n the number of mobile oxygen ion vacancies. At first glance, ionic conductivity increases by increasing vacancies; however, most importantly mobility of free vacancies affects conductivity which can be correlated to activation energy for conduction by equation:

$$\sigma = \frac{A}{T}[V_{\ddot{O}}](1 - [V_{\ddot{O}}]) \exp\left(-\frac{E}{RT}\right) \tag{1. 13}$$

where, E the activation energy for conduction, and A preexponential factor and depends on the concentration of vacancies. Therefore, ionic conductivity of a material depends on dopant concentration and its ionic radius[9].

Solid state electrolyte for SOFC application should provide preliminary requirements such as; high ionic conduction and trivial electronic conductivity, stability over broad range of temperature and oxygen partial pressure, chemical and mechanical compatibility with other components, and reasonable mechanical properties as well which can be found in a narrow range of materials including: $LaGaO_3$ perovskite structures, $Bi_4V_2O_{11}$ and $La_2Mo_2O_9$ derivatives, pyrochlore structures such as $(Gd,Ca)_2Ti_2O_{7-\delta}$, and apatite structure derived from $Ln_{10-x}Si_6O_{26\pm\delta}$

where Ln is a rare earth cation, in addition to conventional solid electrolytes such as ZrO_2 and CeO_2 fluorite structures which have been used for several decades [12]. $LaGaO_3$ structure offers higher ionic conductivity when doped with strontium, magnesium and cobalt; however, volatility of gallium oxide, its instability in reducing conditions, reactivity with anode materials especially perovskite structures, and high cost of gallium put a question mark over its application as electrolyte. Doped ceria is another candidate material for electrolyte application which offers high ionic conductivity in comparison to YSZ [13]. Gadolinium doped ceria (GDC) and samarium doped ceria (SDC) provide higher conductivity among different doping elements. Doped ceria electrolytes are generally considered as low temperature electrolytes for IT-SOFC applications mostly because of their reducibility in reducing atmosphere which increases n-type electronic conductivity and causes short circuiting [14]. In addition, thermal expansion of this structure because of reduction of Ce^{+4} to Ce^{+3} causes mechanical failure which limits the operating temperature of doped ceria electrolyte. Stabilized Zirconia is still widely used as the electrolyte for wide range of operating temperature because of its chemical stability, negligible electronic conductivity compared to other types of electrolytes, mechanical stability and competitive cost as well [15]. Scandium and yttrium are two common dopants that have been employed for the stabilizing cubic tetragonal structure of zirconia which increases its electrical conductivity as well [11].

1.5.3 Cathode

The basic requirements of cathode for solid oxide fuel cell applications are high electronic and ionic conductivities at operating temperature, high catalytic activity towards oxygen reduction reaction (Equation 1.1), adequate porosity for diffusion of oxygen to the cathode-electrolyte interface, compatibility with other components, and low cost [16]. Pt was the first acceptable cathode which was employed; however, it is not cost effective and it is important to use replacement in order to commercialized SOFC systems. Lanthanum manganite perovskite structure provides most of the requirements as cathode at high operating temperature (800 °C to 1000 °C) although it is reactive with YSZ at high temperature forming $La_2Zr_2O_7$. Doping small amount of strontium on A site significantly increases the stability of the structure. Doping strontium oxide in $La_{1-x}Sr_xMnO_{3\pm\delta}$ ($x<0.5$) enhances the electronic conductivity of the structure by oxidizing manganese ion through Equation 1.14, rather than producing oxygen vacancies [17]:

$$Mn_{Mn}^{x} + SrO \xleftrightarrow{LaMnO_3} Sr'_{La} + Mn_{Mn}^{\cdot} + O_{O}^{x} \qquad (1.14)$$

Using mixed ionic-electronic cathodes (MIECs) conductor oxides is another approach for improving the activity of the cathode structure, e.g., $La_{0.8}Sr_{0.2}Co_{1-y}Fe_yO_{3-\delta}$. Cobalt based cathode materials including $La_{1-x}Sr_xCoO_3$ display higher ionic and electronic conductivities among other cathode materials; however, their relatively high thermal expansion coefficients (TEC) limits

their application on different conventional electrolytes [16,18]. Substitution of Sr on La sites produces electron holes into the structure which is compensated by forming $Co_{Co}^{\cdot}$ and oxygen vacancies. Then, the overall electroneutrality is driven by [19]:

$$\mathrm{Sr_{Sr}^{x} + Co_{Co}^{\cdot} + 2V_{\ddot{O}} = Sr_{La}^{\prime} + Co_{Co}^{x}} \tag{1.15}$$

$$\mathrm{2Co_{Co}^{\cdot} + O_{O}^{x} \rightarrow 2Co_{Co}^{x} + V_{\ddot{O}} + \frac{1}{2}O_2(g)} \tag{1.16}$$

$LaFeO_3$ based cathode material is another promising candidate with higher stability and TEC compatibility when compared to cobaltite structures. The same electron hole formation occurs by substituting Sr for La, with charge neutrality maintained by forming Fe^{4+} or oxygen vacancies. At high temperature, the structure loses oxygen to form oxygen vacancies resulting in a decrease of hole concentrations [20]:

$$\mathrm{2Fe_{Fe}^{\cdot} + O_{O}^{x} \rightarrow \frac{1}{2}O_2 + 2Fe_{Fe}^{x} + V_{\ddot{O}}} \tag{1.17}$$

A combination of $LaFeO_3$ and $LaCoO_3$ with the overall composition of $La_{1-x}Sr_xFe_{1-x}Co_xO_{3\pm\delta}$ (LSCF) is another active anode material which is more stable than $LaCoO_3$ and more active than $LaFeO_3$, which can replace the LSM conventional cathode [21]. In addition, it shows high chemical compatibility with cerium oxide based electrolytes that can be used as a protective layer against reaction of LSCF with YSZ [16].

1.5.4 Anode

Electrochemical oxidation of fuel components occurs on the anode material, where the received oxygen ions from the electrolyte react with fuel and produce electrons transferred to the external circuit. Fuel variety is one of the main advantageous of using SOFCs, owing to oxygen conducting electrolyte and high operating temperature. Achieving this objective needs correct selection of anode material to enable fuel oxidation at operating temperature with the lowest polarization resistance in order to obtain high fuel conversion efficiency and power density. The prominent requirements of anode materials are:

- High electronic and ionic conductivity.
- Chemical and mechanical compatibility with electrolyte and interconnects.
- Electrocatalytic activity of anode to fuel components.
- Resistivity to degradation by carbon cracking and poisoning effect of H_2S in hydrocarbon fuels and syngas as well.
- Enough porosity for fuel flow to enhance the access of fuel to reaction sites.
- Low cost

Ni-YSZ cermet is a conventional anode which has been used mainly as anode in solid oxide fuel cells working with humidified hydrogen as fuel [22]. Adsorption, dissociation and oxidation of hydrogen readily occur on the surface of Ni. Employing this material in SOFC fuelled with hydrocarbons or syngas is definitely challenging based on carbon deposition which can block and decrease the activity of catalyst [23,24] in addition to sulfur poisoning [25,26]. Particle

coarsening, extreme volume expansion during oxidation-reduction process are other problematic issues of using a Ni-YSZ cermet [6]. Consequently, development of advanced anode materials which can effectively resist carbon deposition, show sulfur resistivity and display a comparable activity to fuel components is necessary.

Basically, two approaches have been employed for solving the problem of Ni-YSZ cermets, firstly using another kind of cermet such as Ni-GDC [27], Cu-YSZ and Cu-GDC [28] which improved some problems compared to the common Ni-YSZ cermet. Replacement of Ni with Cu significantly improved the carbon deposition problem. In contrast to Ni, Cu does not catalyze the cracking of hydrocarbons preventing formation of carbon fibers and improve the stability of the anode material when SOFCs are fed by hydrocarbons [29,30]. In addition, the presence of cerium oxide based materials enhances the carbon deposition stability of the electrode [31]. Secondly, development of single phase MIEC compounds with higher resistance towards carbon deposition and sulfur poisoning is another effective way for Ni-YSZ replacement. As a result, different ceramic materials with various structures such as fluorite [32–35], perovskite [36,37], pyrochlore [38], tungsten bronze [39,40], rutile [41], etc have been developed for this application.

Materials with different perovskite structures formed a wide range of anodes which have been extensively studied in different feeds. Diversity of this structure in which both A and B sites can be occupied with different elements implies the variations of different properties

including: electronic and ionic conductivities, catalytic activity and compatibility with electrolytes.

1.5.5 Perovskite structure

Perfect perovskite structure with the stoichiometry of ABO_3 is cubic structure in which A-site elements occupy 8 corners while are surrounded by 12 oxygen atoms and B-site element is located inside the octahedral structure formed by oxygen atoms. Generally, perovskite structures are assumed as ionic oxides where electrostatic forces dominate the structure and cations donate electrons to oxygen, but covalent bonds significantly control structure bonding and play an important role in material properties mainly electrical properties. Presence of electrostatic potential between ions changes their states, most significantly the state of B-O bonds which causes splitting of valence orbitals into different levels of energy where the fivefold degenerate d state is split into two groups, 3 t_{2g} and 2 e_g. On the other hand, oxygen 2p states are split into doubly degenerate $p_{\perp}$ state and non-degenerate $p_{\parallel}$ state with orientations perpendicular and parallel to the B-O axis, respectively. From ionic point of view, energy level difference between t_{2g} and $p_{\perp}$ energy gap affects electronic conductivity of the structure. In addition to this point of view, covalent mixing is another approach for interpretation of this structure in which overlap of d and p orbitals leads to formation of sigma (σ) and pi (π) hybrids which increases the covalent bonding. As a result, 23 states are produced which are divided into three anti-bonding, bonding states and non-bonding states with sigma and pi configurations. The energy difference between three equivalent π^0-type non-bonding bands and three equivalent π^*-type conduction

(anti-bonding) bands is fundamentally considered as the band gap, E_g where covalent mixing decreases with increasing band gap. Consequently, doping of A and B-sites effectively changes the bonding structure and band gap which probably influences properties of the structure [42].

Lanthanum chromites ($LaCrO_3$) based materials are p-type semiconductors which has been extensively considered mainly as a current collector and also as anode material [43]. Doping of different elements on La sites and Cr sites dramatically changes the properties of these materials. In contrast to Ni/YSZ anode, chromite based materials display low catalytic activity for H_2 oxidation which can be enhanced by doping certain elements on the A and B sites. Irvine and Tao [36] showed that $La_{0.75}Sr_{0.25}Cr_{0.5}Mn_{0.5}O_3$ can be a good replacement for state of the art Ni-YSZ anode with comparable electro-catalytic activity in wet hydrogen and only a small trace of carbon after 7 h at 900°C; however, 50% loss was observed during operation and shows low electronic conductivity in reducing atmosphere and low tolerance in the presence of 10% H_2S [44]. However, this material showed high activity and low carbon deposition when methane fed the cell [45], and that improved at the presence of GDC [46]. $Sr_2MgMoO_{6-\delta}$ with double perovskite structure is another promising candidate for methane oxidation although Pt was employed as a current collector which can catalyze methane oxidation. Moreover, a power density drop of only 4.8% was observed in H_2/H_2S (50ppm) after 200 h [37].

Strontium titanate based perovskite materials are another widespread anode with n-type conductivity behavior which has been studied mainly because of their high electronic

conductivities in reducing conditions. However, their catalytic activities are poor for H_2 oxidation, but offering high stability for carbon deposition and sulfur containing feeds.

1.5.6 Strontium titanate

Strontium titanate perovskite structure is an insulator material with a filled valence band and empty conduction band and band gap of 3.25 eV, but reduced $SrTiO_3$ is n-type semiconductor in low partial pressure of oxygen because of electron production in terms of reduction of Ti^{+4} to Ti^{+3} in reducing atmospheres.

Charge carriers equation for undoped strontium titanate can be expressed:

$$2\mathrm{Ti}_{\mathrm{Ti}}^{\mathrm{X}} + \mathrm{O}_{\mathrm{O}}^{\mathrm{X}} \overset{\mathrm{K}_1}{\Leftrightarrow} 2Ti'_{Ti} + \mathrm{V}_{\ddot{\mathrm{O}}} + {}^{1}/_{2}\ \mathrm{O}_2 \tag{1.18}$$

thus

$$\mathrm{n}^2 = [\mathrm{Ti}'_{\mathrm{Ti}}]^2 = \mathrm{K}_1 \frac{[\mathrm{Ti}_{\mathrm{Ti}}^{\mathrm{X}}]^2[\mathrm{O}_{\mathrm{O}}^{\mathrm{X}}]}{[\mathrm{V}_{\ddot{\mathrm{O}}}][\mathrm{P}_{\mathrm{O}_2}]^{1/2}} \tag{1.19}$$

Based on the charge electroneutrality, two Ti3+ ions formed for every oxygen vacancy. As a result, $V_{\ddot{O}}$ can be replaced by $[Ti'_{Ti}]$ in equation 1.19 resulting:

$$\sigma = \mathrm{e}[\mathrm{Ti}_{\acute{\mathrm{T}}\mathrm{i}}]\mu \approx [\mathrm{P}_{\mathrm{O}_2}]^{-1/6} \tag{1.20}$$

Donor doping of Sr sites is an effective way for enhancing electronic conductivity of $SrTiO_3$ in reducing atmosphere. In fact, the physical chemistry of A-site atom affects the

properties of perovskite structure by influencing the Ti-O bond. The Ti-O bond can be weakened either with increasing electronegativity of the A-site ion which makes the A-O bond more covalent or due to distortion of the perovskite structure as well [47].

Marina [48] showed that lanthanum doped strontium titanate (LST) would be a promising anode for solid oxide fuel cell application with acceptable electronic conductivity in reducing atmosphere, stability in highly reducing condition ($pO_2 \sim 10^{-19}$ atm) with better thermal expansion match to YSZ in comparison to Ni-YSZ anode and redox stability in both oxidizing and reducing atmospheres. Mukundan et al. [49] showed that LST can tolerate up to 1% H_2S for 8 h without any performance loss by changing the gas to hydrogen. Moreover, the cell performance increases by 20 percent at the presence of 5000 ppm H_2S which was stable for 24 hours.

Doping of strontium titanate by La donor dopant creates an impurity band resulting in a lower band gap (<2.9 eV) in comparison to pure $SrTiO_3$ and higher conductivity in reducing atmosphere as well [50,51]. In spite of undoped strontium titanate in which electrical conductivity is proportional to $pO_2^{-1/6}$ and varies with oxygen concentration [52], two different behaviors were observed for lanthanum doped strontium at different partial pressures of oxygen which is attributed to fundamentally different defect chemistry in doped and undoped $SrTiO_3$ structures. In fact, when strontium titanate is doped with La^{+3} ions, excess charge is compensated by either atomic imperfections or electronic imperfections at different partial pressure of oxygen. Donor dopant might be compensated by atomic imperfection or self compensation method by

formation of cation vacancy by absorbing excess oxygen which is accommodated into highly disordered structure probably by formation of SrO layer and Sr vacancy as well [53–55]:

$$La_2O_3 \xrightarrow{SrTiO_3} 2La_{Sr}^{\cdot} + 3SrO + Ti_{Ti} + V_{Sr}'' \quad (1.21)$$

Despite this, electronic compensation mechanisms presumably happens during moderate and highly reducing atmosphere based on valency change of Ti^{+4} to Ti^{+3} [50]:

$$La_x^{+3}Sr_{1-x}^{+2}Ti^{+4}O_{3+(\frac{x}{2})}^{-2} \xrightarrow[\text{reduction}]{\text{moderate}} La_x^{+3}Sr_{1-x}^{+2}Ti_{1-y}^{+4}Ti_y^{+3}O_{3+(\frac{x}{2})-(\frac{y}{2})}^{-2} \quad (1.22)$$

and

$$La_x^{+3}Sr_{1-x}^{+2}Ti^{+4}O_{3+(\frac{x}{2})}^{-2} \xrightarrow[\text{reduction}]{\text{strong}} La_x^{+3}Sr_{1-x}^{+2}Ti_{1-x}^{+4}Ti_x^{+3}O_3^{-2} \quad (1.23)$$

Therefore, electrical conductivity of $La_xSr_{1-x}TiO_3$ is mostly independent of oxygen partial pressure at low oxygen content specifically at high dopant concentration which is given by [56,57]:

$$\sigma = e[La_{Sr}^{\cdot}]\mu \quad (1.24)$$

In contrast to self compensation mechanism for donor doped $SrTiO_3$ which was mentioned, excess oxygen can be accommodated into structure by creation of $La_2Ti_2O_7$ planar structure. However, $La_xSr_{1-x}TiO_{3\pm\delta}$ system has been considered as cubic perovskite structure with general formula of ABO_3, it is composed of different perovskite slabs joined by octahedral

corners sharing along the [001] direction which belongs to members of the $La_4Sr_{n-4}Ti_nO_{3n+2}$ series. As a result, connectivity between octahedral corners is broken and highly distorted structure is formed by increase of excess oxygen beyond structure stoichiometry [58–61]. The presence of this layered structure was revealed by high resolution transmission electron microscopy (HRTEM) with corresponding electron diffraction pattern. For members with n>11, high oxygen content defects were randomly distributed in the structure which cannot be detected by XRD method; although, 40 at. % is usually considered as solubility limit for La in the $SrTiO_3$ structure [62,63].

Although donor doped $SrTiO_3$ structures with excess oxygen offer higher electronic conductivity [64,65], their electro-catalytic activities are not comparable to other effective anode materials like $La_{0.75}Sr_{0.25}Cr_{0.5}Mn_{0.5}O_3$ [36] which is mainly attributed to tendency of Ti to keep octahedral structure and lower oxygen conductivity [66]. Therefore, doping of Ti with acceptor dopant which can adopt lower coordination than octahedral may enhance oxygen-ion migration. Irvine et al. [67] showed that increase of Sc content decreases the overall oxygen content of LST structure; however, these phases still have oxygen overstoichiometry which was revealed by HRTEM. Furthermore, they observed n-type electrical conductivity which decreases by Sc addition due to lower tendency of Ti^{+4} ions reduction to Ti^{+3} ions and lower total amount of charge carrier electrons. Addition of Sc, Ga and Mn [68] significantly decreased the polarization resistance of the anode and electrochemical performance of $La_4Sr_8Ti_{11}Ga_{0.5}Mn_{0.5}O_{37.5}$ was

comparable with other efficient perovskite structure anodes even in the presence of methane as fuel at 950 °C [58].

Marina [69] analyzed the effect of several transition metals (Cr, Fe, Co, Ni, and Cu) and Ce on polarization resistances of doped strontium titanate anodes and found that cerium modified lanthanum strontium gives better electro-catalytic activity. Hue and Petric [70] showed that Co has lower detrimental effect on electrical conductivity of yttrium doped strontium titanate among other transition metals and enhances its catalytic activity which was attributed to mixed valence of cobalt and provides almost constant conductivity over wide range of oxygen partial pressure. He et al. [71] showed that yttrium oxide doped strontium titanate (YST) can be a good replacement for Ni when used as a composite with YSZ which can bring appropriate ionic conductivity. Addition of ceria to YST can be a good choice for anode in SOFC because of suitable electronic conductivity of YST in addition to high catalytic activity and ionic conductivity of ceria [72].

As mentioned, finding a single phase anode material which consists all of the requirements is a challenging issue for SOFC development. Improving one property sometimes leads to a drop in the other one. Consequently, we tried to use a composite structure in which each component plays a different role in order to improve the activity of the anode toward the oxidation of different fuels. LST was chosen mainly as the electronic conductor with high stability toward hydrogen sulphide poisoning and compatible thermal expansion with YSZ. In order to improve the ionic conductivity of the anode, YSZ and/or cerium based material were

added into the structure. Besides, the compatibility of the anode structure with YSZ electrolyte improves by adding YSZ. Addition of the cerium based catalysts may have dual advantage, first enhancing the ionic conductivity as they are more conductive when compare to YSZ, second improving the catalytic activity of the anode toward different fueling systems especially where the main concern is hydrocarbon oxidation.

1.6 Concept of triple phase boundary

Triple phase boundary (TPB) is reaction sites where a gas phase molecule, electrons, and oxygen ions must be available to electrochemical reactions occur. The concept of TPB is an important issue that needs to be addressed in order to improve the activity of the electrodes for either reducing or oxidation reaction. For pure electronic conductor electrodes, TPB is where the electrode and electrolyte interface each other [73]. Using a composite of electrolyte material and electrode can significantly extend the TPB along the electrode away from the electrolyte. In addition, application of MIEC materials enhances the TPB of the electrode resulting in high catalytic activity by providing more reaction sites for electrochemical reactions [74].

1.7 Hydrogen-fueled SOFCs

Hydrogen is a versatile fuel for SOFCs which is the main feed for different cells especially when Ni-YSZ is used as the anode material. Ni is a state of art catalyst for electrochemical oxidation of H_2. However it has different limitations including: redox instability

and particle coarsening which need to be addressed. High electronic conductivity of this anode material enables the fast collection of the electrons produced by electrochemical oxidation reactions. The reaction mechanism for electrochemical oxidation of H_2 on Ni-YSZ was shown by Wen et al. [75], constructed to find out the relationship between overpotential and surface reactions, with the assumption that the surface reaction is a controlling process and two other involved processes, surface diffusion and charge transfer, are not rate limiting. Therefore, the reaction phenomenon can be separated into different sub-reactions at equilibrium condition:

$$O_{(YSZ\ bulk)} + V_{ad} \leftrightarrow O_{ad}\ K_1 a_O \Theta_V = K_1' \Theta_O \tag{1.25}$$

$$H_{ad} + O_{ad} \leftrightarrow OH_{ad} + V_{ad}\ K_2 \Theta_H \Theta_O = K_2' \Theta_{OH} \Theta_V \tag{1.26}$$

$$H_{ad} + OH_{ad} \leftrightarrow H_2O_{ad} + V_{ad}\ K_3 \Theta_H \Theta_{OH} = K_3' \Theta_{H_2O} \Theta_V \tag{1.27}$$

$$H_2O_{ad} \leftrightarrow H_2O + V_{ad}\ K_4 \Theta_{H_2O} = K_4' P_{H_2O} \Theta_V \tag{1.28}$$

$$H_2 + 2V_{ad} \leftrightarrow 2H_{ad}\ K_5 P_{H_2} \Theta_V^2 = K_5' \Theta_{H_2}^2 \tag{1.29}$$

where k is the rate constant for each reaction, Θ is the coverage of each adsorbed species, and Θ_V is the coverage of vacancy. There is a relationship between the overpotential and activity of O on the anode (a_O^A) and on the reference electrode (a_O^R) with the assumption that these terms are proportional to the coverage of O on the anode and reference electrodes, respectively. With these assumptions, the overpotential can be derived as [76]:

$$\eta = \frac{RT}{2F}\ln\left(1 + \frac{i \times f \times K_a}{i \times S + 2F \times x_{H_2O} \times f}\right) \quad (1.30)$$

where f is the gas flow rate, K_a is determined by the equilibrium constant of equation 1.28 and rate constants of the backward equations 1.28 and 1.29, x_{H_2O} is the inlet mole fraction of water vapor, and S is the anode surface area. It was predicted that the materials with larger equilibrium O_{ad} coverage display lower overpotentials. This conclusion implies that larger equilibrium coverage will decrease the effect of current flow on induced coverage.

1.8 CO-fueled SOFCs

Carbon monoxide is a part of fuel either in syngas or in internal reforming of hydrocarbons. Therefore, its electrochemical oxidation mechanism is important in order to improve the catalytic activity of the anode materials. It has been found that the electrochemical activity of the CO is worse when compared to H_2 using different anode materials. It was suggested that the rate controlling reaction for CO oxidation on porous Pt/YSZ electrode is the chemical reaction involving adsorbed species on the surface [76]:

$$CO_{ad}(Pt) + O_{ad}(YSZ) \rightarrow CO_{2ad}(Pt) \quad (1.31)$$

$$2CO_{ad}(Pt) \rightarrow CO_{2ad}(Pt) + C_{ad}(YSZ) \quad (1.32)$$

with the rate equations:

$$i = K_1 p(CO)^{\frac{1}{2}}[a_O^*]^{1/2} - K_1' p(CO_2)^{1/2} \quad (1.33)$$

$$i = K_2 p(CO) - K_2' p(CO_2)^{1/2} [a_O^*]^{-1/2} \quad (1.34)$$

Fast sorption kinetics and direct oxidation of carbon monoxide was considered for the reactions along the electrolyte surface:

$$O^{2-} + CO \leftrightarrow CO_2 + 2e^- \quad (1.35)$$

In this case, the current density per TPB unit length can be expressed as [76]:

$$i = i_0 \left[\theta_e \exp\left(\frac{\alpha F \eta}{2RT}\right) - \exp\left(-\frac{(1+\beta)F\eta}{2RT}\right)\right] \quad (1.36)$$

where θ_e is the concentration of electronic charge carriers at the TPB.

1.9 CH_4-fueled SOFCs

Electrochemical oxidation rate of CH_4 is fairly low when compared to H_2 and CO on the anode catalyst. High molecular stability of the methane and catalyst deactivation by carbon formation are two challenging issues that need to be addressed. Carbon fouling can be highly prevented when the $p(H_2O)/p(CH_4)$ is higher than 2 causing internal reforming of CH_4 on the surface of the catalyst [30,31,77,78]:

$$CH_4 + H_2O = CO + 3H_2 \quad (1.37)$$

Followed by the direct electrochemical oxidation of produced H_2 and CO:

$$H_2 + O^{2-} = H_2O + 2e^- \quad (1.38)$$

$$CO + O^{2-} = CO_2 + 2e^{2-} \quad (1.39)$$

The oxidation of CO can also proceed by water gas shift reaction:

$$CO + H_2O = CO_2 + H_2 \quad (1.40)$$

followed by the reaction to oxidize H_2 (Equation 1.38).

The internal reforming of CH_4 is highly favorable on Ni/YSZ electrode; however, carbon formation limits the application of Ni for this reaction. In addition, the reaction is highly endothermic which increase the probability of cracking because of thermal shock. Direct electrochemical oxidation of CH_4 is another possible way for using this feed for SOFCs:

$$CH_4 + 4O^{2-} = CO_2 + 2H_2O + 8e^- \quad (1.41)$$

This reaction is unlikely to proceed in one step, possibly several reaction steps occur:

$$CH_4 + 3O^{2-} = CO + 2H_2O + 6e^- \quad (1.42)$$

followed by oxidation of CO often equation 1.39.

Another possibility is the thermal decomposition of CH_4:

$$CH_4 = C + 2H_2 \quad (1.43)$$

followed by electrochemical oxidation of H_2 toward equation 1.38 and electrochemical oxidation of C:

$$C + O^{2-} = CO + 2e^{-} \quad (1.44)$$

proceed to electrochemical oxidation of CO (equation 1. 39).

Mogensen et al. [79] investigated the CH_4 electrochemical oxidation and internal reforming when GDC was used as the anode material. It was mentioned that the presence of GDC alone is not enough for methane reforming at high temperature. Beside the electrocatalytic activity of GDC toward methane oxidation was fairly low when compared to Ni based catalyst. They suggested the addition of C-H bond breaking catalysts including: Ni, Ru and Pt along with GDC for enhancing the electrochemical activity of the anode. In contrast to active catalysts, no carbon formation was observed using GDC anode material neither under OCV condition nor when the cell was polarized. Reduced GDC may adsorb water under open circuit conditions; hence, that can directly react with carbon species cleaning the surface of the catalyst:

$$C + H_2O_{ad} = CO + H_2 \quad (1.45)$$

Possibly proceed toward reaction 1.4, and then CO_2 takes part into gasification of carbon:

$$C + CO_2 = 2CO \quad (1.46)$$

At high overpotentials (potential versus Pt/Air > 0V) evolution of oxygen occurs via fast discharge of oxygen ions to weakly bonded adsorbed oxygen on the surface of GDC which is ready to react with methane, similar to the reaction of methane with adsorbed oxygen on the surface of the catalyst from the gas phase:

1.10 H_2S-fueled SOFCs

Fuel flexibility is one of the major advantageous of SOFCs which makes their application economically viable. Direct utilization of fuel decreases the cost of fuel processing and purification. However direct utilization of different fuels including hydrocarbons for SOFCs are challenging regarding sulfur poisoning and carbon deposition. A very few ppm of H_2S can poison the conventional Ni/YSZ anode material depending on operating conditions including overpotential, temperature and concentration of H_2S [80,81]. Therefore, different approaches need to follow to mitigate the adverse effect of H_2S on the anode material and improve the stability of the SOFCs in H_2S containing feeds. Ni/YSZ has been extensively studied in different feeds containing different concentrations of H_2S. It was thermodynamically predicted that the sulfidation of Ni is not viable at high operating temperature when the concentration of H_2S is lower than 1000 ppm at 800 °C; however, Dong et al. [82] detected Ni_3S_2 by Raman spectroscopy on Ni/YSZ after 5 days exposure to 100 ppm H_2S. The difference in result could be related to the difference of bulk thermodynamics and surface thermodynamics of the catalyst. In fact, different surface related features including the microstructure, particle size and electric field during SOFC operation can affect this result. It was suggested that the main degradation mechanism for Ni/YSZ is the adsorbed sulfur species on the surface of the catalysts limiting the TPB by preventing access of fuel to the reaction sites:

$$H_2S(g) \leftrightarrow HS_{ad} + H_{ad} \leftrightarrow S_{ad} + H_{2(ad)} \tag{1.47}$$

For the SOFCs operating at very high concentration of H_2S (> 1000 ppm), the sulfidation of the Ni is the main reason for the cell degradation which causes the dilamination of the anode:

$$Ni + H_2S \leftrightarrow NiS + H_2 \quad (1.48)$$

$$3Ni + xH_2S \leftrightarrow Ni_3S_x + xH_2 \quad (1.49)$$

Different strategies have been tried for improving the stability of the anode towards sulfur poisoning including: electrochemical oxidation of sulfur species, improve the ionic conductivity of Ni based anode materials, replacing Ni with less reactive metals or alloys, using metal sulfide or thiospinels materials as anode, and using MIEC materials. Depending on the feed and concentration of H_2S, different strategies can be followed.

1.10.1 Electrochemical oxidation of H_2S

H_2S is a reactive gas which can be electrochemically oxidized in SOFCs over proper and stable catalysts. Pujare et al. [83] studied the possibility of direct oxidation for H_2S on thiospinel $CuFe_2S_4$ at 900 °C. Peterson et al. [84] also studied the electrochemical oxidation of H_2S for SOFCs using Pt/SDC anode catalyst. They suggested different reaction paths for the electrochemical oxidation of H_2S at high temperature.

H_2S can be directly oxidized with oxygen ions toward equations 1.50 and/or 1.51:

$$H_2S + O^{2-} \rightarrow H_2O + \frac{1}{2}S_2 + 2e^- \quad (1.50)$$

$$H_2S + 3O^{2-} \rightarrow H_2O + SO_2 + 6e^- \quad (1.51)$$

Produced sulfur in equation 1.50 can be oxidized to produce SO_2:

$$\frac{1}{2}S_2 + 2O^{2-} \rightarrow SO_2 + 4e^- \quad (1.52)$$

In addition, H_2S can be thermally decomposed to H_2 and S_2 at high temperature (~8.6% at 830 °C):

$$H_2S = H_2 + \frac{1}{2}S_2 \quad (1.53)$$

Both can be electrochemical oxidized to produce H_2O and SO_2, respectively.

SO_2 is less reactive when compared to H_2S resulting in a decrease in the poisoning effect of the feed. Therefore, controlling the potential of the cell with the right choice of material to direct the reactions toward production of SO_2 can be a possible way to mitigate the adverse effect of H_2S.

1.10.2 Improve the ionic conductivity

Enhancing the ionic conductivity of both anode material on and electrolyte can significantly improve the stability of the anode material via oxidizing the sulfur species into less reactive compounds including SO_2. Using scandia stabilized zirconia (SSZ) instead of YSZ as the electrolyte and part of the anode components remarkably improved the cell performance and sulfur tolerance of the anode [85]. One of the drawbacks of using SSZ is its high cost. Cerium oxide based catalysts are another material to improve the catalytic activity of the anode and improve its stability towards sulfur poisoning. Ni-GDC showed higher stability toward sulfur

poisoning when compared to Ni-YSZ at 9 ppm H_2S [80]. Cerium oxides are well known for H_2S adsorption resulting in cerium oxysulfide in reducing condition [86]:

$$CeO_{2-x}(s) + H_2S(g) + (1-2x)H_2(g) \leftrightarrow Ce_2O_2S(s) + 2(1-x)H_2O(g) \quad (1.54)$$

Consequently, one of the stability mechanisms for cerium oxide containing anode material could be higher adsorption ability of these materials which can prevent Ni deactivation. However, Ni-SDC was poisoned by 10 ppm H_2S under OCV condition [87]. Therefore, higher available oxygen on the surface of the catalyst could be the main reason for this stability mechanism. In addition, cerium oxide can catalyze hydrogen oxidation even when Ni was covered by sulfur species.

1.10.3 Metal sulfides and thiospinels

Exposure of H_2S to metals or alloys by controlling the gas atmosphere and temperature results in forming metal sulfides or thiospinel based materials which can be potential anode materials for high concentrations H_2S-containing feeds.

$$xM + yH_2S = M_xS_y + yH_2 \quad (1.55)$$

$$A_2BO_4 + 4H_2S = A_2BS_4 + 4H_2O \quad (1.56)$$

High electronic conductivity, catalytic activity for H_2S oxidation, along with high stability are all advantageous of using these types of materials. Among all different materials, MoS_2, WS_2, CoS_2, $CuCo_2S_4$, $NiFe_2S_4$ were identified as the most active catalysts for the anode

[83,84,88,89]. Low redox stability because of high volume difference between oxide and sulfide states, high vapor pressure of some sulfides, and high thermal expansion coefficient difference between sulfides and conventional electrolytes make the application of these types of materials limited. In addition, the interaction of these materials with other feeds is unknown in terms of activity and stability [90].

1.10.4 MIEC materials

Using ceramic based materials has different advantageous for being as the anode in SOFCs. One of the advantageous is increasing the stability of anode toward sulfur poisoning. Different structures, mainly perovskite structures, have been studied under different concentrations of H_2S which make the comparison difficult. Among all different materials with different structures, LST displayed the highest stability for sulfur poisoning, even after exposure to 10% H_2S [49]. It was previously mentioned that this material does not actively catalyze the electrochemical oxidation of fuel and needs to be used with other active materials or be doped with other oxides.

1.11 Scope of thesis

The main goal of this project is to develop and characterize an anode material for SOFCs using high concentration H_2S-containing feeds. Finding an anode material which can provide all the requirements including electronic and ionic conductivity, high catalytic affinity toward feed component, stability for carbon deposition, most importantly sulfur poisoning for our application, is highly needed. Moreover, finding possible mechanisms for the interaction of feed

components with the anode material is necessary for developing the material for this application. In fact, analyzing the materials to find out more information about their behavior can give us more insight in order to mitigate all the adverse effects on the stability and catalytic activity of the cell.

We develop an anode material based on a composite of LST and cerium oxides (YDC and LDC) to be tested in H_2S (0.5%)-containing feeds (syngas and methane). LST is an n-type material with high electronic conductivity in reducing atmosphere. However, its fairly low catalytic activity for fuel oxidation and low ionic conductivity for oxygen ions limit the application of this material as the anode. The promising advantage of this material is its high stability in high concentration H_2S-containing feeds which persuade us into characterizing this material in order to improve its catalytic activity for high concentration H_2S (0.5%)-containing feeds. On the other hand, cerium oxide based materials can provide high ionic conductivity and also improve the catalytic activity of the cell especially for oxidation of hydrocarbons. However, their chemical stability in the presence of high concentrations of H_2S is a challenging issue which should be addressed. There is no information in the literature for electrochemical stability of these composite materials for high concentration H_2S (0.5%)-containing feeds. Consequently, composite anode materials were synthesized and electrochemically analyzed using different electrochemical tests including potentiodynamic, potentiostatic, galvanostatic and electrochemical impedance spectroscopy (EIS). Scanning electron microscopy (SEM) and transmission electron microscopy (TEM) were employed to analysis the surface morphology

before and after fuel cell tests and microstructure. In addition, several gas analyses methods including gas chromatograph and mass spectroscopy were used to study the reaction of the feed with the anode material during fuel cell runs.

1.12 References

[1] N.L. Panwar, S.C. Kaushik, S. Kothari, Renewable and Sustainable Energy Reviews 15 (2011) 1513–1524.

[2] M.G. Salameh, Applied Energy 75 (2003) 33–42.

[3] W.T. Tsai, Y.H. Chou, Renewable and Sustainable Energy Reviews 9 (2005) 119–147.

[4] R. O'Hayre, Fuel Cell Fundamentals, 2nd edition, John Wiley & Sons, 2006.

[5] G. Hoogers, Fuel Cell Technology Handbook, Society of Automotive Engineers,U.S., 2002.

[6] S.C. Singhal, High-temperature Solid Oxide Fuel Cells: Fundamentals, Design and Applications, 1st ed., Elsevier Science, 2003.

[7] A.J. Bard, L.R. Faulkner, Electrochemical Methods: Fundamentals and Applications, 2nd ed., Wiley, 2000.

[8] R.J. Gorte, J.M. Vohs, Annu. Rev. Chem. Biomol. Eng. 2 (2011) 9–30.

[9] J. Fergus, R. Hui, X. Li, D.P. Wilkinson, J. Zhang, eds., Solid Oxide Fuel Cells: Materials Properties and Performance, CRC Press, 2008.

[10] H. Yokokawa, Annual Review of Materials Research 33 (2003) 581–610.

[11] J.B. Goodenough, Annual Review of Materials Research 33 (2003) 91–128.

[12] T.H. Etsell, S.N. Flengas, Chem. Rev. 70 (1970) 339–376.

[13] K. Eguchi, T. Setoguchi, T. Inoue, H. Arai, Solid State Ionics 52 (1992) 165–172.

[14] A. Tarancón, Energies 2 (2009) 1130–1150.

[15] S.P.S. Badwal, Solid State Ionics 52 (1992) 23–32.

[16] C. Sun, R. Hui, J. Roller, Journal of Solid State Electrochemistry 14 (2010) 1125–1144.

[17] J.M. Ralph, A.C. Schoeler, M. Krumpelt, Journal of Materials Science 36 (2001) 1161–1172.

[18] A. Weber, E. Ivers-Tiffée, Journal of Power Sources 127 (2004) 273–283.

[19] A.N. Petrov, O.F. Kononchuk, A.V. Andreev, V.A. Cherepanov, P. Kofstad, Solid State Ionics 80 (1995) 189–199.

[20] E.V. Bongio, H. Black, F.C. Raszewski, D. Edwards, C.J. McConville, V.R.W. Amarakoon, Journal of Electroceramics 14 (2005) 193–198.

[21] A. Esquirol, N.P. Brandon, J.A. Kilner, M. Mogensen, Journal of The Electrochemical Society 151 (2004) A1847–A1855.

[22] W.. Zhu, S.. Deevi, Materials Science and Engineering: A 362 (2003) 228–239.

[23] T. Kim, G. Liu, M. Boaro, S.-I. Lee, J.M. Vohs, R.J. Gorte, O.H. Al-Madhi, B.O. Dabbousi, Journal of Power Sources 155 (2006) 231–238.

[24] S. Park, J.M. Vohs, R.J. Gorte, Nature 404 (2000) 265–267.

[25] Y. Matsuzaki, I. Yasuda, Solid State Ionics 132 (2000) 261–269.

[26] F.P. Nagel, T.J. Schildhauer, J. Sfeir, A. Schuler, S.M.A. Biollaz, Journal of Power Sources 189 (2009) 1127–1131.

[27] Fifth European Solid Oxide Fuel Cell Forum, European Fuel Cell Forum, Oberrohfdorf, Switzerland 1 (2002) 523–530.

[28] S. McIntosh, J.M. Vohs, R.J. Gorte, Journal of The Electrochemical Society 150 (2003) A470–A476.

[29] H. Kim, C. Lu, W.L. Worrell, J.M. Vohs, R.J. Gorte, Journal of The Electrochemical Society 149 (2002) A247–A250.

[30] R.J. Gorte, S. Park, J.M. Vohs, C. Wang, Advanced Materials 12 (2000) 1465–1469.

[31] E.P. Murray, T. Tsai, S.A. Barnett, Nature 400 (1999) 649.

[32] A. Kelaidopoulou, A. Siddle, A.L. Dicks, A. Kaiser, J.T.. Irvine, Fuel Cells 1 (2001) 226–232.

[33] A. Kelaidopoulou, A. Siddle, A.L. Dicks, A. Kaiser, J.T.. Irvine, Fuel Cells 1 (2001) 219–225.

[34] A. Kaiser, A. Feighery, D. Fagg, J. Irvine, Ionics 4 (1998) 215–219.

[35] S. Tao, J.T.S. Irvine, Journal of Solid State Chemistry 165 (2002) 12–18.

[36] S. Tao, J.T.S. Irvine, Nat Mater 2 (2003) 320–323.

[37] Y.-H. Huang, R.I. Dass, Z.-L. Xing, J.B. Goodenough, Science 312 (2006) 254 –257.

[38] S. Kramer, M. Spears, H.L. Tuller, Solid State Ionics 72, Part 2 (1994) 59–66.

[39] P.. Slater, J.T.. Irvine, Solid State Ionics 120 (1999) 125–134.

[40] A. Kaiser, J.. Bradley, P.. Slater, J.T.. Irvine, Solid State Ionics 135 (2000) 519–524.

[41] C.M. Reich, A. Kaiser, J.T.. Irvine, Fuel Cells 1 (2001) 249–255.

[42] T. Wolfram, S. Ellialtioglu, Electronic and Optical Properties of d-Band Perovskites, Cambridge University Press, 2006.

[43] S.P. Jiang, S.H. Chan, Journal of Materials Science 39 (2004) 4405–4439.

[44] S. Zha, P. Tsang, Z. Cheng, M. Liu, Journal of Solid State Chemistry 178 (2005) 1844–1850.

[45] S.P. Jiang, X.J. Chen, S.H. Chan, J.T. Kwok, K.A. Khor, Solid State Ionics 177 (2006) 149–157.

[46] S.P. Jiang, X.J. Chen, S.H. Chan, J.T. Kwok, Journal of The Electrochemical Society 153 (2006) A850–A856.

[47] S. Hui, A. Petric, Journal of The Electrochemical Society 149 (2002) J1–J10.

[48] O.A. Marina, N.L. Canfield, J.W. Stevenson, Solid State Ionics 149 (2002) 21–28.

[49] R. Mukundan, E.L. Brosha, F.H. Garzon, Electrochem. Solid-State Lett. 7 (2004) A5–A7.

[50] B. Odekirk, U. Balachandran, N.G. Eror, J.S. Blakemore, Journal of the American Ceramic Society 66 (1983) C–22–C–23.

[51] B. Odekirk, J.S. Blakemore, Journal of The Electrochemical Society 130 (1983) 321–326.

[52] U. Balachandran, N.G. Eror, Journal of Solid State Chemistry 39 (1981) 351–359.

[53] N.G. Eror, U. Balachandran, Journal of Solid State Chemistry 40 (1981) 85–91.

[54] B.F. Flandermeyer, A.K. Agarwal, H.U. Anderson, M.M. Nasrallah, J Mater Sci 19 (1984) 2593–2598.

[55] R. Meyer, R. Waser, J. Helmbold, G. Borchardt, Journal of Electroceramics 9 (2002) 101–110.

[56] U. Balachandran, N.G. Eror, J. Electrochem. Soc. 129 (1982) 1021–1026.

[57] R. Moos, S. Schöllhammer, K.H. Härdtl, Applied Physics A: Materials Science & Processing 65 (1997) 291–294.

[58] J.C. Ruiz-Morales, J. Canales-Vázquez, C. Savaniu, D. Marrero-López, W. Zhou, J.T.S. Irvine, Nature 439 (2006) 568–571.

[59] M.E. Bowden, D.A. Jefferson, I.W.M. Brown, Journal of Solid State Chemistry 117 (1995) 88–96.

[60] J. Canales-Vázquez, M.J. Smith, J.T.S. Irvine, W. Zhou, Adv. Funct. Mater. 15 (2005) 1000–1008.

[61] P.D. Battle, J.E. Bennett, J. Sloan, R.J.D. Tilley, J.F. Vente, Journal of Solid State Chemistry 149 (2000) 360–369.

[62] U. Balachandran, N.G. Eror, J American Ceramic Society 64 (1981) c–75–c–76.

[63] R. MOOS, T. BISCHOFF, W. MENESKLOU, K. HARDTL, Journal of Materials Science 32 (1997) 4247–4252.

[64] T. Kolodiazhnyi, A. Petric, Journal of Electroceramics 15 (2005) 5–11.

[65] F.J. Lepe, J. Fernández-Urbán, L. Mestres, M.L. Martínez-Sarrión, Journal of Power Sources 151 (2005) 74–78.

[66] U. Kiessling, J. Claus, G. Borchardt, S. Weber, S. Scherrer, Journal of the American Ceramic Society 77 (1994) 2188–2190.

[67] J. Canales-Vazquez, J.C. Ruiz-Morales, J.T.S. Irvine, W. Zhou, Journal of The Electrochemical Society 152 (2005) A1458–A1465.

[68] Q.X. Fu, F. Tietz, D. Stover, J. Electrochem. Soc. 153 (2006) D74–D83.

[69] O.. Marina, L.. Pederson, In: J. Huijsmans, Editor, Fifth European Solid Oxide Fuel Cell Forum, European Fuel Cell Forum, Oberrohfdorf, Switzerland (2002) 481–489.

[70] S. Hui, A. Petric, Materials Research Bulletin 37 (2002) 1215–1231.

[71] H. He, Y. Huang, J.M. Vohs, R.J. Gorte, Solid State Ionics 175 (2004) 171–176.

[72] S. Koutcheiko, Y. Yoo, A. Petric, I. Davidson, Ceramics International 32 (2006) 67–72.

[73] C.W. Tanner, K.-Z. Fung, A.V. Virkar, Journal of The Electrochemical Society 144 (1997) 21–30.

[74] H. Ullmann, N. Trofimenko, F. Tietz, D. Stöver, A. Ahmad-Khanlou, Solid State Ionics 138 (2000) 79–90.

[75] C. Wen, R. Kato, H. Fukunaga, H. Ishitani, K. Yamada, Journal of The Electrochemical Society 147 (2000) 2076–2080.

[76] E. Tsipis, V. Kharton, Journal of Solid State Electrochemistry 12 (2008) 1039–1060.

[77] S. McIntosh, R.J. Gorte, ChemInform 35 (2004) no–no.

[78] S. Park, R. Craciun, J.M. Vohs, R.J. Gorte, Journal of The Electrochemical Society 146 (1999) 3603–3605.

[79] O.A. Marina, M. Mogensen, Applied Catalysis A: General 189 (1999) 117–126.

[80] L. Zhang, S.P. Jiang, H.Q. He, X. Chen, J. Ma, X.C. Song, International Journal of Hydrogen Energy 35 (2010) 12359–12368.

[81] Z. Cheng, J.-H. Wang, Y. Choi, L. Yang, M.C. Lin, M. Liu, Energy Environ. Sci. 4 (n.d.) 4380–4409.

[82] J. Dong, Z. Cheng, S. Zha, M. Liu, Journal of Power Sources 156 (2006) 461–465.

[83] N.U. Pujare, K.W. Semkow, A.F. Sommells, J. Electrochem. Soc. 134 (1987) 2639–2640.

[84] D.R. Peterson, J. Winnick, Journal of The Electrochemical Society 145 (1998) 1449–1454.

[85] K. Sasaki, K. Susuki, A. Iyoshi, M. Uchimura, N. Imamura, H. Kusaba, Y. Teraoka, H. Fuchino, K. Tsujimoto, Y. Uchida, N. Jingo, J. Electrochem. Soc. 153 (2006) A2023–A2029.

[86] H. Devianto, S.P. Yoon, S.W. Nam, J. Han, T.-H. Lim, Journal of Power Sources 159 (2006) 1147–1152.

[87] A. Tomita, K. Tsunekawa, T. Hibino, S. Teranishi, Y. Tachi, M. Sano, Solid State Ionics 177 (2006) 2951–2956.

[88] M. Liu, G. Wei, J. Luo, A.R. Sanger, K.T. Chuang, J. Electrochem. Soc. 150 (2003) A1025–A1029.

[89] K. Chuang, J. Luo, A. Sanger, Chemical Industry and Chemical Engineering Quarterly 14 (2008) 69–76.

[90] M. Gong, X. Liu, J. Trembly, C. Johnson, Journal of Power Sources 168 (2007) 289–298.

Chapter 2

Effect of hydrogen sulfide inclusion in syngas feed on the electrocatalytic activity of LST-YDC composite anodes for high temperature SOFC applications

2.1. Introduction

SOFCs have been developed as alternatives to conventional energy systems with the objectives of decreasing energy production costs, more efficient utilization of energy resources and minimization of environmental pollution. Through the selection of appropriate anode catalysts SOFCs are able to use a wide range of fuels with the best known conversion efficiency at high operating temperature, and produce less environmental pollution than generators such as conventional combustion systems. These specific advantages make SOFCs attractive options as systems for energy production [1,2].

Hydrogen (H_2) has been extensively used as the fuel for SOFCs, partly in order to have a clean energy production system. Ni-YSZ based catalysts have been found to be among the most active anode materials for electro-oxidation of H_2 when compared to alternative anode candidates including ceramic based materials. High electronic and catalytic activities [3], comparable TEC with YSZ [4], in addition to low cost, make this material a viable and

economical anode for SOFC applications. However, using Ni as a catalyst has some drawbacks including: short lifetime because of particle coarsening [5]; low redox stability [6]; and, above all, its instability when using hydrocarbons [7,8] and sulfur-containing fuels [9-11].

Replacing H_2 with other fuel types including syngas (H_2 + CO) and hydrocarbons would provide a major advance toward applications of SOFCs as economical and efficient candidates for future energy conversion systems. Thus, to enable this advance it is necessary to replace Ni with another material in order to widen options for SOFC feeds. As a result, a challenging but promising issue in SOFC development is replacing Ni-based anode catalysts with other types of materials with no or minimal loss of performance.

Many approaches have been investigated for increasing the stability and resistance of the anode when H_2S-containing hydrocarbons are used as anode feed. Among these, an attractive option uses anodes comprising strontium titanate ($SrTiO_3$) based materials with cubic perovskite structure. Appropriate electronic conductivity, TEC compatibility with yttria stabilized zirconia (YSZ, typically 8% Y_2O_3), stability toward redox reactions, and its high stability towards sulfidation when there is less than 10 wt% H_2S in the feed [12] make this material one of the most promising candidates for anode material when using sour fuels [13]. Unfortunately, the catalytic activity of this material is not as high as that of Ni and LSCM anode materials [14]. Nevertheless, $SrTiO_3$-based anode materials remain a potentially valuable and economically viable choice for use with high concentration H_2S-containing feeds as its stability toward H_2S could compensate for its lower catalytic activity. Marina et al. [15] tried to improve the catalytic

activity of a lanthanum-substituted $SrTiO_3$, $La_{0.4}Sr_{0.6}TiO_3$ (L4ST), by partly substituting the B-sites with Fe, Ni, Cu, Co and Ce in order to decrease the polarization resistance of the anode. Addition of cerium ions significantly decreased the impedance of the anode and enhanced the performance of the cell when humidified H_2 was used as the feed. They also suggested that Ce ions could partially replace Ti^{4+} ions; however, CeO_2 itself was detected as a secondary phase. They also examined the stability of this composite material in H_2 containing H_2S, and showed it was stable for over 100 h when 100 ppm H_2S was present in H_2 under humidified conditions. Partially replacing Ti^{4+} with Mn^{3+} and Ga^{3+} was shown to be another effective approach for improving electrochemical activity of LST anode materials [16,17]. However there are no data on the tolerance of these materials to sour feeds. YST-YSZ composite impregnated with CeO_2 and Ru was used as the anode material for H_2S-containing feed [18]. This anode also offered stability in low concentrations of H_2S. Cerium oxide based materials are effective catalysts for the water gas shift reaction [19,20] and oxidation and reforming of hydrocarbons [21,22]. Also, CeO_2 is an effective support for noble metal catalysts as it improves their stability [20].

It was found that the presence of H_2S increased the rate of conversion of methane as SOFC fuel using a composite L4ST and YSZ anode [23], an effect of participation by H_2S in the reaction mechanism without the H_2S itself being converted. However, it was not known whether this effect was peculiar specifically to the L4ST-YSZ anode and methane as fuel or whether similar effects would occur over other anode catalysts or when using other anode feeds. Herein we describe the effect of H_2S inclusion in the anode feed on the catalytic activity and the

chemical and electrochemical stability of composite L4ST and $Y_{0.2}Ce_{0.8}O_{2-\delta}$ (YDC) anodes in SOFC fueled with syngas comprising 40% H_2 and 60% CO.

2.2. Experimental section

LST and YDC both were synthesized using a citrate-nitrate gel combustion method [24]. Lanthanum(III) nitrate hexahydrate ($La(NO_3)_3.6H_2O$; Aldrich, 99.999%), strontium nitrate ($Sr(NO_3)_2$; Aldrich, puriss), yttrium(III) nitrate hexahydrate ($Y(NO_3)_3 .6H_2O$; Acros, 99.9%), cerium(III) nitrate hexahydrate ($Ce(NO_3)_3.6H_2O$; Aldrich, 99.99%), titanium(IV) propoxide ($Ti(OC_3H_7)_4$; TP; Aldrich, 98%), citric acid (CA; Acros, 99%) and triethanolamine (TEA; MP Biomedicals) were used as starting precursors.

For LST preparation, CA was initially added to stirred water preheated at 60 °C. After dissolving CA, $La(NO_3)_3.6H_2O$ and $Sr(NO_3)_2$ were added to prepare a homogenous solution. TP was stabilized in TEA at 60 °C for 1 h until its color changed to pale green. Then the citrate-nitrate solution was slowly added over 1 h into the latter solution while it was vigorously stirred at room temperature. The final molar ratio was 2:2:1 for CA: TEA: total metal ions.

YDC solution was prepared by adding stoichiometric amounts of $Y(NO_3)_3 .6H_2O$ and $Ce(NO_3)_3.6H_2O$ into the citrate solution with 2:1 molar ratio of CA: total metal ions and stirred continuously to form a homogeneous solution. The resulting gels were formed after continuously stirring solutions for 24 h at 80 °C. The LST and YDC gels were combusted at 550 °C and 350 °C respectively for 2 h to obtain crystalline powders. After combustion each of the LST and

YDC powders was ball milled for 2 h and calcined at 900 °C for 4 h to burn off carbon residues. To increase the crystallinity of LST it was calcined at 1300 °C for a further 4 h.

Membrane electrode assemblies (MEA) were prepared having the following configuration LST:YDC 50:50| YSZ (0.3mm) |LSM:YSZ 50:50 |LSM. The electrodes were prepared using spin coating of electrode materials suspensions onto YSZ disks (D = 2.5 cm, t = 0.3 mm, Fuel Cell Materials) using a spin coater (Cookson Electronics, Model No. P6204), drying, then sintering at 1200 °C for 2 h.

A SOFC setup with coaxial alumina tubes (inlet and outlet) was used for feeding fuel and air to the anode and cathode sides of the MEA, respectively, and removing effluent, as described previously [25]. Each MEA was sealed between the outer anode and cathode chamber tubes using glass sealant. Gold wire and gold mesh welded together were used as current collectors. A Pt wire connected to Pt formed from paste on the rim of YSZ disk was used as reference electrode to enable differentiation of anodic and cathodic behaviors. Feeds having different gas compositions were fed into the anode compartment of the cell with a flow rate of 20 $mL.min^{-1}$ while air was fed into the cathode side at 100 $mL.min^{-1}$. A mass spectrometer (Pfeiffer Thermostar GSD 301) and gas chromatograph (Agilent 6890N) equipped with sulfur chemiluminescence detector detector (SCD) (Sievers 355) were connected to the exhaust line to determine the outlet gas composition.

Potentiodynamic (PD) tests with a scan rate of 1 $mV.s^{-1}$ were performed to obtain the power densities of the cell when fed with different feed gases at different temperatures. EIS was

used to analyze the total polarization resistance of the cell. Potentiostatic (PS) tests were used to investigate the electrochemical stability of the cell fed with different fuels when the potential of the cell was adjusted at 0.2 V versus Pt-air reference electrode. Electrochemical tests including PD, PS and EIS were performed using a Solartron instrument (SI 1260) equipped with a frequency response analyzer.

TGA and DSC analyzes were acquired simultaneously (SDT-Q600) to analyze gel combustion reactions under He-O_2 (10%) atmosphere.

A Rigaku Geigerflex X-ray diffractometer (XRD) system with a Co tube (λ= 1.79026 Å) and a graphite monochromator was used to determine the purity of the synthesized powders, and MDI Jade 5 was used for phase identification. A Hitachi S-2700 scanning electron microscope (SEM) equipped with a PGT (PrincetonGamma-Tech) IMIX digital imaging system was used to characterize cross sections of MEAs and particles' morphologies.

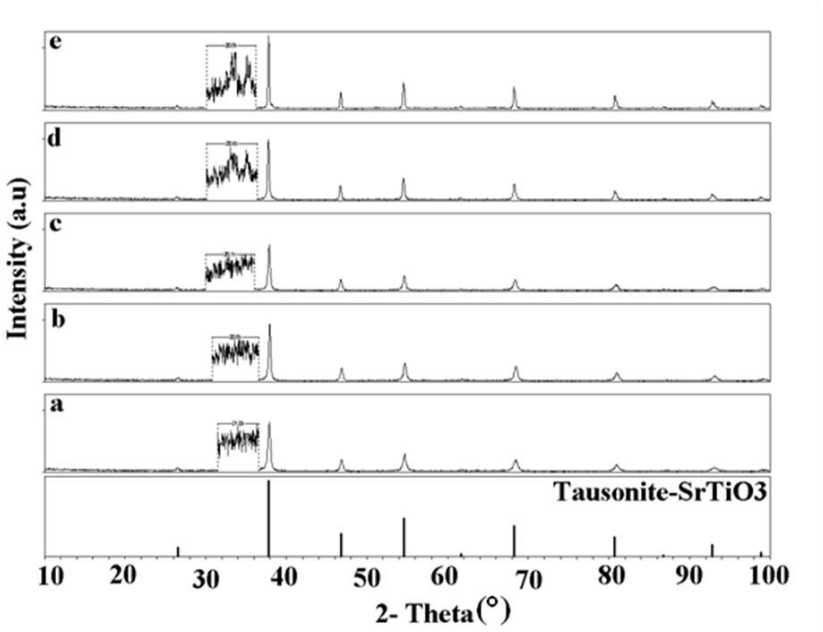

Figure 2. 1 XRD patterns of LST powder calcined at: (a) 900 °C; (b) 1200 °C; (c) 1300 °C; (d) 1400 °C; (e) 1600°C for 4 h in air.

2. 3. Results and discussion

2. 3.1. Materials characterization

Figure 2.1 shows the XRD patterns of LST powders synthesized at 550 °C and calcined at different temperatures. The patterns were refined based on the cubic perovskite structure of $SrTiO_3$ with powder diffraction file number (PDF) 35-0734. Cell parameters of the prepared powders changed as a function of calcination temperature starting from 3.90 Å at 900 °C and increased to 3.91 Å at a calcination temperature of 1600 °C. Two additional 2θ peaks between

30° and 35° were present for samples calcined at 1400 °C and 1600 °C, corresponding to additional phases reported previously[26,27]. Eror and Balachandran [27] ascribed the presence of one extra peak to the presence of secondary phase $La_2Ti_2O_7$ formed when exceeding 40 atom% of Sr substitution by La. They also considered 40 atom% of La as the solubility limit of this element into the SrTiO3 structure, which decreased the lattice parameter of the cell from 3.905 to 3.890 Å [26]. In contrast, Howard et al. [28] noticed that the lattice parameter increased as a consequence of La donor doping at the Sr sites under both oxidizing and reducing conditions. The differences between these reports may be a consequence of the different calcination temperatures and durations. The different lattice parameters now reported appear to be a consequence of the effects of preparation conditions on the structural development of this material.

Figure 2.2 shows the X-ray diffraction pattern of $Y_{0.2}Ce_{0.8}O_{1.9}$ (YDC) synthesized using the citrate nitrate combustion method at 350 °C and calcined at 900 °C for 4 h. This structure was related to the cubic fluorite structure of CeO_2 (PDF 65-2975). The refined cell parameter for the synthesized YDC was 5.41 Å with average crystallite size of 43 nm for the sample calcined at 900 °C.

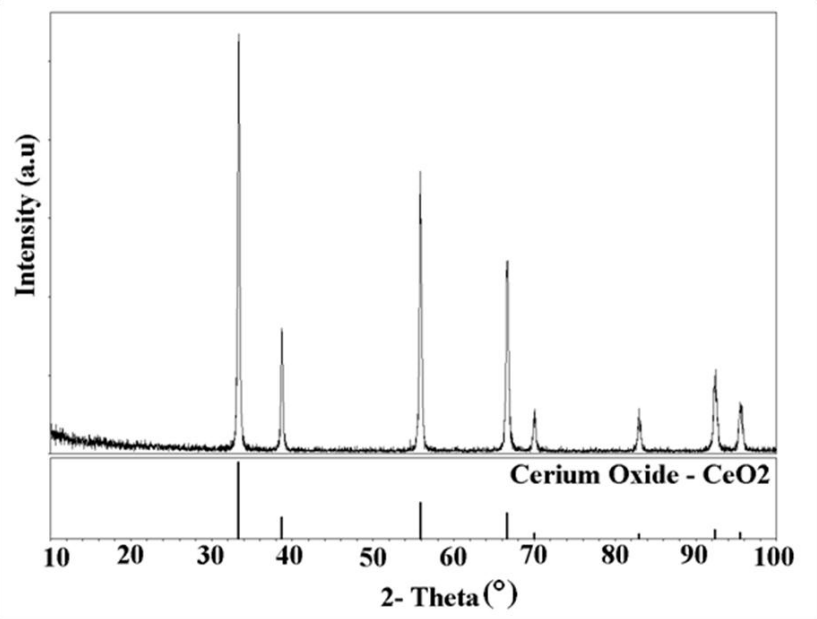

Figure 2. 2 XRD pattern of YDC calcined at 900 °C for 4 h in air.

Scanning electron micrographs of the anode and cathode layers on YSZ disks prepared at 1200 °C for 2 h are shown in Figure 2.3. Uniform anode (LST: YDC 50:50) and cathode (LSM: YSZ 50:50 | LSM) porous layers with respective average thickness of 12 µm and 23 µm were applied using spin coating.

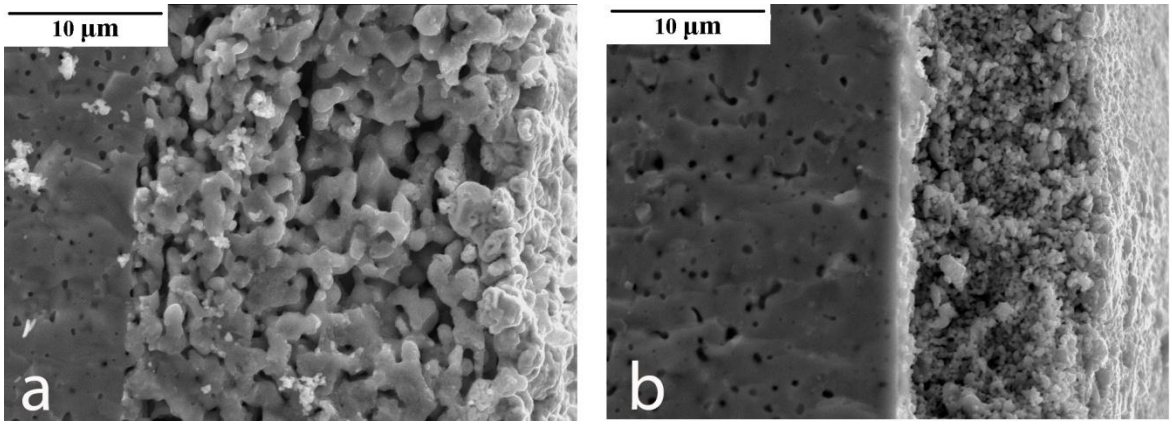

Figure 2. 3 SEM micrograph of SOFC's MEA: (a) cathode and (b) anode sides.

2. 3. 2 Electrochemical analyses

2. 3. 2. 1. Electrochemical performance

Performances of MEA fed with different fuels are compared in Figure 2.4. The maximum power density of the cell fuelled with syngas having 0.5% H_2S was greater than that using sweet syngas, 169 $mW.cm^{-2}$ and 102 $mW.cm^{-2}$ respectively at 850 °C. The maximum current density also increased from 393 $mA.cm^{-2}$ to 939 $mA.cm^{-2}$ when 0.5% H_2S was included in 40% H_2 balanced with CO (syngas). In contrast, the maximum power density and current density obtained by the cell (39 $mW.cm^{-2}$ and 87 $mA.cm^{-2}$) in 0.5% H_2S balanced with Ar was considerably lower than the difference between those obtained using as feed either syngas or H_2S-containing syngas. Thus conversion of H_2S itself was not the sole cause of the increment in performance [23].

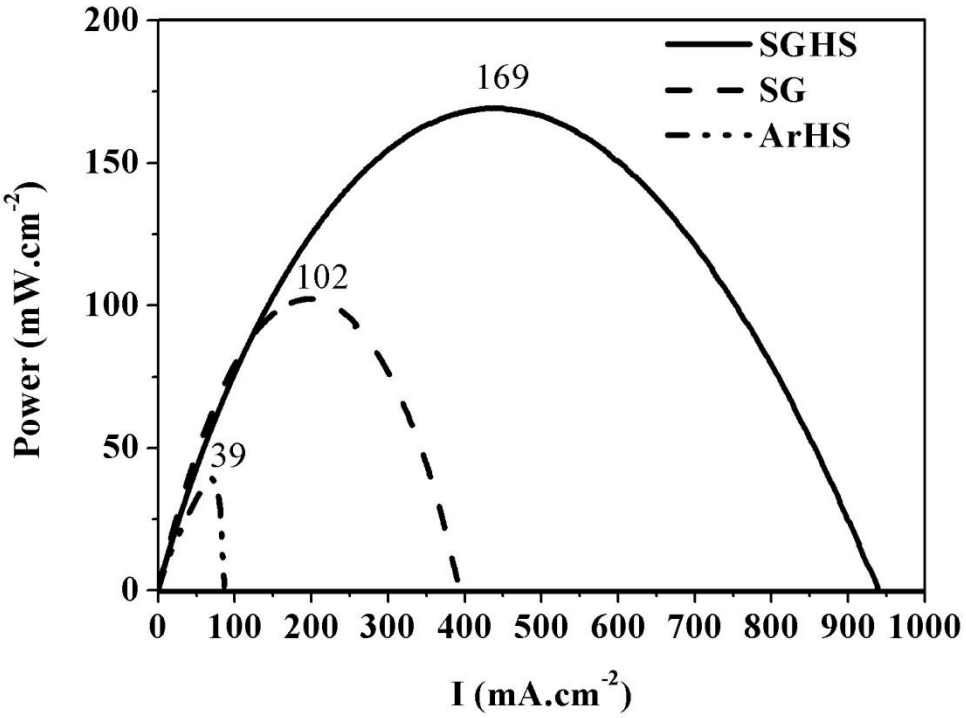

Figure 2. 4 Electrochemical performance at 850 °C of an MEA having the structure LST:YDC 50:50 | YSZ | LSM:YSZ 50:50 | LSM fed with different fuels (SG is syngas; HS0.5 is 0.5%H_2S).

A power density enhancement in the presence of H_2S also was reported for use of anodes comprising LSV [29], LST [12,23] with perovskite structure, and $Ga_2Ti_{1.4}Mo_{0.6}O_7$ [30] with pyrochlore structure. However, the enhancement of power density is in contrast to reported data for other materials including various cermets and the well known LSCM perovskite base material. Marina and Pederson also reported power density loss when using an anode material made by comprising a mixture of LST and ceria when 100 ppm H_2S was added into humidified

hydrogen [15]. Hence the observed effect is neither general nor unique, but is a consequence of interaction between specific anodes and the H_2S present in the anode feed.

2.3. 2. 2. Electrochemical impedance spectroscopy

Figure 2.5 shows the EIS data for the anode when syngas and H_2S-containing syngas under each of humidified and dry conditions was fed into the anode compartment of the cell. The EIS results were fitted based on the appendix A. The variation of natural logarithm of the total polarization of the cell also is plotted vs. inverse of temperature. The total polarization resistance of the cell, R_p, increased from 12 $\Omega.cm^2$ to 43 $\Omega.cm^2$ in dry feed and from 4 $\Omega.cm^2$ to 10 $\Omega.cm^2$ in humidified feed when H_2S was present at 850 °C. In order to determine the effect of the polarization on the impedance, the cell impedance was measured at different overpotentials (Figure 2.6). The total impedance of the cell decreased with increase in the overpotential of the system for both syngas and H_2S-containing syngas feeds. Total polarization resistance of the cell decreased from 44.7 $\Omega.cm^2$ to 5.7 $\Omega.cm^2$ and from 22.1 $\Omega.cm^2$ to 4.8 $\Omega.cm^2$ for H_2S-containing syngas and syngas fuels, respectively, by increasing the overpotential of the cell from OCV to 300 mV. In fact, the impedance reduction rate was faster for H_2S-containing syngas where it converged to the same impedance value as for the syngas feed at 300 mV. After switching back to OCV, the impedance of the cell gradually returned to the original value before biasing the cell.

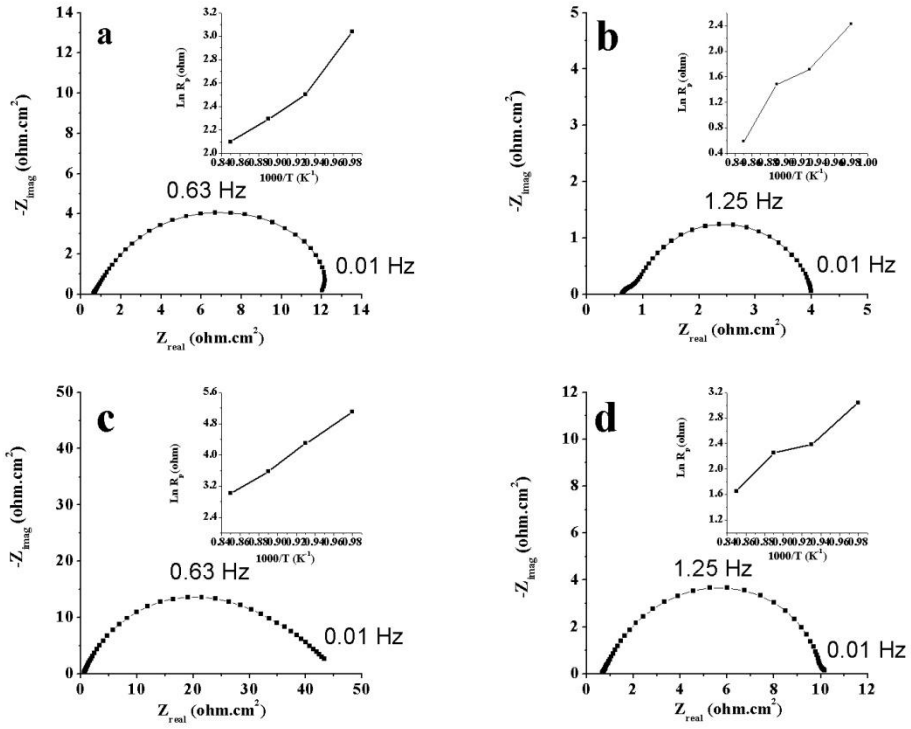

Figure 2. 5 i. Electrochemical impedance spectra of MEA having the structure LST: YDC 50:50 | YSZ | LSM: YSZ 50:50 | LSM MEA when fuelled by: (a) syngas, (b) humidified syngas, (c) syngas–0.5% H_2S and (d) humidified syngas–0.5% H_2S at 850, ii. Ln Rp vs. operating temperature.

The data from the impedance spectra showed that the total polarization resistance of the cell increased as a result of the presence of H_2S; however, the peak power density of the cell also was increased by H_2S presence in the feed. This effect may be a consequence of coverage of the TPBs by adsorption of sulfur species, mainly inactive S_2 at OCV, the effect of which would be increased impedance of the overall system. In contrast, polarization of the cell can form other

types of sulfur species with the effect of improving the catalytic activities of the anode forming intermediate species with the feed components.

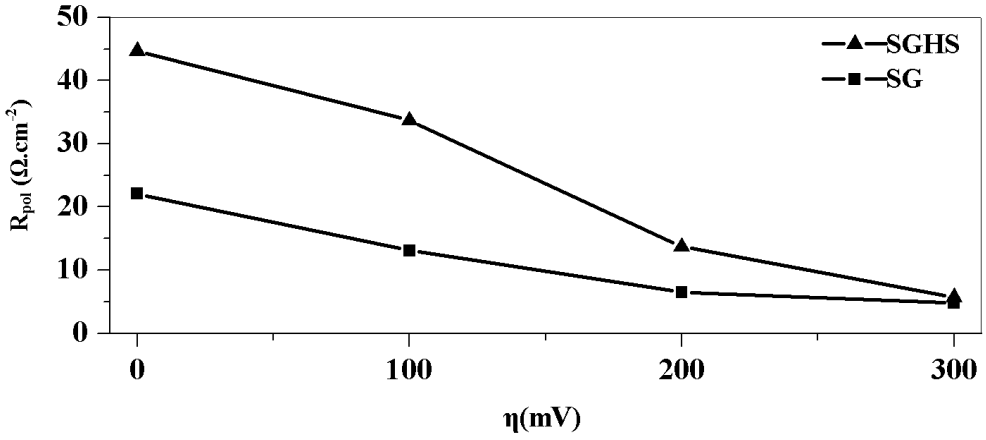

Figure 2. 6 Dependence of polarization resistance on overpotential of the cell when syngas or 0.5% H_2S-syngas was used as fuel at 850 °C.

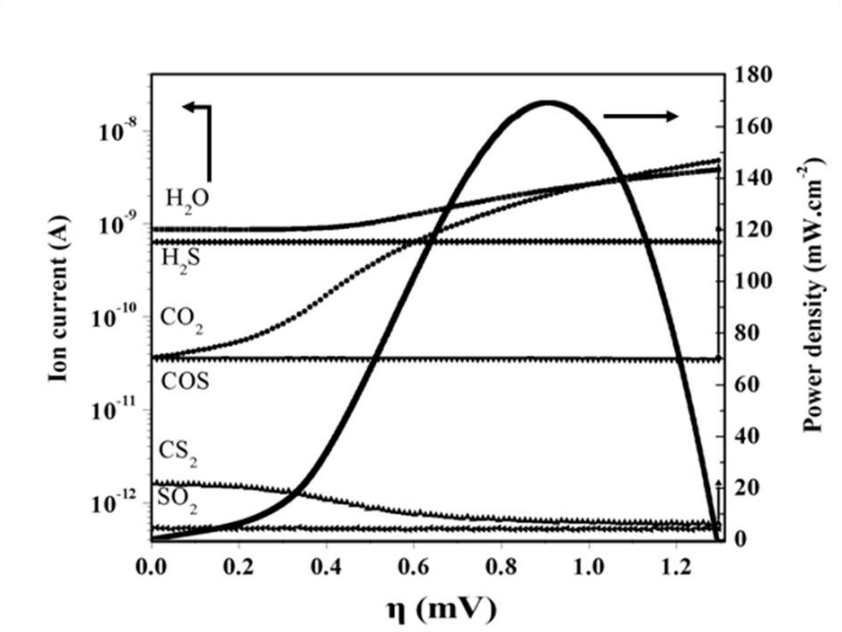

Figure 2. 7 Correlation of MS peaks for the effluent and power density as a function of overpotential of the cell having a MEA with structure LST: YDC 50:50 | YSZ | LSM: YSZ 50:50 | LSM MEA fed with dry syngas containing H_2S (0.5%) at 850 °C.

2. 3. 3. Gas analyses

2. 3.3.1. Mass spectroscopy

Dynamic gas analysis of the exhaust gas was performed using mass spectrometric (MS) analyses during potentiodynamic tests. In these tests the cell potential was ramped from OCV to 0 V at 1 mV.s^{-1}. The outlet tube was connected to the mass spectrometer. The effluent gas components (other than H_2 and CO) detected using mass spectrometry are shown in Figure 2.7. H_2O and CO_2 were the main products of the electrochemical reactions, produced by the

oxidation of H_2 and CO, respectively. H_2S, CS_2, COS and SO_2 also were detected in lower amounts. The main product of the reaction between CO and H_2S was COS with a concentration about 280 ppm which was close to the thermodynamic equilibrium value (300 ppm). Following gas evolution with time during each potentiodynamic run showed that CO_2 and H_2O production increased in parallel with the current density of the cell. The variations in concentrations of H_2S and SO_2 with potential were compared for 0.5% H_2S-containing argon and 0.5% H_2S-containing syngas (Figure 2.8). These revealed the different roles of H_2S in these two different feeds. H_2S was the only consumable gas in H_2S-Ar which could be electrochemically oxidized in the SOFC by reacting with O^{2-} ions. In this case, SO_2 was produced. In contrast, no H_2S was consumed and there was no detectable amount of SO_2 produced when H_2S-containing syngas was used. Therefore H_2S consumption was not the source of power generated from conversion of syngas-H_2S over the present catalyst, a finding parallel to that for CH_4-H_2S fuelled SOFC [23].

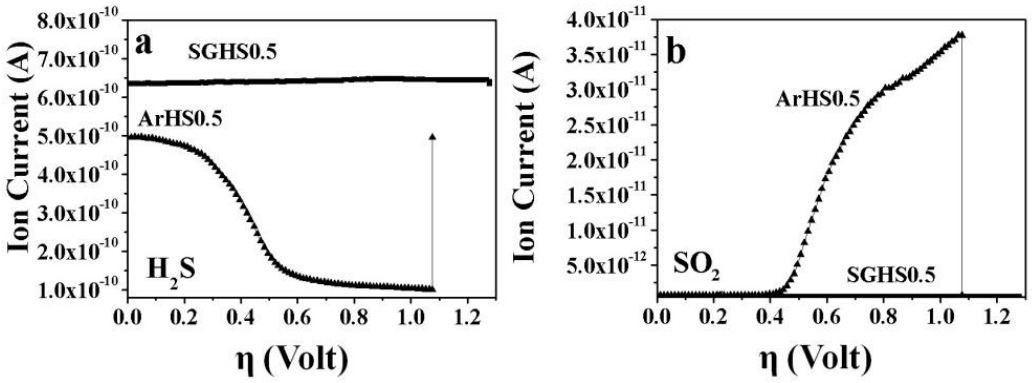

Figure 2. 8 Mass spectroscopic analyses of the exhaust gas for (a) H_2S and (b) SO_2 gas peaks at different voltages operating with syngas–H_2S (0.5%) feed at 850 °C.

Table 2. 1 GC analyses of the outlet gas stream when H_2S containing syngas fueled the cell under potentiostatic conditions (850 °C, 20 mL.min^{-1}). RT refers to room temperature data for comparison.

	RT	OCV	1V	0.8V	0.6V	0.4V	0.2V	0.04V
H_2 (mol%)	40	40	39.4	38.3	34.9	32.5	29.8	26.3
CO (mol%)	59.5	59.4	59.1	58.3	54.8	50.70	42.6	41.6
H_2S (ppm)	5000	4570	4570	4528	4505	4345	4526	4500
CO_2 (mol%)	0	0.06	0.40	1.6	4.6	11.46	16.8	17.9
H_2O (mol%)	0	0	0.6	1.7	5.1	7.5	10.2	13.7
COS (ppm)	0	439	430	413	411	426	412	437

2. 3. 3. 2. Gas chromatography

Based on the MS analyses, it was confirmed that H_2S consumption did not occur during electrochemical oxidation of the syngas feed and no SO_2 was detected during potentiodynamic runs at 1 $mV.s^{-1}$. In addition, gas chromatographic (GC) analyses were used to determine the gas composition under potentiostatic conditions and investigate their variation with time. Table 2.1 shows the gas composition of the exhaust gas measured using GC analyses under potentiostatic conditions at different potentials. Although the concentrations of CO and H_2 were decreased by oxidation to CO_2 and H_2O, the concentration of H_2S remained constant and no SO_2 production was detected using GC fitted with a sulfur detector. Conversion of the syngas increased from 21% to 27% when 0.5% H_2S was present in the feed at 0.2 V and 850 °C. Thus the presence of H_2S enhanced feed conversion while itself was not converted in the electrochemical oxidation reaction. Furthermore, gas analyses showed that the presence of H_2S significantly enhanced the rate of CO oxidation when compared to H_2 oxidation at 0.2 volt. At the same flow rate CO_2 production was increased three-fold from 5% to 16.8% when H_2S was present. However, the parallel H_2O production decreased from 16% to 10% of the feed concentration. In addition, a similar concentration close to 400 ppm COS was detected at all applied potentials.

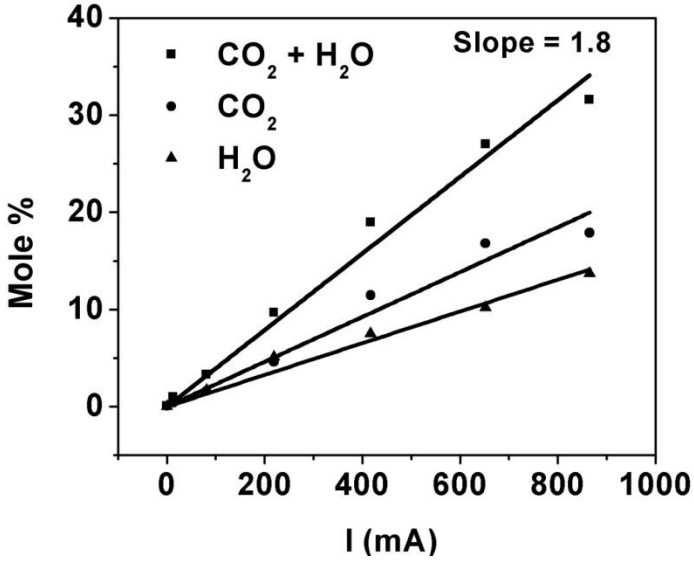

Figure 2. 9 Variations of CO_2 and H_2O concentrations (GC analysis) as a function of current produced by electrochemical oxidation of the fuel (syngas containing 0.5% H_2S) at 850 °C.

Figure 2.9 shows the variations of CO_2 and H_2O concentrations with current when 0.5% H_2S-containing syngas fuelled the cell at 850 °C. Faraday's law (Equation 2.1) was used to verify the charge balance of the electrochemical reactions:

$$\mathrm{I\ (A)} = \frac{\mathrm{WnF}}{\mathrm{Mt}} \tag{2.1}$$

where I is the total current in amperes, W/M is the total moles of the converted gas, F is Faraday's constant, t is the time and n is the number of electrons per mole transferred in the electrochemical reaction. The value of n was calculated to be 1.8 ± 0.2 at 850 °C by using the

slope of the line when H_2S-containing syngas fuelled the cell, and this value was close to that for electrochemical oxidation of both CO and H_2 (n = 2).

2.3.4. Mechanism

H_2S can be directly oxidized in a fuel cell by its electrochemical reactions with O^{2-} ions, generating electrons (Equations 2.2, 2.3) [11,31]. In addition, H_2S also can be dissociated at high temperature into H- and S-containing species (Equation 2.4). After that, hydrogen and sulfur each can take part in electrochemical oxidation reactions (Equations 2.5, 2.6). Hence the reaction path in a particular circumstance will depend on the temperature, current and types of catalysts used for the anode [32].

$$H_2S + O^{2-} \rightarrow {}^1/_2\, S_2 + H_2O + 2e^- \quad (2.2)$$

$$H_2S + 3O^{2-} \rightarrow SO_2 + H_2O + 6e^- \quad (2.3)$$

$$H_2S \rightarrow {}^1/_2\, S_2 + H_2 \quad (2.4)$$

$$H_2 + O^{2-} \rightarrow H_2O + 2e^- \quad (2.5)$$

$${}^1/_2\, S_2 + 2O^{2-} \rightarrow SO_2 + 4e^- \quad (2.6)$$

Therefore it would appear that one possible explanation for the power and current density enhancement arising from inclusion of H_2S in the feed could be direct or indirect electrochemical oxidation of H_2S. However, in such a case consumption of H_2S would lead to formation of SO_2

and H_2O, whereas gas analyses showed that no SO_2 was produced and that the H_2S concentration remained constant at different potentials. In contrast, H_2S was completely consumed and produced SO_2 when 0.5% H_2S in Ar was used as the feed at 0.2 V. These results show that H_2S itself was not consumed in the generation of electrical power from conversion of syngas containing H_2S, and that conversions of H_2 and CO were the main electrochemical oxidation reactions for generating power. Vincent et al. [23] showed that SO_2 was not produced for voltages higher than 0.59 V when H_2S was balanced with methane. They showed that the presence of H_2S played an important role in methane oxidation, but was not consumed. Among other observations, they proved that the gain in performance could not be explained as simply a result of H_2S oxidation. Below 0.59 V, SO_2 appeared in the gas composition followed by a drop of CO_2 and CS_2 concentrations. In contrast, we did not observe SO_2 production even at high overpotentials. The differences between these two systems originate from the nature of feeds (syngas or methane) and the different compositions of mixtures in the in-situ thermodynamic equilibria, in particular the intermediate concentration of H_2. By comparison with the data for conversion of methane, it appears that in the present case the higher level of H_2 present in syngas fuel inhibited SO_2 production (Table 2.1).

As confirmed by GC and MS gas analyzes, electro-oxidation of the feed significantly improved when 0.5% H_2S was present in the feed. However, the role of H_2S is not yet sufficiently clear to fully discriminate between possible reactions paths. One possibility is that

reaction between CO and H_2S at high temperature leads to formation of intermediate species which are more electrochemically active than CO itself (e.g. Equations 2.7, 2.8) [33].

$$CO + H_2S \leftrightarrow COS + H_2 \;\; \Delta G_{850} = 29.108 \text{ KJ} \tag{2.7}$$

$$2COS \leftrightarrow CS_2 + CO_2 \;\; \Delta G_{850} = 4.81 \; KJ \tag{2.8}$$

Alternatively, H_2S could be dissociated into fragments on the catalyst surface (Equation 2.9) [34], and the presence of these active species could enhance the activity of the surface by changing the catalytically active sites and thereby the reaction path into a more favourable direction. The present data suggest strongly that at least one intermediate compound is formed which is more readily electrochemically oxidized than the components of syngas [23,33]. Beck et al. [35] proposed a similar process for the activation by TiO_2 as a catalyst for CO conversion into COS by reaction with H_2S.

$$H_2S \rightarrow HS^* + H^* \text{ or } 2H^* + S^* \tag{2.9}$$

The Gibbs free energy of each reaction (2.10, 2.11) shows that COS formation is more favorable in the presence of HS and S species on the surface of the catalyst when compared to straightforward reaction of CO and H_2S at 850 °C (Equation 2.7).

$$2CO + 2HS^* \rightarrow 2COS^* + H_2 \;\; \Delta G_{850} = -125.96 \text{ KJ} \tag{2.10}$$

$$CO + S^* \rightarrow COS^* \; \Delta G_{850} = -20.11 \text{ KJ} \tag{2.11}$$

Reaction of COS with H_2O produced by electrochemical oxidation of fuel components is thermodynamically favorable for production of CO_2 and H_2S (Equation 2.12). H_2S would be reformed in such a reaction sequence, and thus would present a constant concentration in the effluent gases.

$$COS + H_2O \leftrightarrow CO_2 + H_2S \;\; \Delta G_{850} = -28.07 \text{ KJ} \qquad (2.12)$$

Hence, to determine the exact mechanism path for electrochemical oxidation of syngas requires data, not presently available, from *in situ* gas chemical analyses and surface analyses of the catalysts.

2. 3. 4. Stability tests

2. 3. 4. 1. Electrochemical stability

The electrochemical stability of the MEA was investigated under potentiostatic conditions when different fuels were fed into the anode compartment (Figure 2.10). H_2, syngas and H_2S-containing syngas were successively fed into the same cell. Then, the feed was cycled back to syngas and then H_2 to check the reproducibility of the results. The LST-YDC anode was electrochemically stable in each of these feeds. Also, there was no loss of performance when 0.5% H_2S was present in syngas feed during runs up to 75 h. Unexpectedly, the power density of the cell was enhanced over time while H_2S-containing syngas was the fuel. However, when the feed was reverted to sweet syngas the performance of the cell then dropped steadily to restabilize at its original value, before the inclusion of H_2S in the feed. This showed that the effects of the

sulfur species on the reactive sites of the catalyst were recoverable. This recovery process needs time for complete removal of inactive sulfur species (S_2) from the active sites of the catalysts. In addition, current collection problem would be another possible reason for this degradation effect over operating time, the effect of which would prevent complete recovery of the performance. XPS analysis of the anode of the cell membrane after exposure to the sequence of feeds showed the presence of 0.25% elemental sulfur (S_2) without any trace of sulfide (S^{2-}).

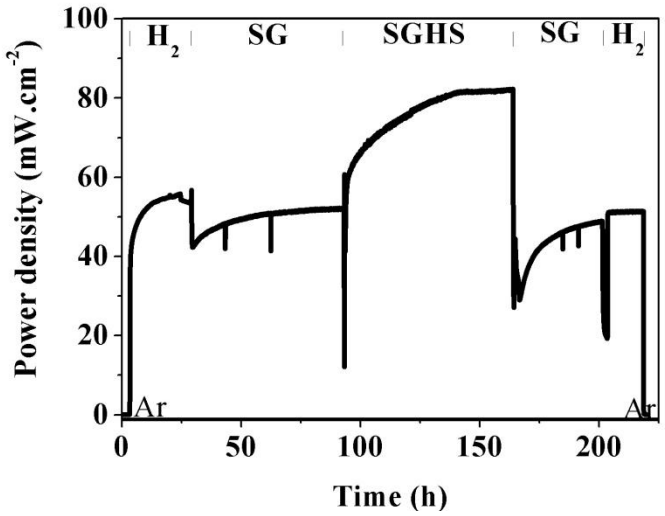

Figure 2. 10 Electrochemical stability test for the MEA having the structure LST: YDC 50:50 | YSZ | LSM: YSZ 50:50 | LSM under potentiostatic (E = 0.2 volt) condition at 850 °C when fed with different gases.

2.3.4.2 Chemical stability

To examine the chemical stability of the anode material in H_2S-containing feed a sample of the LST-YDC mixture was exposed to various feeds at 850 °C for 48 h. Figure 2.11 shows the XRD patterns for LST-YDC mixtures exposed to each of air, syngas and H_2S-containing syngas, respectively. Comparing these three XRD patterns showed that LST is stable in either oxidizing or reducing atmospheres and in the presence of H_2S. There were no peak shifts for LST. In contrast, different crystal structures were formed from YDC in the different atmospheres. YDC has the fluorite crystal structure similar to CeO_2 in oxidizing atmosphere. In contrast, YDC was partially reduced in the reducing atmosphere provided by syngas and Ce_2O_3 with hexagonal structure was detected. In H_2S-containing syngas, the peaks corresponding to the CeO_2 structure were greatly diminished and were replaced by those for Ce_2O_2S. It is known that different cerium oxides and sulphides are stable under different conditions, depending on the partial pressures of O_2 and sulfur [36,37]. Ce_2O_2S and CeO_{2-x} are the most stable species at high partial pressure of S_2 and low partial pressure of O_2, respectively. Reversing the feed from H_2S-containing syngas to syngas did not reverse the change of the structure back to Ce_2O_3 from Ce_2O_2S.

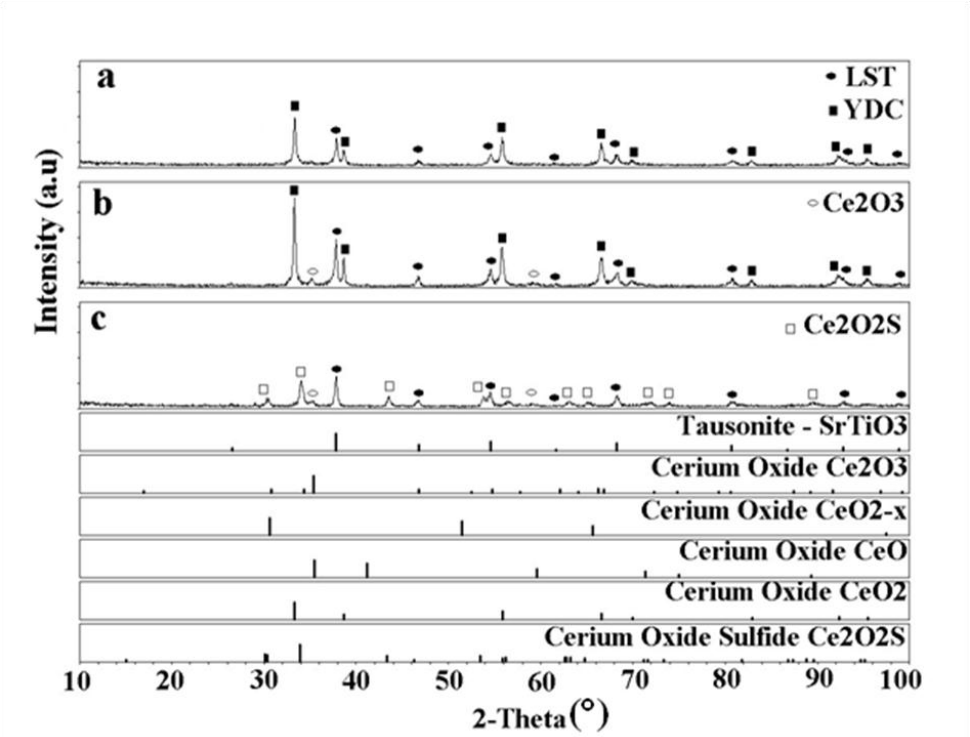

Figure 2. 11 XRD patterns for LST–YDC powder mixture prepared at 1200 °C for 2 h and then exposed to: (a) air: (b) syngas: and (c) syngas – H_2S (0.5%) at 850 °C for 48 h.

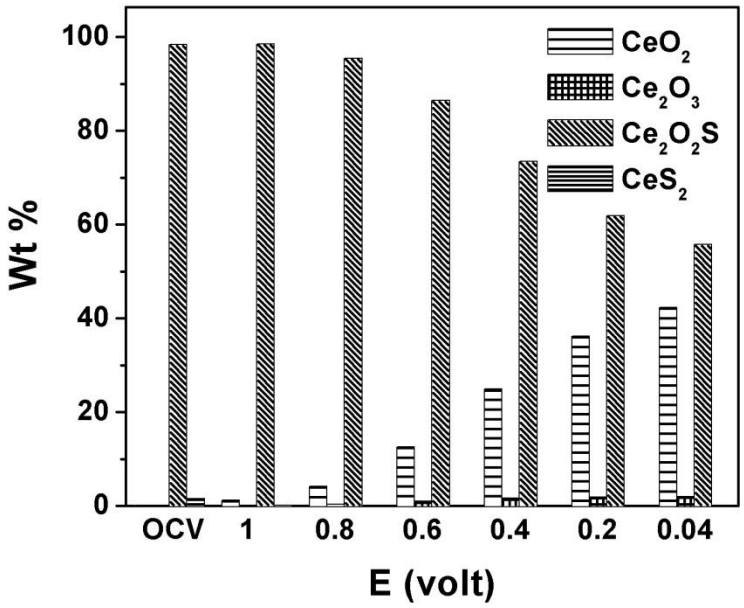

Figure 2. 12 Variations of different cerium species' concentrations with applied potential under potentiostatic conditions (thermodynamic calculations based on gas composition) at 850 °C.

These results showed that LST-YDC composite is electrochemically stable as an anode material in high concentration H_2S-containing syngas, whereas CeO_2 was not chemically stable in the same feed. There was electrochemical and performance stability of the cell when operated under potentiostatic conditions. Figure 2.12 shows the calculated thermodynamic values in weight percent of different cerium species present after the catalyst was operated in H_2S-containing feed under potentiostatic conditions using different gas compositions (GC analyses). Ce_2O_2S was the main stable species at OCV and low applied voltage. CeO_2 was present after

increasing the applied voltage of the cell to more than 0.8 V and reached a maximum value around 40 wt% at 0.04 V. Consequently, CeO_2 becomes can thermodynamically stable when the cell was biased as a consequence of increasing the water content.

2.4 Conclusions

Active $La_{0.4}Sr_{0.6}TiO_{3\pm\delta}$: $Y_{0.2}Ce_{0.8}O_{1.9}$ (LST:YDC) 50:50 composite anodes can be prepared using materials manufactured from a modified citrate-nitrate gel combustion method and applying a suspension onto YSZ electrolyte disks by spin coating. Potentiostatic electrochemical tests showed that LST:YDC is electrochemically stable when 0.5% H_2S-containing syngas was used as fuel in SOFC. The presence of H_2S enhanced the performance of the cell. However, the H_2S concentration remained unchanged during potentiodynamic and potentiostatic runs, and so conversion of H_2S itself was not the source of the enhanced performance. MS and GC gas analysis showed that CO oxidation was improved three-fold in the presence of 0.5% H_2S. The role of H_2S may include formation of intermediate sulfur species in the syngas electrochemical oxidation, with regeneration of H_2S, with the net effect that H_2S is not consumed during the process but instead facilitates oxidation of CO by changing the reaction path.

2.5 References

[1] G.J.K. Acres, Journal of Power Sources 100 (2001) 60–66.

[2] K. Hassmann, Fuel Cells 1 (2001) 78–84.

[3] T. Setoguchi, K. Okamoto, K. Eguchi, H. Arai, J. Electrochem. Soc. 139 (1992) 2875–2880.

[4] M. Mori, T. Yamamoto, H. Itoh, H. Inaba, H. Tagawa, J. Electrochem. Soc. 145 (1998) 1374–1381.

[5] S. Jiang, S. Chan, MATERIALS SCIENCE AND TECHNOLOGY 20 (2004) 1109–1118.

[6] B.C.H. Steele, Solid State Ionics 86-88 (1996) 1223–1234.

[7] T. Kim, G. Liu, M. Boaro, S.-I. Lee, J.M. Vohs, R.J. Gorte, O.H. Al-Madhi, B.O. Dabbousi, Journal of Power Sources 155 (2006) 231–238.

[8] W. Zhu, C. Xia, J. Fan, R. Peng, G. Meng, Journal of Power Sources 160 (2006) 897–902.

[9] Y.M. Choi, C. Compson, M.C. Lin, M. Liu, Chemical Physics Letters 421 (2006) 179–183.

[10] K. Sasaki, K. Susuki, A. Iyoshi, M. Uchimura, N. Imamura, H. Kusaba, Y. Teraoka, H. Fuchino, K. Tsujimoto, Y. Uchida, N. Jingo, J. Electrochem. Soc. 153 (2006) A2023–A2029.

[11] M. Gong, X. Liu, J. Trembly, C. Johnson, Journal of Power Sources 168 (2007) 289–298.

[12] R. Mukundan, E.L. Brosha, F.H. Garzon, Electrochem. Solid-State Lett. 7 (2004) A5–

A7.

[13] O.A. Marina, N.L. Canfield, J.W. Stevenson, Solid State Ionics 149 (2002) 21–28.

[14] S. Tao, J.T.S. Irvine, Nat Mater 2 (2003) 320–323.

[15] O.. Marina, L.. Pederson, In: J. Huijsmans, Editor, Fifth European Solid Oxide Fuel Cell Forum, European Fuel Cell Forum, Oberrohfdorf, Switzerland (2002) 481–489.

[16] J.C. Ruiz-Morales, J. Canales-Vázquez, C. Savaniu, D. Marrero-López, W. Zhou, J.T.S. Irvine, Nature 439 (2006) 568–571.

[17] Q.X. Fu, F. Tietz, D. Stover, J. Electrochem. Soc. 153 (2006) D74–D83.

[18] H. Kurokawa, L. Yang, C.P. Jacobson, L.C. De Jonghe, S.J. Visco, Journal of Power Sources 164 (2007) 510–518.

[19] S. Hilaire, X. Wang, T. Luo, R.J. Gorte, J. Wagner, Applied Catalysis A: General 215 (2001) 271–278.

[20] T. Bunluesin, R.J. Gorte, G.W. Graham, Applied Catalysis B: Environmental 15 (1998) 107–114.

[21] S. Park, R.J. Gorte, J.M. Vohs, Applied Catalysis A: General 200 (2000) 55–61.

[22] N. Laosiripojana, S. Assabumrungrat, Applied Catalysis B: Environmental 60 (2005) 107–116.

[23] A.L. Vincent, J.-L. Luo, K.T. Chuang, A.R. Sanger, Applied Catalysis B: Environmental In Press, Accepted Manuscript (n.d.).

[24] F. Deganello, G. Marcì, G. Deganello, Journal of the European Ceramic Society 29 (2009) 439–450.

[25] N. Danilovic, J.-L. Luo, K.T. Chuang, A.R. Sanger, Journal of Power Sources 192 (2009) 247–257.

[26] U. Balachandran, N.G. Eror, J American Ceramic Society 64 (1981) c–75–c–76.

[27] N.G. Eror, U. Balachandran, Journal of Solid State Chemistry 40 (1981) 85–91.

[28] S.A. Howard, J.K. Yau, H.U. Anderson, J. Appl. Phys. 65 (1989) 1492.

[29] L. Aguilar, S. Zha, Z. Cheng, J. Winnick, M. Liu, Journal of Power Sources 135 (2004) 17–24.

[30] S. Zha, Z. Cheng, M. Liu, Electrochem. Solid-State Lett. 8 (2005) A406–A408.

[31] M. Liu, G. Wei, J. Luo, A.R. Sanger, K.T. Chuang, J. Electrochem. Soc. 150 (2003) A1025–A1029.

[32] N.U. Pujare, K.J. Tsai, A.F. Sammells, J. Electrochem. Soc. 136 (1989) 3662–3678.

[33] F. Faraji, I. Safarik, O.P. Strausz, M.E. Torres, E. Yildirim, Industrial & Engineering Chemistry Research 35 (1996) 3854–3860.

[34] C. Yanxin, J. Yi, L. Wenzhao, J. Rongchao, T. Shaozhen, H. Wenbin, Catalysis Today 50 (1999) 39–47.

[35] D.D. Beck, J.M. White, C.T. Ratcliffe, The Journal of Physical Chemistry 90 (1986) 3123–3131.

[36] P. Lohsoontorn, D.J.L. Brett, N.P. Brandon, Journal of Power Sources 175 (2008) 60–67.

[37] R.M. Ferrizz, R.J. Gorte, J.M. Vohs, Applied Catalysis B: Environmental 43 (2003) 273–280.

Chapter 3

Impregnation of LDC and LST into porous YSZ for SOFC anodes

3.1 Introduction

High conversion efficiency and fuel flexibility are among the considerable advantages of using SOFCs as reliable energy conversion systems [91,92]. In order to achieve these, anode material design is one of the main challenges in SOFC development. Ni-based cermets have been extensively used as anode materials with the highest electrocatalytic activity towards H_2 oxidation, and they are compatible with YSZ electrolytes [93,94]. However, redox instability and carbon deposition are problematic issues when using hydrocarbon-containing fuels. Ceramic based anode materials with high redox stability [95] and low propensity for carbon deposition [23,96] should be used instead of Ni based anode materials when using hydrocarbons as feeds. Different perovskite based oxides have been investigated for conversion of various feeds. Among them, LSCM showed the highest electrocatalytic activity when using H_2 as fuel, comparable to that of Ni-YSZ anodes [97]. Strontium titanate based materials offer high electronic conductivity when compared to other perovskite based materials in reducing atmospheres [50,56]. However, they do not have high electrocatalytic activity because of the low oxide ion conductivity in this structure [48]. In addition to high electronic conductivity and redox stability, the chemical stability of strontium titanate based anode materials in feeds containing

high concentrations of H_2S is advantageous when compared to other active anode materials [49]. Different approaches have been investigated to improve the electrocatalytic activity of strontium titanate based materials including doping at either Sr sites or Ti sites, and use of composites in combination with ionic conductor materials and catalysts [58,69,98].

In addition to materials selection for use as anode catalyst, the structure is also one of the most important issues for anode development. Conventional anode preparation methods have some drawbacks including: high preparation temperature; different sintering conditions for anode and electrolyte which cause cracking and/or delamination; and redox problems. In contrast, impregnation is an effective method for preparing electrode materials for SOFC applications. Independent sintering temperatures for different components, decreasing the preparation temperature for formation of catalysts so as to reduce their particle sizes, and extending the TPBs are among the benefits of using this method for electrode preparation [99,100].

Different electrode materials have been impregnated as catalysts in cathodes [101–107] and anodes [108–112]. Cathodes materials including $La_{0.8}Sr_{0.2}MnO_3$ [113], $La_{0.6}Sr_{0.4}CoO_{3-\delta}$ [114], $La_{0.8}Sr_{0.2}FeO_3$ [115], $LaNi_{0.6}Fe_{0.4}O_3$ [116], $Ce_{0.8}Sm_{0.2}O_{1.9}$ (SDC) [101], $La_{0.6}Sr_{0.4}Co_{0.2}Fe_{0.8}O_{3-\delta}$ [102] and $La_{0.6}Sr_{0.4}Co_{0.8}Ni_{0.2}O_{3-\delta}$ [103] were prepared by wet impregnation. This approach also has been used extensively for development of anode materials for SOFCs. Vohs et al. [117] developed Cu-ceria/YSZ anode material by impregnation of Cu and ceria into a porous YSZ structure prepared using graphite and PMMA as pore formers and heating in air to 1550 °C. This anode material was introduced as a replacement for Ni based

anodes as it has higher stability in hydrocarbon feeds [117]. However the lower thermal stability of Cu at high operating temperatures in reducing atmospheres is a challenging issue.

LSCM was prepared in situ by impregnating a solution of appropriate metal nitrates into porous YSZ with ~65 wt% porosity [118]. This anode material showed higher thermal stability when compared to the Cu-ceria/YSZ anode system. Addition of 0.5 wt% Pd and 0.5 wt% ceria significantly improved the catalytic activity of this anode in humidified H_2 and methane. $La_{0.3}Sr_{0.7}TiO_3$ (L3ST) was impregnated into the same porous structure using an aqueous solution containing appropriate ions followed by calcination in air between 1100 °C and 1300 °C [119]. The results showed poor electrocatalytic activity of this material toward H_2 oxidation with lower power density, 20 $mW.cm^{-2}$, in humidified H_2 at 800 °C when compared to LSCM as anode. This difference was attributed to the lower ionic conductivity of L3ST when compared to LSCM. In addition, the difference between the morphologies of L3ST and LSCM deposits may be another reason for such an activity difference. The LSCM deposit was evenly spread throughout the YSZ structure and the impregnated material formed a porous microstructure in reducing atmosphere. In contrast, L3ST formed particles on the YSZ structure, which can be attributed to the low wettability of L3ST precursor solution on the YSZ structure [119]. It also was shown that L3ST and YSZ surfaces bond weakly even after sintering at 1500 °C [120].

$La_{0.4}Sr_{0.6}TiO_3$ (L4ST) is another material among potential candidates for use as an anode material, with which different feeds can be used to fuel the cell, especially for fuels having high concentrations of H_2S. It has been reported that it was a chemically and electrochemically stable anode material when H_2S (0.5%)-containing syngas (CO: H_2 6:4) and CH_4 were used to fuel the

cell [121,122]. In addition, the performance of the catalyst was improved in the presence of H_2S (0.5%) when using the composites L4ST-YSZ and L4ST-YDC. It was found that the presence of high concentrations of H_2S catalytically activated the electrochemical oxidation of hydrocarbons on the surface of L4ST [121,122].

In the present study, we describe the activities and structures of anode catalysts prepared by impregnation of $La_{0.4}Sr_{0.6}TiO_3$ (L4ST) into porous YSZ. In addition, we show the effect of co-impregnation with $La_{0.4}Ce_{0.6}O_{1.8}$ (LDC) on the electrochemical activity of these anodes in H_2 fuel. The reasons for LDC in improving the fuel cell performance will be discussed.

3.2 Experimental

Porous YSZ layers were obtained by sintering a mixture of YSZ (Tosoh) and graphite 40 wt% powders. A paste was prepared by mixing the powders with α-terpineol (Alfa Aesar): isopropanol 2:1 as a solution containing poly(vinyl butyral-co-vinyl alcohol-co-vinyl acetate) (MW = 70000-100000, Aldrich) (PVB) 5 wt% and ethyl cellulose (Aldrich) 5 wt%. The paste was screen printed onto both sides of a disc of YSZ electrolyte (300 μm thick, 25 mm diameter) and sintered at 1200 °C for 5 h to form layers with 70 vol% open porosity. L4ST solution was prepared by dissolving titanium(IV) propoxide (98%, Aldrich) and triethanolamine (Aldrich) (mole ratio 1:4) into an aqueous solution containing the appropriate amounts of lanthanum(III) nitrate hexahydrate (99.999%, Aldrich) and strontium nitrate (Adrich). LDC solution was prepared by dissolving lanthanum(III) nitrate hexahydrate and ammonium cerium(IV) nitrate

(99.99%, Aldrich) and glycine (Aldrich) in 0.4:0.6:2 molar ratio. The total metal ion concentration in these solutions was 0.5 mol L^{-1}. The impregnated solutions were decomposed at 400 °C following each impregnation step, and the final materials were calcined at 900 °C for 2 h.

L4ST was impregnated into the porous YSZ support for different numbers of times to form electrodes having different concentrations between 4 wt% and 40 wt% (Table 3.1) to determine the effect of concentration on activity. The amount of the impregnation was measured using the weight gain after final sintering divided by the total weight of the porous structure after impregnation. Another sample was impregnated twice (10 wt%) with LDC solution before L4ST in order to investigate the effect of co-impregnation on the performance of the cell. The cathode electrode was prepared by co-impregnation of GDC and $La_{0.6}Sr_{0.4}Co_{0.2}Fe_{0.8}O_3$ (LSCF) into the porous YSZ on the opposite side of the electrolyte. GDC aqueous solution (0.5 mol L^{-1}) was prepared by dissolving gadolinium(III) nitrate hexahydrate (99.9%, Aldrich), ammonium cerium(IV) nitrate and glycine in distilled water with 0.2:0.8:2 molar ratio. LSCF aqueous solution was also prepared in the same way by using appropriate amounts of lanthanum(III) nitrate hexahydrate, strontium nitrate, cobalt(II) nitrate hexahydrate (98+%, Aldrich) and iron(III) nitrate nonahydrate (Aldrich). The prepared GDC solution was impregnated twice (10 wt%), then decomposed at 400 °C following each impregnation, followed by calcination at 900 °C for 2 h. Then LSCF solution was impregnated four times (16 wt%) using the same decomposition and calcination sequence.

After the fuel cell MEAs were prepared by impregnating the anode catalyst solution into the porous layer at one side of the electrolyte and the cathode catalyst (GDC-LSCF) into the

layer at the other side of the cell, gold paste was applied onto both electrode surfaces to form the current collectors. The cells were affixed onto the alumina tube forming the outside wall of the anode compartment and sealed with a glass sealant (Armco-seal 617), and placed into the furnace to cure the sealant in situ. Dry H_2 with a flow rate of 50 mL min^{-1} flowed through the anode compartment while the cathode electrode was open to the air. The operating temperature varied between 800 °C and 900 °C.

Symmetrical cells were prepared by impregnating the same electrode materials into porous layers on both sides of the electrolyte. The cells were fixed onto a ceramic fixture and inserted into a quartz tube which was placed into the furnace. Humidified H_2 with 3 wt% H_2O was utilized as the feed at different temperatures between 700 °C and 900 °C.

Electrochemical measurements were performed using a Solartron SI 1287 electrochemical interface equipped with SI 1260 impedance/ gain-phase analyzer. All the EIS results were fitted based on the circuits available in appendix A.

A XRD system with a Co tube and a graphite monochromator was used to determine the phase of the synthesized powders. Microstructures of the samples were determined using field emission scanning electron microscopy (FE-SEM) (JOEL 6301F). Conventional and high resolution TEM analyses were performed using a JEOL-JEM 2100 microscope, operating at 200 kV accelerating voltage. A drop of diluted suspension of powder in ethanol was placed onto a carbon-coated grid and allowed to dry at room temperature before TEM analysis. Simulation of the experimental electron diffraction patterns was performed using Desktop Microscopist™ and

CrystalMaker software. The crystallographic data in references [30-32] were used to generate the simulations of different phases (Table 3.2).

3.3 Results and Discussion

3.3.1 XRD analysis

Figure 3.1 shows the XRD patterns for different materials prepared by impregnation into the porous YSZ structure. Figure 3.1(a) shows the XRD pattern of the porous YSZ structure sintered at 1200 °C. This structure had the cubic structure with symmetry **Fm-3m** and cell parameter 5.139 Å, corresponding to 8 mole% Y_2O_3 in ZrO_2. L4ST with the cubic perovskite structure of $SrTiO_3$ was formed after impregnation and calcination at 900 °C (Figure 3.1(b)). The cell parameter was calculated to be 3.904 Å, compared to the 3.905 Å for the parent $SrTiO_3$ structure. Figure 3.1(c) shows the XRD pattern of LDC impregnated into the porous YSZ with a cubic fluorite structure and cell parameter 5.526 Å. Figure 3.1(d) shows the XRD pattern for porous YSZ impregnated with both LDC and LST and calcined at 900 °C. The positions of all peaks did not change and no extra phases were formed, showing that the components of YSZ, LDC and LST did not react and so were chemically compatible up to 900 °C.

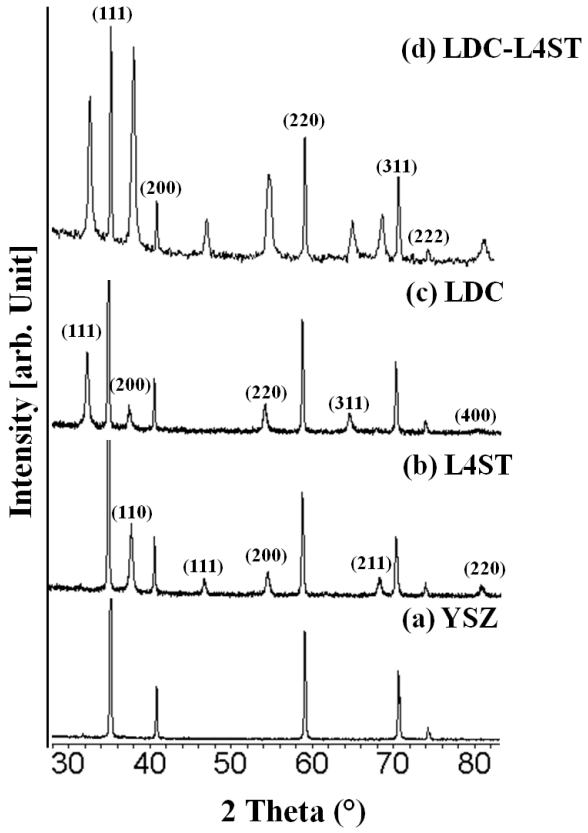

Figure 3. 1 XRD patterns of (a) YSZ structure sintered at 1200 °C for 5 h, and porous YSZ impregnated with different materials: (b) LDC, (c) L4ST, (d) LDC-L4ST calcined at 900 °C for 2 h.

3.3.2 GDC-LSCF impregnation

Liquid penetration of the impregnation solution into the porous structure is one of the important issues in the electrode preparation. In order to obtain a high performance electrode, impregnated deposits should evenly cover the whole structure, avoiding pores blockage. Figure 3.2 shows the microstructure of the impregnated cathode using GDC-LSCF materials. The GDC-LSCF particles fully covered the electrode-electrolyte interface of porous YSZ which

shows the effective penetration of impregnation liquid. Deposits with a particle size in the range of 20 nm to 50 nm covered the surfaces of the pores. In addition, a very tight interface contact formed between the porous electrode layer and dense electrolyte. Figure 3.3 (a) compares the EIS curves of a symmetrical cell with GDC-LSCF cathode catalysts in air at different temperatures. Area specific ohmic resistance (ASR_{ohmic}) of the cells improved from 0.43 $\Omega.cm^2$ to 0.25 $\Omega.cm^2$ when temperature was ramped between 700 °C and 900 °C. Area specific polarization resistance (ASR_{pol}) varied in the range of 0.6 $\Omega.cm^2$ to 0.23 $\Omega.cm^2$. Figure 3.3(b) shows the Arrhenius plot for the ASR_{ohmic} and ASR_{pol} of the cell in the same temperature range. Activation energies of 4.37 KJ and 7.79 KJ were calculated for the ohmic resistance and activation polarization of the cell.

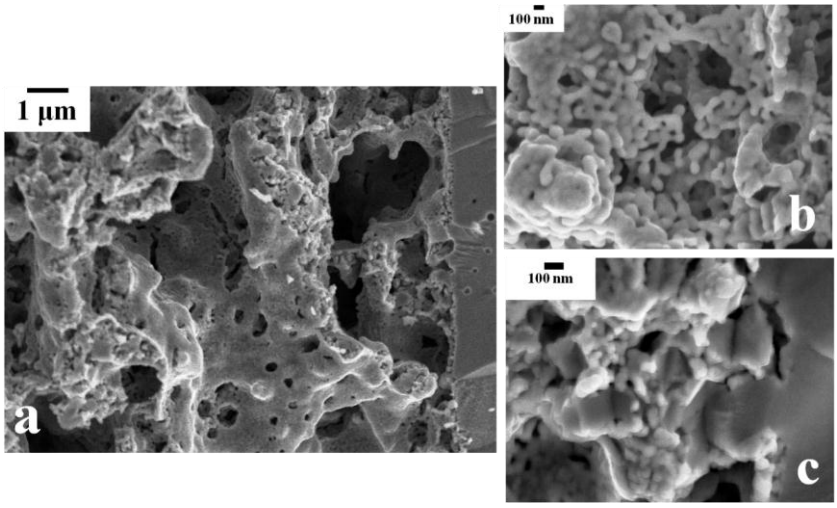

Figure 3. 2 SEM micrographs of GDC-LSCF impregnated cathode materials into porous YSZ calcined at 900 °C for 2 h.

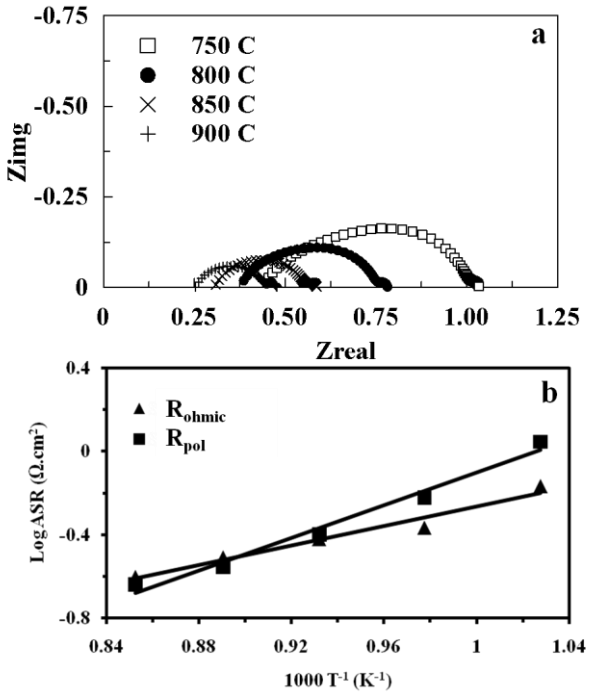

Figure 3. 3 (a) EIS, (b) Arrhenius plots for ASR_{ohmic} and ASR_{pol} for the GDC-LSCF impregnated cell in the temperature range between 700°C and 900 °C.

3.3.3 L4ST impregnation

Figure 3.4 shows the SEM micrograph of the porous YSZ impregnated with L4ST and calcined at 900 °C for 2 h. The fracture surface shows distinct LST particles and the YSZ surface. Their respective EDX patterns are shown in Figures 3.4(c) and 3.4(d), showing elemental analysis of the fracture area of the impregnated structure. The results show only the main elemental peaks related to the L4ST and YSZ. No other peaks were observed, indicating that there were no significant amounts of any impurity.

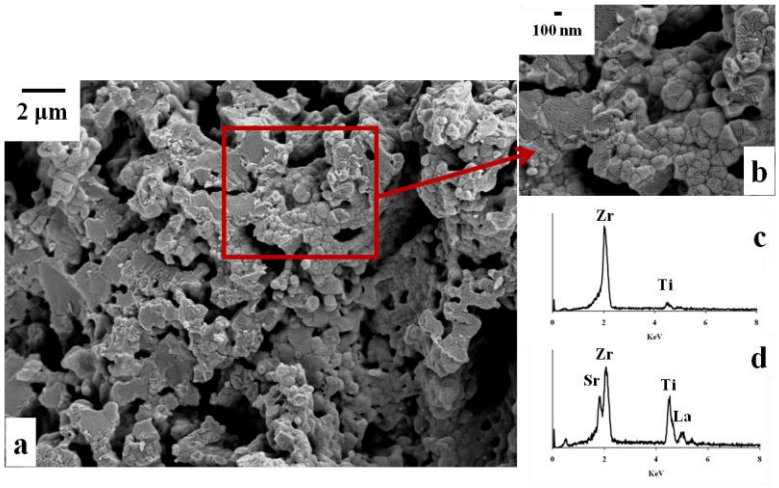

Figure 3. 4 SEM micrographs (a, b) and EDX of the fracture area for (c) YSZ and (d) impregnated L4ST (16 wt%).

Different amounts of L4ST were impregnated into porous YSZ to determine the optimum anode composition. Figure 3.5 compares the I-V curves for cells with different amounts of L4ST impregnation with H_2 fueling the cell at 850 °C. Table 3.1 compares peak power densities and the power densities at 0.7 V. The power density increased as the amount of L4ST deposit increased to a maximum value of 41 mW cm^{-2} and 39 mW cm^{-2} for 8 wt% and 16 wt% L4ST, respectively. The peak power density of the cell then decreased significantly when there was greater impregnation of L4ST into the porous YSZ, and power densities of 22 mW cm^{-2} and 3.2 mW cm^{-2} were obtained for 28 wt% and 40 wt% impregnation.

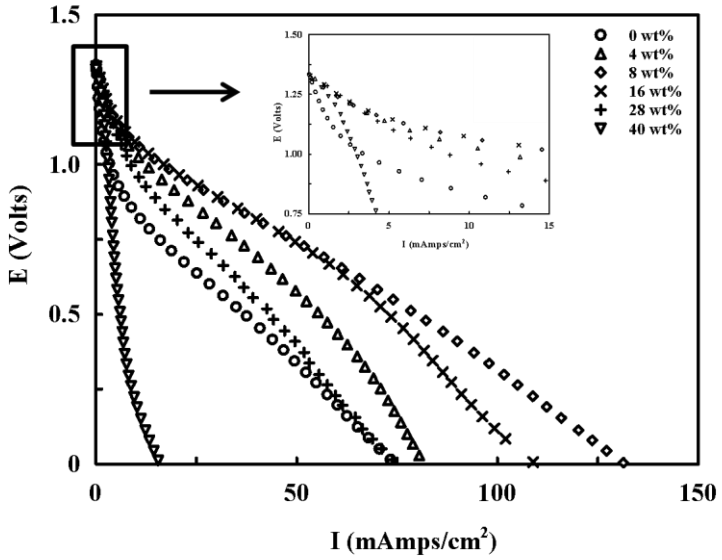

Figure 3. 5 I-V curves for the cells with different amounts of L4ST impregnation when H_2 was fed to the cells at 850 °C.

Table 3. 1 Electrochemical performance and characterization of the cells with different amounts of impregnated L4ST.

Impregnation times	L4ST wt%	Peak power density ($mW.cm^{-2}$)	Power density 0.7 V ($mW.cm^{-2}$)	ASR_{total} ($ohm.cm^2$)	ASR_{ohm} (EIS) ($ohm.cm^2$)	ASR_{pol} (EIS) ($ohm.cm^2$)
0	0	19	15	227.2	2.2	225
1	4	29	28	2.7	1	1.7
2	8	41	39	2.3	1	1.3
4	16	39	38	2.3	0.9	1.4
7	28	22	20	2.6	0.8	1.8
10	40	3.2	3	2.6	0.7	1.9

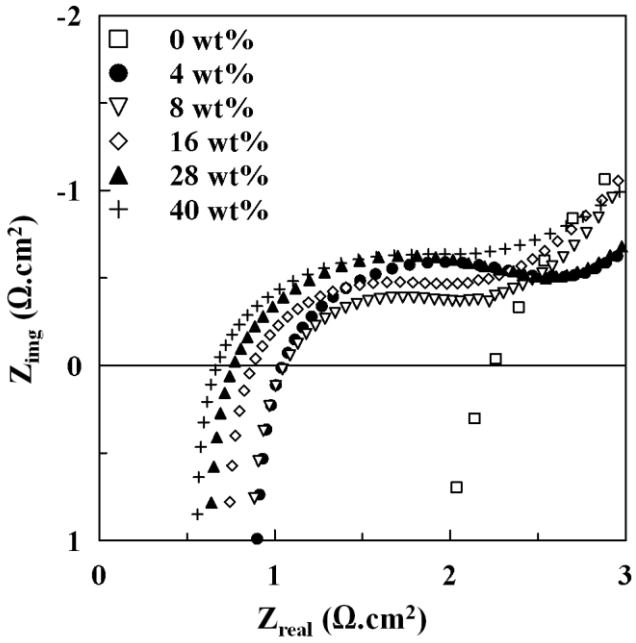

Figure 3. 6 EIS for the cells with different amounts of L4ST impregnation weight when H_2 was fed to the cells at 850 °C.

EIS showed that the ASR_{ohmic} of the cell (the intersection of the curve with the X-axis in Figure 3.6 decreased with increasing L4ST impregnation, between 2.2 Ω cm^2 and 0.7 Ω cm^2 as impregnation increased from 0 wt.% to 40 wt.% L4ST in the porous YSZ structure. The ASR_{pol} were obtained by fitting the EIS semicircules between 15 kHz to 100 Hz. The lowest polarization resistance, 1.3 Ω cm^2, was obtained for YSZ impregnated with 8 wt% L4ST. The polarization resistance increased with further impregnation of L4ST into the porous YSZ, up to 1.9 Ω cm^2 for

40 wt% L4ST. The cells with 8 wt% and 16 wt% L4ST showed the lowest ASR_{total} (ASR_{pol}+ASR_{ohmic}), 2.3 Ω cm^2.

The microstructures of the cells with different amounts of L4ST were characterized using SEM analysis (Figure 3.7). Figure 3.7(a) shows the micrograph of the porous YSZ before impregnation. The distribution of the formed L4ST particles over the surfaces of the YSZ particles after one impregnation is shown in Figure 3.7(b). Increasing the impregnation time increased the coverage of the porous YSZ surface with deposited particles (Figures 3.7(a-f)). Figure 3.7(c) shows that L4ST formed a dense layer on the surfaces of the YSZ after two impregnations to form 8 wt% deposits. Further impregnation increased the coverage of the particles. The ionic conductivity of L4ST by itself was not sufficient for conducting oxygen ions necessary for electro-oxidation of the fuel. Consequently, impregnation of L4ST over 16% increased the coverage of YSZ particles, limited the accessibility of the fuel to the TPBs for electrochemical oxidation of the fuel and reduced ionic conductivity.

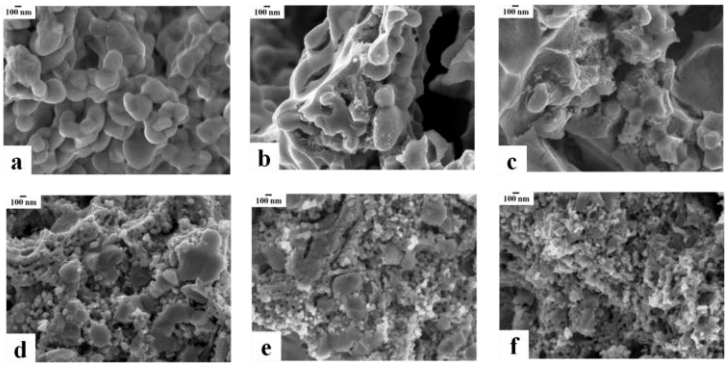

Figure 3. 7 SEM micrographs for the porous YSZ structure impregnated with L4ST: (a) 0 wt%, (b) 4 wt%, (c) 8 wt%, (d) 16 wt%, (e) 28 wt%, (f) 40 wt%, and calcined at 900 °C for 2 h.

Consequently, cells with 16 wt% of L4ST were chosen for use as MEAs to investigate the effect of LDC addition on the performance of the cell.

3.3.2 Co-deposition of L4ST and LDC

3.3.2.1 Performance

To improve the oxygen ionic conductivity and catalytic activity of the anode, we investigated the effect of addition of LDC to L4ST on the performance of the cell.

Figure 3.8 compares the power density and I-V curves for the cells with L4ST, LDC and combined LDC-L4ST impregnated anodes. The maximum power density of the cell at 900 °C was improved significantly by co-depositing LDC and L4ST, from 48 mW cm^{-2} to 161 mW cm^{-2} for L4ST and LDC-L4ST, respectively (Figure 3.8(b)).

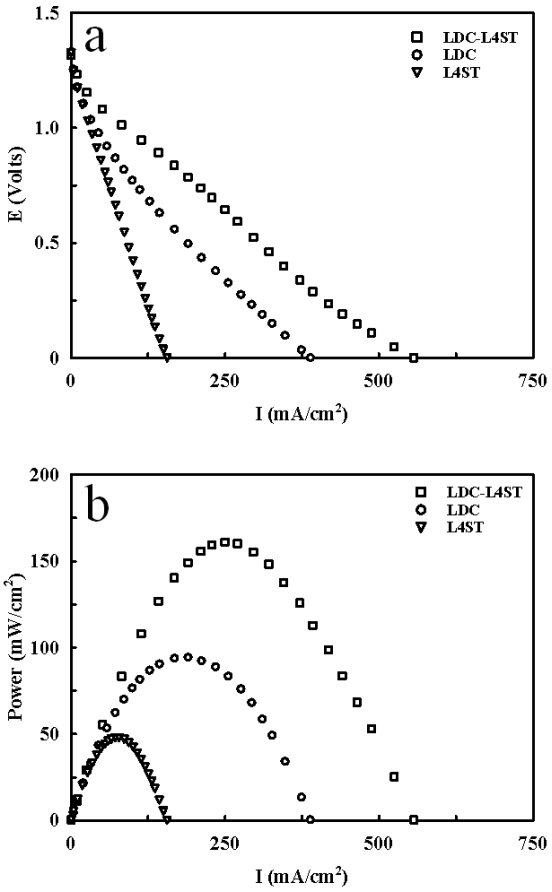

Figure 3. 8 Potential (a) and power density (b) curves vs. current density for different anode materials impregnated into porous YSZ structure using H_2 as fuel, at 900 °C.

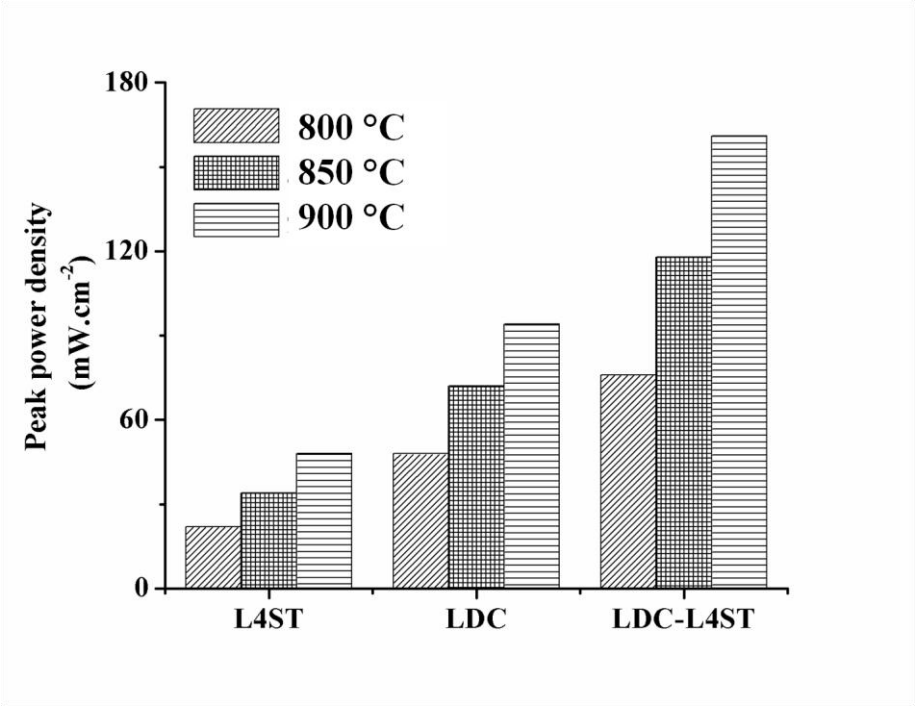

Figure 3. 9 Peak power densities of the cells with different impregnated materials at different operating temperatures when H_2 was fed to the anode.

Proportionately similar maximum power density improvement was found for operating temperatures throughout the range 800-900 °C (Figure 3.9). While the specific role of LDC is not yet clear for affecting such an improvement in performance of the cell, higher oxygen ionic conductivity, electrocatalytic activity and higher surface area for reactions when compared to L4ST are plausible contributing factors for cell performance enhancement in SOFC with H_2 feed.

3.3.2.2 Symmetrical cell

Figure 3.10 shows the EIS for the symmetrical cells with the different impregnated anodes in humidified H_2 (3% H_2O) at 900 °C. The same measurements were conducted at the

operating temperatures between 700 °C and 900 °C. Based on these curves, the values of ASR_{ohmic} and ASR_{pol} were determined and were summarized in Figure 3.11. The ohmic resistances of the cells in humidified H_2 are shown in Figure 3.11(a). The lowest ASR_{ohmic} were for the cells impregnated with L4ST or LDC-L4ST. For example, when the cells were operated at 800 °C, ASR_{ohmic} for the cells impregnated with L4ST or LDC-L4ST was 0.2 Ω cm^2 and the LDC impregnated cell had ASR_{ohmic} of 0.5 Ω cm^2 which was lower than the ASR_{ohmic} of porous YSZ alone. L4ST is an n-type electronic conductor under reducing conditions. Impregnating YSZ with this material improved the total conductivity of the electrodes by providing electron conducting paths throughout the porous structure.

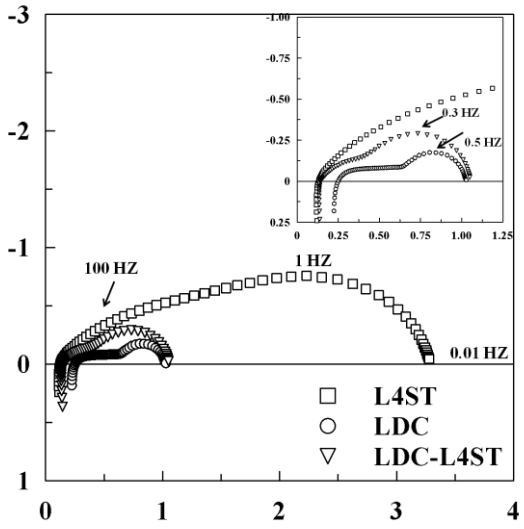

Figure 3. 10 EIS of the symmetrical cells prepared by impregnation of different materials into porous YSZ when humidified H_2 (3% H_2O) was fed to the cells at 900 °C.

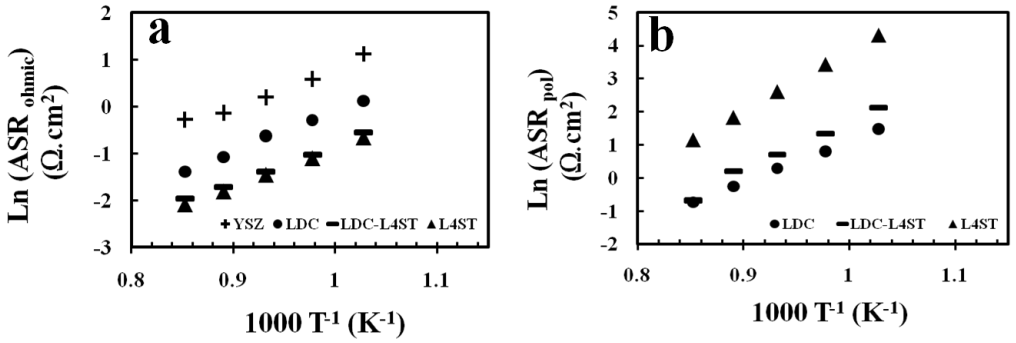

Figure 3. 11 Arrhenius plots of EIS data for the symmetrical cells having anodes prepared with different materials impregnated into porous YSZ. (a) ohmic resistance, (b) polarization resistance, in humidified H_2.

The values of ASR_{pol} of the cells were measured for different symmetrical cells with EIS in the frequency range 105 Hz to 0.01 Hz. The results showed that the presence of LDC along with L4ST significantly decreased the ASR_{pol} of the cell in humidified H_2 (Figure 3.11(b)). The polarization resistance decreased from 13.5 Ω cm^2 for L4ST to 2 Ω cm^2 for LDC-L4ST impregnated cells in humidified H_2 at 800 °C. The lowest ASR_{pol} was obtained for the cell with only LDC impregnated (0.77 Ω cm^2). LDC is a mixed electronic and ionic conductor, with lower electronic conductivity than L4ST. Consequently, ASR_{ohmic} was higher for the LDC impregnated cell, 0.25 Ω cm^2. The addition of LDC significantly improved the performance of the cell (Fig. 3.8). Thus the improvement in ionic conductivity of the anode may explain the performance improvement when LDC was co-impregnated into the porous YSZ anode. The results strongly indicated that the electronic conductivity of the cell in reducing atmosphere was enhanced by the presence of L4ST.The lower polarization resistance for LDC-containing samples showed that co-

impregnation of LDC also improved the electrocatalytic activity of the cell for electrochemical oxidation of H_2.

3.3.3 Microstructures of materials

The microstructures of the cell materials were investigated using SEM (Figure 12). Figure 12(a) shows the microstructure of L4ST deposits in the porous YSZ structure after four times impregnation. L4ST deposits covered the whole interior surface of the YSZ with particles. Micrographs of the LDC impregnated sample (Figure 12(b)) show the presence of nanometric particles distributed over the YSZ structure. The microstructure of the cell prepared by impregnation of LDC-L4ST (Figure 12(c)) revealed the effective role of LDC particles on distribution of L4ST deposits within the porous YSZ structure. The presence of particles with higher surface area and lower particle sizes drastically changed the distribution of L4ST particles and avoided formation of a dense layer on the YSZ structure. In addition, Figures 12(d) and 12(e) show that the particle sizes of the L4ST deposits all were reduced when in the presence of LDC particles, when compared to L4ST deposits alone on YSZ particles. The surface analyses showed that the specific surface area of the structure was improved by impregnation of LDC into the porous structure of YSZ. The specific surface area of the porous YSZ was 2.02 $m^2.g^{-1}$. Addition of L4ST increased the specific surface area of the structure to 2.41 $m^2\ g^{-1}$ which was further increased to 3.67 $m^2\ g^{-1}$ when LDC was impregnated prior to L4ST.

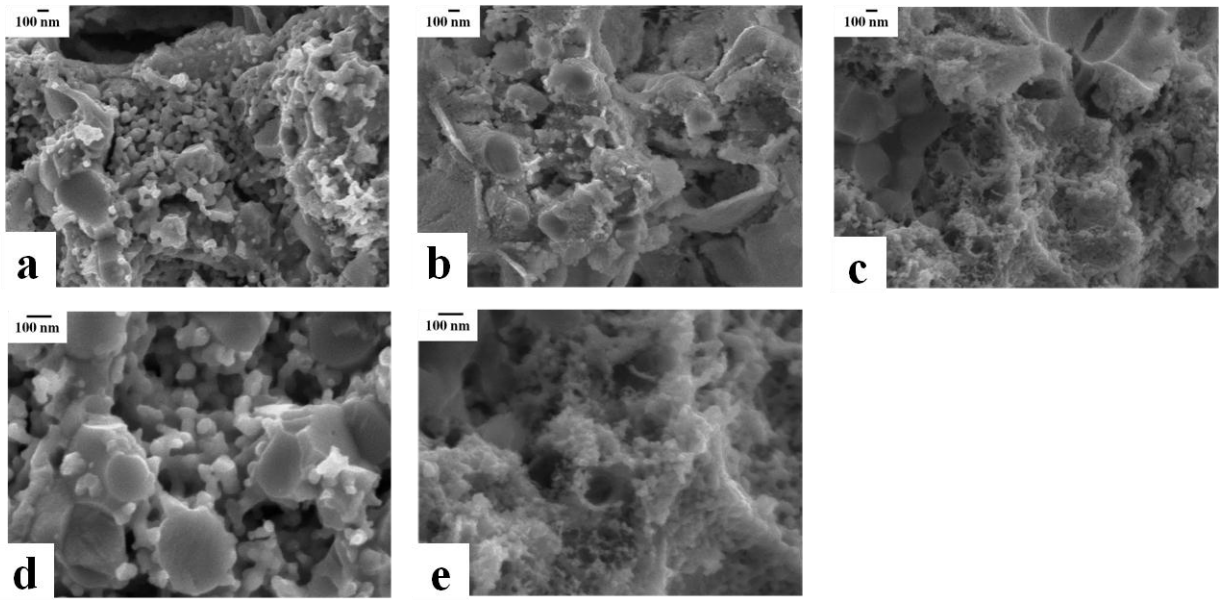

Figure 3. 12 SEM micrographs of the porous YSZ structure impregnated with: (a, d) L4ST, (b) LDC, (c, e) LDC-L4ST, calcined at 900 °C for 2 h.

TEM analyses were performed on samples having L4ST, LDC and LDC-L4ST impregnated into the YSZ particles, to characterize and compare both particle sizes and the morphologies of particles. Figure 13 shows TEM results of the L4ST-YSZ powder particles. Figure 13(a) shows the microstructure of the powder. The microstructure consisted of a relatively thick matrix and a number of small particles on the surface. The selected area diffraction (SAD) pattern from an area within the bulk of the particle is shown in Figure 13(b). Simulation of the SAD pattern indicated that this part of the sample most likely was cubic ZrO_2 powder. The diffraction pattern rings were not continuous and uniform, and instead appear in the form of arcs. Such arcing usually is observed in textured polycrystalline materials, stemming from the intersections of the diffracting planes and Eswald sphere [123,124]. Figure 13(c) shows the dark

field (DF) micrograph taken using a portion of the 111 plane of the cubic phase. The SAD pattern from the region near the surface of the particle is shown in Figure 13(d). The SAD pattern shows a spot pattern which is ascribed to the L4ST crystals. The simulation of the pattern indicated that the grain shown in the DF micrograph (Figure 13(e)) was close to the [011] zone axis of $SrTiO_3$. The high resolution TEM (HR-TEM) micrograph of the region near this grain showed lattice fringes from the L4ST grain (Figure 13(f)). The inset in this micrograph shows the digital diffractogram which contains a diffuse halo arising from an amorphous region. The observed contrast in the HR-TEM micrograph in Figure 13(f) is similar to the observed contrast described by Irvine et al. [60,125]; however, the data are insufficient to unambiguously ascribe them to the presence of secondary phase or a change of the atomic textures.

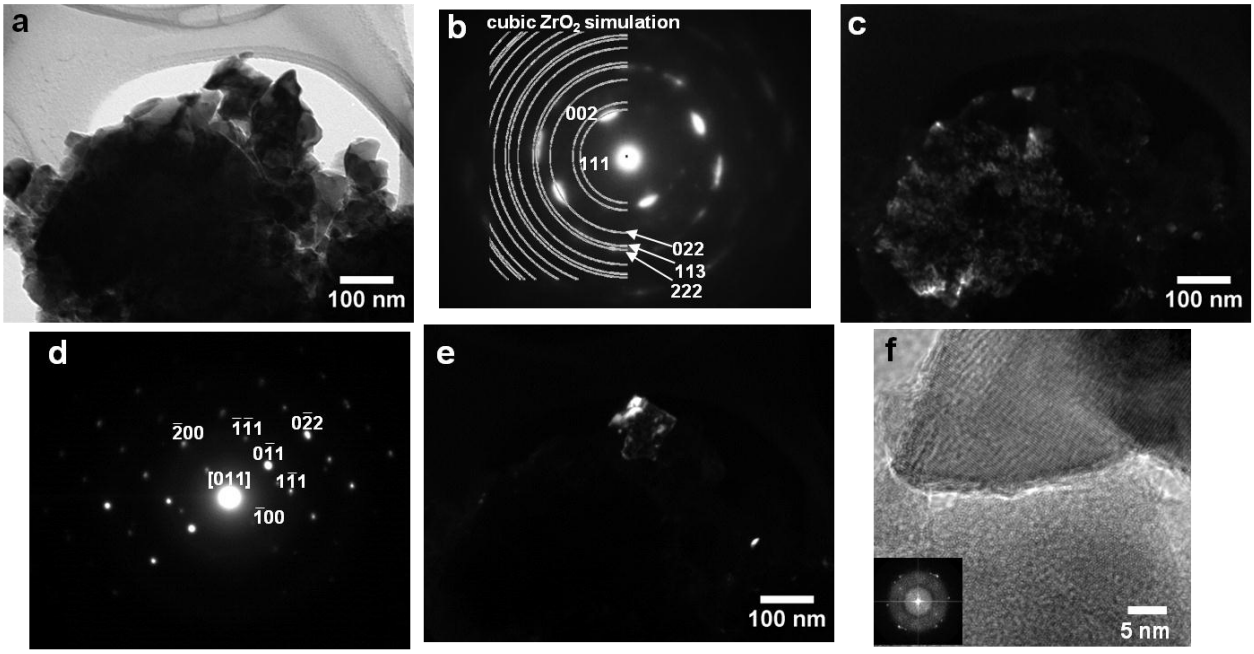

Figure 3. 13 TEM micrographs of L4ST impregnated sample: (a) bright field micrograph of a particle; (b) the SAD pattern from a region within the bulk of the particle far from the surface, and the simulated pattern for zirconia; (c) dark field micrograph obtained using the g = 111_{ZrO2} reflection; (d) the SAD pattern from the region near the surface marked by an arrow and the indexed zone axis corresponding to the $SrTiO_3$ phase; (e) dark field micrograph taken from the g = $0\text{-}11_{SrTiO3}$ reflection; (f) the HRTEM micrograph from the area near the surface.

The microstructure of 8YSZ-LDC powder is shown in Figure 14. The bright field (BF) micrograph in Figure 14(a), shows that the microstructure consists of a phase with quite small crystallites on a thick matrix. The SAD pattern of the area in Figure 14(a) also indicates the presence of two phases with different grain sizes (Figure 14(b)). The simulation of the ring pattern confirmed that the rings correspond to the ceria-based phase. The observed ring pattern also indicates that the CeO_2 phase was nanocrystalline with a particle size around 20 nm. The bright spots in the SAD pattern most likely correspond to the cubic YSZ matrix. This conclusion

is further supported by the DF micrograph in Figure 14(c). This micrograph was taken from the spot indicated as the 004 reflection of the ZrO_2 in the SAD pattern. Figure 14(d) shows the DF micrograph obtained using the portion of 111 and 002 rings of the CeO_2 phase. As this image indicates, the LDC crystallites had uniform dispersion over the surface of the YSZ particle.

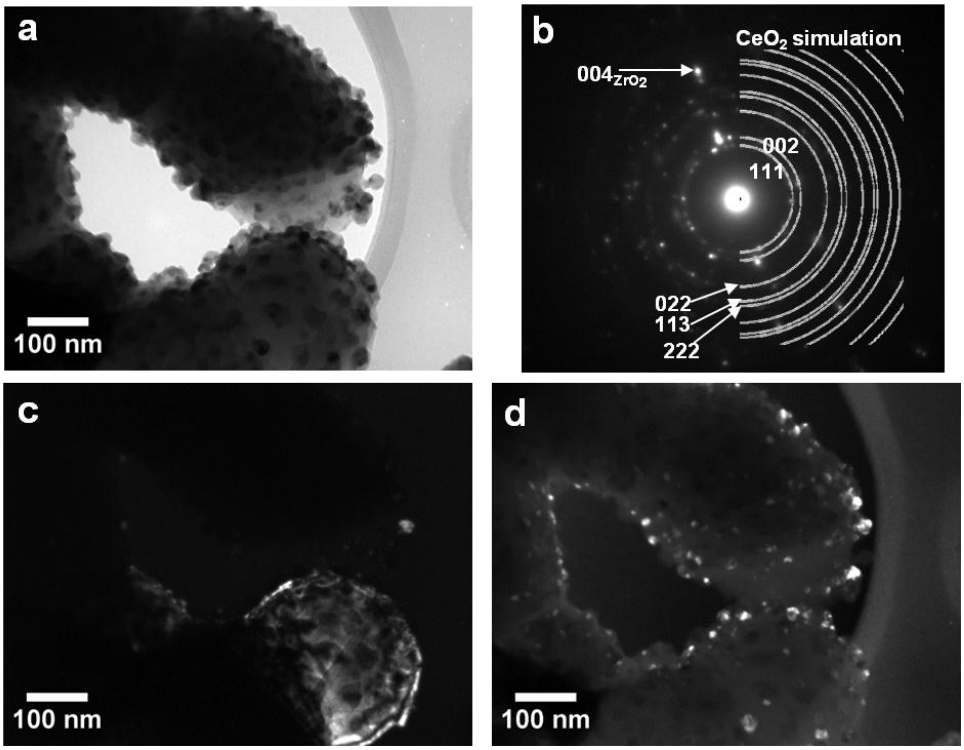

Figure 3. 14 TEM micrographs of LDC impregnated samples: (a) bright field micrograph of a particle; (b) corresponding SAD pattern with the simulated ring pattern for the CeO_2 phase; (c) dark field micrograph obtained using the g = 002ZrO_2 reflection; (d) dark field micrograph obtained using the portion of 111 and 002_{CeO2} rings.

Figure 3.15 shows the TEM analysis on the 8YSZ-LDC-L4ST powders. Figure 3.15(a) shows the BF micrograph of a few relatively large particles. The simulations of the ring patterns for both L4ST and LDC phases are shown in Figure 3.15(b). It can be seen that presence of both

phases would cause ring overlapping in the diffraction pattern. The corresponding SAD pattern is shown in Figure 3.15(c). Similar to the case of YSZ-LDC, the SAD pattern contains both bright spots and rings. The bright spots are ascribed to the YSZ matrix. The DF micrograph taken from a portion of the rings corresponding to 111 and 002 rings of LDC and 011 ring of LST is shown in Figure 3.15(d). As this image indicates, the L4ST and LDC nanocrystallites were densely dispersed across the surface of the YSZ particles.

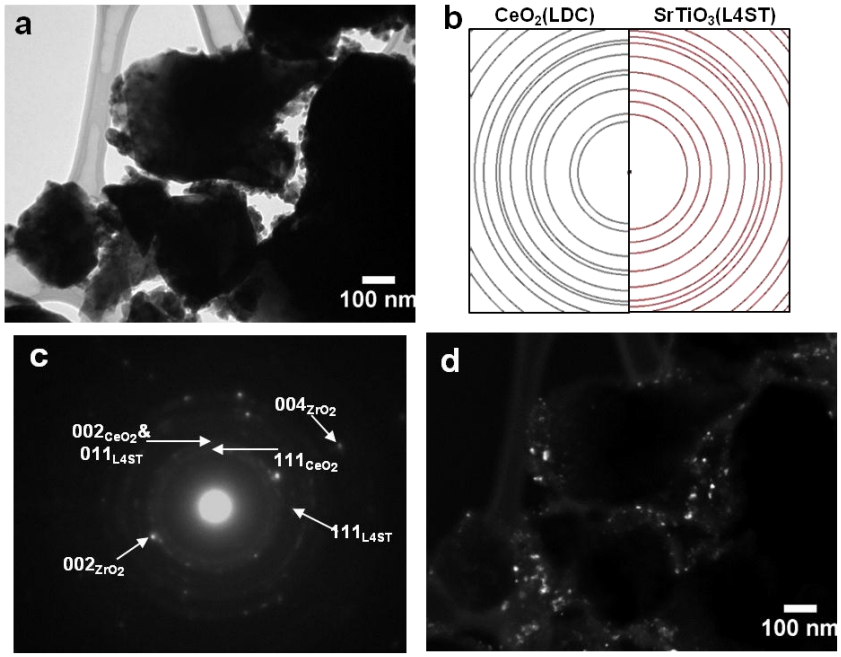

Figure 3. 15 TEM micrographs of LDC-L4ST impregnated samples: (a) bright field micrograph of a few particles; (b) the simulated ring patterns of CeO2 and SrTiO3 phases, highlighting the overlapping of rings; (c) corresponding SAD pattern; (d) dark field micrograph o obtained using the weak portion of the 002_{CeO2} , 111_{CeO2} and 011_{SrTiO3} rings.

TEM of the YSZ powders with different coatings of L4ST and LDC revealed important aspects of the microstructure. Different types of morphologies were achieved by applying various combinations of L4ST and/or LDC layers. Upon applying L4ST onto YSZ powders, the

resulting microstructure consisted of a YSZ matrix having relatively large L4ST particles on the surface. The TEM observations on 8YSZ-LDC powders revealed a nanoscale distribution of the LDC phase on the surface of the YSZ. The distribution of the LST phase was significantly enhanced when applying the L4ST layer on top of the prior deposited LDC phase.

3.3.4 Discussion

Co-impregnation of LDC with L4ST significantly improved the performance of the cell. The higher ionic conductivity of LDC when compared to YSZ and L4ST could be one of the contributing factors, by providing more oxygen to the reaction sites. The symmetrical cell results showed that the ohmic resistance of the cell did not change when LDC was incorporated into the structure, either in air or in H_2. While the fine particles of LDC were finely distributed within the structure, their low particle loading (10 wt.%) was not enough to provide a contiguous conduction path throughout the electrode. The EIS results for the symmetrical cells showed that the polarization resistance of the cell was reduced significantly through the presence of LDC in the structure. Co-impregnation of LDC and L4ST reduced the polarization resistance to one-third when compared to the L4ST impregnated sample. In fact, the higher catalytic activity of LDC could be another reason for the electrochemical activity improvement of the anode material. The TEM results also showed that the particle sizes of L4ST were reduced in the presence of LDC nano-particles. Sintering of YSZ at high temperature resulted in a structure with lower surface area. Impregnation of L4ST into this structure formed a dense and contiguous layer on the YSZ particles. The presence of LDC nano-particles on the surface of the YSZ increased the surface

area of the structure which was available for deposit of L4ST particles. Consequently, the impregnation of L4ST on the nano-particles with higher available surface area increased the total surface area of the structure. In addition, the particle sizes of L4ST were reduced, providing fine particles with better distribution within the structure.

In summary, the presence of LDC in combination with L4ST within the YSZ matrix resulted in a synergetic effect, high electronic conductivity of L4ST coupled with high catalytic activity of LDC, which significantly improved the performance of the cell for electrochemical oxidation of H_2. As the ultimate objective of development of this anode was for use when fuelling the cell with hydrocarbons containing high concentrations of H_2S, the effects of H_2S and CH_4 on the catalytic activity of this anode material presently will be reported in Part II.

3.4 Conclusions

Anode materials having different amounts of LDC and L4ST as the active catalysts were formed by impregnation into a porous YSZ structure with approximate 70 vol% porosity. The performance of the cell improved three-fold when LDC was impregnated prior to L4ST, compared to the cell with anodes containing only L4ST. The EIS data from symmetrical cells showed that the polarization resistance of the cell was decreased significantly by the inclusion of LDC into the anode when using humidified H_2 feed. The presence of LDC into the structure of the anode enhanced the catalytic activity of the anode towards the electrochemical oxidation of the H_2. EIS results showed that the polarization resistance of the cell significantly dropped; however, its ohmic resistance remained unchanged showing that the ionic conductivity of the

structure was controlled by the YSZ structure and impregnation of LDC had minor effect. In addition, SEM and TEM analyses showed that prior impregnation with LDC resulted in better distribution of the L4ST into the YSZ structure.

3.5 References

[1] G.J.K. Acres, J. Power Sources 100 (2001) 60–66.

[2] K. Hassmann, Fuel Cells 1 (2001) 78–84.

[3] T. Setoguchi, K. Okamoto, K. Eguchi, H. Arai, J. Electrochem. Soc. 139 (1992) 2875–2880.

[4] M. Mori, T. Yamamoto, H. Itoh, H. Inaba, H. Tagawa, J. Electrochem. Soc. 145 (1998) 1374–1381.

[5] B.C.H. Steele, Solid State Ionics 86-88 (1996) 1223–1234.

[6] T. Kim, G. Liu, M. Boaro, S.-I. Lee, J.M. Vohs, R.J. Gorte, O.H. Al-Madhi, B.O. Dabbousi, J. Power Sources 155 (2006) 231–238.

[7] W. Zhu, C. Xia, J. Fan, R. Peng, G. Meng, J. Power Sources 160 (2006) 897–902.

[8] S. Tao, J.T.S. Irvine, Nat Mater 2 (2003) 320–323.

[9] U. Balachandran, N.G. Eror, J. Electrochem. Soc. 129 (1982) 1021–1026.

[10] B. Odekirk, U. Balachandran, N.G. Eror, J.S. Blakemore, J. Am. Ceram. Soc. 66 (1983) C–22–C–23.

[11] O.A. Marina, N.L. Canfield, J.W. Stevenson, Solid State Ionics 149 (2002) 21–28.

[12] R. Mukundan, E.L. Brosha, F.H. Garzon, Electrochem. Solid-State Lett. 7 (2004) A5–A7.

[13] O.. Marina, L.. Pederson, In: J. Huijsmans, Editor, Fifth European Solid Oxide Fuel Cell Forum, European Fuel Cell Forum, Oberrohfdorf, Switzerland (2002) 481–489.

[14] J.C. Ruiz-Morales, J. Canales-Vázquez, C. Savaniu, D. Marrero-López, W. Zhou, J.T.S. Irvine, Nature 439 (2006) 568–571.

[15] A. Vincent, J.-L. Luo, K.T. Chuang, A.R. Sanger, J. Power Sources 195 (2010) 769–774.

[16] R.J. Gorte, J.M. Vohs, Curr. Opin. Colloid Interface Sci. 14 (2009) 236–244.

[17] M.D. Gross, J.M. Vohs, R.J. Gorte, Electrochem. Solid-State Lett. 10 (2007) B65–B69.

[18] F. Bidrawn, G. Kim, N. Aramrueang, J.. Vohs, R.. Gorte, J. Power Sources 195 (2010) 720–728.

[19] J. Chen, F. Liang, D. Yan, J. Pu, B. Chi, S.P. Jiang, L. Jian, J. Power Sources 195 (2011) 5201–5205.

[20] X. Xu, F. Wang, Y. Liu, J. Pu, B. Chi, L. Jian, J. Power Sources 196 (2011) 9365–9368.

[21] Y. Wang, H. Zhang, F. Chen, C. Xia, J. Power Sources 203 (2012) 34–41.

[22] D. Ding, M. Gong, C. Xu, N. Baxter, Y. Li, J. Zondlo, J. Power Sources 196 (2011) 2551–2557.

[23] L. Nie, M. Liu, Y. Zhang, M. Liu, J. Power Sources 195 (2010) 4704–4708.

[24] X. Li, N. Xu, X. Zhao, K. Huang, J. Power Sources 199 (2012) 132–137.

[25] M.C. Tucker, G.Y. Lau, C.P. Jacobson, S.J. Visco, L.C. De Jonghe, J. Power Sources 195 (2010) 3119–3123.

[26] J.-T. Zhang, F.-L. Liang, B. Chi, J. Pu, J. Li, J. Power Sources 200 (2012) 29–33.

[27] J.S. Cronin, J.R. Wilson, S.A. Barnett, J. Power Sources 196 (2011) 2640–2643.

[28] P. Puengjinda, H. Muroyama, T. Matsui, K. Eguchi, J.Power Sources 204 (2012) 67–73.

[29] Y. Chen, J. Bunch, C. Jin, C. Yang, F. Chen, J. Power Sources 204 (2012) 40–45.

[30] Y. Huang, J.M. Vohs, R.J. Gorte, J. Electrochem. Soc. 152 (2005) A1347–A1353.

[31] Y. Huang, K. Ahn, J.M. Vohs, R.J. Gorte, J. Electrochem. Soc. 151 (2004) A1592–A1597.

[32] F. Bidrawn, G. Kim, N. Aramrueang, J.M. Vohs, R.J. Gorte, J. Power Sources 195 (2010) 720–728.

[33] S. Lee, M. Bevilacqua, P. Fornasiero, J.M. Vohs, R.J. Gorte, J. Power Sources 193 (2009) 747–753.

[34] S. Jung, C. Lu, H. He, K. Ahn, R.J. Gorte, J.M. Vohs, J. Power Sources 154 (2006) 42–50.

[35] G. Kim, S. Lee, J.Y. Shin, G. Corre, J.T.S. Irvine, J.M. Vohs, R.J. Gorte, Electrochem. Solid-State Lett. 12 (2009) B48–B52.

[36] S. Lee, G. Kim, J.M. Vohs, R.J. Gorte, J. Electrochem. Soc. 155 (2008) B1179–B1183.

[37] K. Ahn, S. Jung, J.M. Vohs, R.J. Gorte, Ceram. Int. 33 (2007) 1065–1070.

[38] M. Roushanafshar, J.-L. Luo, A.L. Vincent, K.T. Chuang, A.R. Sanger, Int. J. Hydrogen Energy 37 (2012) 7762-7770

[39] A.L. Vincent, J.-L. Luo, K.T. Chuang, A.R. Sanger, Applied Catalysis B: Environmental 106 (2011) 114-122.

[40] L. Tang, D.E. Laughlin, J. Appl. Crystallogr. 29 (1996) 411–418.

[41] D.. Williams, C.. Carter, Transmission Electron Microscopy: A Textbook for Materials Science, 2nd ed., Springer, 2009.

[42] J.C. Ruiz-Morales, J. Canales-Vázquez, C. Savaniu, D. Marrero-López, W. Zhou, J.T.S. Irvine, Nature 439 (2006) 568–571.

[43] J. Canales-Vázquez, M.J. Smith, J.T.S. Irvine, W. Zhou, Adv. Funct. Mater. 15 (2005) 1000–1008.

[44] B. Butz, P. Kruse, H. Störmer, D. Gerthsen, A. Müller, A. Weber, E. Ivers-Tiffée, Solid State Ionics 177 (2006) 3275–3284.

[45] C.J. Howard, H.T. Stokes, Acta Crystallogr A 61 (2004) 93–111.

[46] D.G. Lamas, R.O. Fuentes, I.O. Fábregas, M.E. Fernández de Rapp, G.E. Lascalea, J.R. Casanova, N.E. Walsöe de Reca, A.F. Craievich, J. Appl. Crystallogr. 38 (2005) 867–873.

Chapter 4

Electrochemical oxidation of H_2S-containing hydrogen and methane over LDC-LST impregnated SOFC anodes

4.1. Introduction

SOFCs provide higher energy conversion efficiency with environmentally friendly products when compared to conventional energy production systems based on combustion processes [126]. Replacing pure H_2 with other fuels such as natural gas can extend the applications of SOFCs and make them more economically viable [127]. However, choosing anode materials for such applications is a critical issue in terms of high electrocatalytic activity, coking resistance and hydrogen sulfide tolerance [43,49,69,93,95]. Nickel based anode materials showed high electrocatalytic activity for H_2 oxidation [93,128], but they cannot tolerate coking when different hydrocarbons fuel the cell [129,130]. Addition of either other metal catalysts or cerium oxide based materials improved the stability of the anode [129,131–135]; however, the presence of H_2S in the fuels is still a challenging issue [25,49,85,90,136,137].

Ni-YSZ has been studied in different concentrations of H_2S containing-feeds. It has been reported that a few ppm of H_2S can significantly poison the Ni-YSZ anode materials [49]. Replacing Ni with Cu-CeO_2 as anode material for SOFCs exhibited no dramatic performance drop up to 600 ppm H_2S in the H_2 [138]. Weak bonding energy of H_2S adsorption with Cu could

be the reason for its higher sulfur tolerance compared to Ni [139]. Ceramic based anode materials of LSCM showed high electrochemical activities toward H_2 and CH_4 oxidation, but instability in 10% H_2S-containing H_2 [44]. Addition of GDC improved the stability of the anode material in H_2S (0.5%)-CH_4, showing an initial degradation rate of 1.4%/h followed by a stable degradation rate of 0.017%/h at 850 °C, on which no carbon and sulfur deposition were detected [140]. In contrast, it was shown that high concentrations of H_2S improved the electrochemical oxidation of the feed using L4ST as the anode material when methane or syngas (CO: H_2 6: 4) fuelled the cell [122,121]. The same performance improvement was also observed using $La_{0.3}Sr_{0.7}VO_3$ anode material when H_2 switched to H_2S (5%)-H_2 [141]. Vincent et al. [122] reported that the electrochemical oxidation of H_2S (0.5%) containing- CH_4 is different depending on the applied potential.

Using high concentration H_2S-containing fuels is more economically profitable which decreases the purification cost of the fuels. In order to achieve this objective, replacing Ni based catalysts with other anode materials is necessary [81,85,142,143]. Strontium titanate based oxides with perovskite structure are viable anode materials for high concentration H_2S-containing fuels [49,90,144]. Lanthanum doped strontium titanate has been used by different researchers in different fuel systems containing different concentrations of H_2S [49,145–147]. The results showed that this material was chemically and electrochemically stable when exposed to high concentrations of H_2S. One of the main drawbacks of this anode material is the low activities toward the oxidation of fuels [43,48] compared to other anode materials including: cermets and LSCM [36]. Low oxygen ionic conductivity of the $SrTiO_3$ structure is one of the main reasons

which need to be improved by making composites with other ionic conductor materials or doping different elements on the Sr and Ti atomic sites to introduce oxygen vacancies [54,60,148–150]. Irvine et al. showed that doping of Ga and Mn on the Ti atomic sites disrupted the extending of oxygen defects into the structure which improving its ionic conductivity with the comparable result to LSCM [58]. Doping of Ba on the Sr atomic sites also improved the performance of the anode material [98]. Addition of YSZ [122] and cerium oxide based materials [121,146,147] is another way for improving the ionic conductivity of $SrTiO_3$ based materials as anodes of SOFCs.

In this paper, we analyzed the effect of high concentration H_2S (0.5%) on the electrochemical oxidation of H_2 and CH_4 using L4ST, LDC and LDC-L4ST as the anode materials for SOFCs. The effect of LDC addition on the electrochemical oxidation of hydrogen, conductivity, and microstructure of the impregnated anode structures was investigated in the previous chapter. As these anode materials were developed to be used in high concentration of H_2S-containing feeds, different electrochemical tests and mass spectrometry analysis were performed in order to get more insight about the possible mechanisms for electrochemical oxidation of methane in the presence of H_2S (0.5%). The interaction of H_2S with the anode materials is also investigated using the 4-point conductivity measurement technique to prove the possibility of the charge transfer between H_2S and the catalysts.

4.2. Experimental

Porous YSZ was prepared using a mixture of YSZ (Tosoh) and graphite 40 wt% powders. A paste was prepared by mixing the powders with α-terpineol (Alfa Aesar) and isopropanol (volume ratio 2:1) as a solution containing poly(vinyl butyral-co-vinyl alcohol-co-vinyl acetate) (MW = 70000-100000, Aldrich) (PVB) 5 wt% and ethyl cellulose (Aldrich) 5 wt%. The paste was screen printed onto both sides of a disc of YSZ electrolyte (300 μm thick, 25 mm diameter) and then sintered at 1200 °C for 5 h to form a layer with 70 vol% open porosity.

L4ST precursor solution was prepared by dissolving titanium(IV) propoxide (98%, Aldrich) and triethanolamine (Aldrich) (mole ratio 1:4) into an aqueous solution containing the appropriate amounts of lanthanum(III) nitrate hexahydrate (99.999%, Aldrich) and strontium nitrate (Adrich). LDC precursor solution was prepared by dissolving lanthanum(III) nitrate hexahydrate, ammonium cerium(IV) nitrate (99.99%, Aldrich) and glycine (Aldrich) in 0.4:0.6:2 molar ratio. The total metal ion concentrations in these solutions was 0.5 mol L^{-1}. The porous YSZ was impregnated with L4ST and LDC solutions. The impregnated solutions were decomposed at 400 °C following each impregnation step, and the final materials were calcined at 900 °C for 2 h. L4ST was impregnated four times to form electrodes having 16 wt% deposits. LDC-L4ST sample was prepared by impregnation of LDC twice (10 wt%) before L4ST (16 wt%).

The cathode electrode was prepared by co-impregnation of GDC and LSCF into the porous YSZ on the opposite side of the electrolyte. GDC precursor aqueous solution (0.5 mol L^{-1}) was prepared by dissolving gadolinium(III) nitrate hexahydrate (99.9%, Aldrich), ammonium cerium(IV) nitrate and glycine in distilled water with 0.2:0.8:2 molar ratio. LSCF precursor

solution also was prepared in the same way by using appropriate amounts of lanthanum(III) nitrate hexahydrate, strontium nitrate, cobalt(II) nitrate hexahydrate (98+%, Aldrich) and iron(III) nitrate nonahydrate (Aldrich). GDC preparation solution was impregnated twice (10 wt%), then decomposed at 400 °C following each impregnation, followed by calcination at 900 °C for 2 h. Then LSCF solution was impregnated four times (16 wt%) using the same decomposition and calcination sequence. Microstructure of the electrodes of SOFCs were captured using a field emission scanning electron microscope (FE-SEM) (JOEL 6301F).

Subsequently, MEAs were prepared by impregnating the anode catalyst solution into the porous layer at one side of the electrolyte and the cathode catalyst (GDC-LSCF) into the layer at the other side of the cell; gold paste was applied onto both electrode surfaces to form the current collectors. The cells were affixed onto an end of the alumina tube forming the outside wall of the anode compartment and sealed with a glass sealant (Armco-seal 617), and placed into the furnace to cure the sealant *in situ*. Dry H_2, CH_4, H_2S (0.5%)-H_2 and H_2S (0.5%)-CH_4 with a flow rate of 50 mL min^{-1} flowed through the anode compartment while the cathode electrode was open to the air. The operating temperature varied between 800 °C and 900 °C. Electrochemical analyses of cells were performed using a Solartron SI 1287 electrochemical interface equipped with SI 1260 impedance/ gain-phase analyzer. The exhaust of the anode tube was connected to a mass spectrometer (Pfeiffer Thermostar GSD 301) to analyze the gas composition effluent out of the cell.

Symmetrical cells were prepared by impregnating the same electrode materials into porous layers at both sides of the electrolyte. The cells were fixed onto a ceramic fixture and inserted into a

quartz tube which was placed into the furnace. The electrochemical impedance analysis of the cathode material symmetrical cell was measured in dry air from 700 °C to 900 °C. Humidified feed with 3 wt% H_2O was used as the feed for the anode material symmetrical cell EIS measurements at different temperatures between 800 °C and 900 °C.

Four-point conductivity measurement technique was used for measuring the conductivity of the impregnated porous YSZ structure. Porous YSZ bars (ℓ = 10 mm, d = 4.3 mm) were prepared by mixing YSZ and Graphite powders 40 wt.%, impregnated with different solutions to prepare LDC, L4ST and LDC-L4ST containing structures and sintered with the same heating program. Two probes were adjusted in the middle of the bar with a fixed distance (5.5 mm) to measure the potential difference along the bar. Two other probes were fixed onto the ends of the bar providing current into the bar. Gold paste and gold wires were used as the current collectors. The potential differences between potential probes were measured at different applied current using 0.2 mA, 0.4 mA, 1 mA as well as reverse polarity using -0.2 mA, -0.4 mA and -1 mA under galvanoastatic conditions. The resistance of the samples were measured in different atmospheres including: air, H_2 and H_2S (0.5%)-H_2 between 700 °C to 900 °C using the slope of the potential-current line. The specific electrical conductivities of the samples were calculated using Equation 1:

$$\sigma = \frac{L}{R.A} \qquad \text{(Equation 1)}$$

where, σ is the conductivity of the porous structure, L distance between the potential probes, A surface area of the bars and R is the measured resistance of the samples.

The electrochemical analyses of the fuel cells were performed using a 4-probes configuration (Figure 4.1). I-V curves were measured with two probes, WE and RF2, attached to the anode and the other two, RF1 and CE, attached to the cathode. The stability tests were performed under galvanostatic condition (40 $mA.cm^{-2}$) with two probes connected to the anode, one probe, CE, was attached to the cathode and another probe, RF1, connected to Pt wire which was attached to the rim of the YSZ electrolyte disk as shown in Figure 4.1.

Temperature program oxidation (TPO) method was used to analyse the carbon deposition on the anode materials. Two samples containing L4ST and LDC-L4ST anode materials were exposed to H_2S (0.5%)-CH_4 feed (50 $mL.min^{-1}$) under 0.7 V potentiostatic run for 20 h at 800 °C. The feed switched to N_2 under OCV condition and cooled down to room temperature with 5 $°C.min^{-1}$. Samples were put into a quartz tube connected to a mass spectrometer and oxidized using O_2 (10%)-He with the temperature ramping from room temperature to 1000 °C with 1 $°C.min^{-1}$ heating rate.

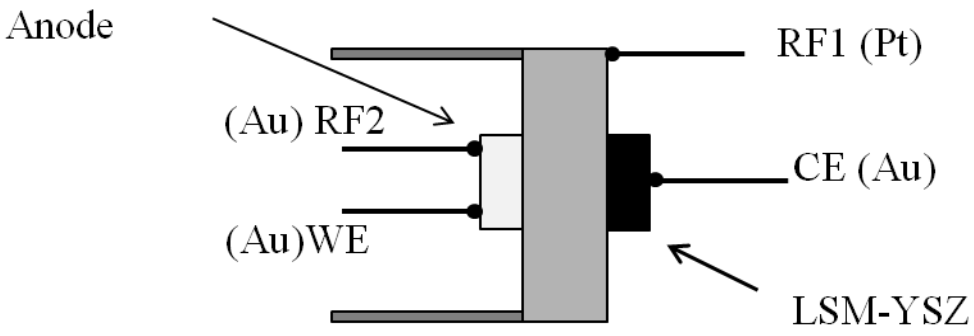

Figure 4. 1 Schematic of the 4- electrodes configuration cell.

4.3. Results and discussion

4.3.1. Symmetrical Cell

Figure 4.2 compares EIS results for the symmetrical cell with LDC-L4ST anode material in different fuels at 800 °C. ASR_{pol} of the anode decreased from 2.1 $\Omega.cm^2$ to 1.8 $\Omega.cm^2$ when H_2S (0.5%) was added into the H_2 feed. Further measurements showed increase of ASR_{pol} by time to 3.02 $\Omega.cm^2$ after 40 h of exposure. The reversibility of this deactivation was examined by switching to H_2. ASR_{pol} suddenly increased to 3.9 $\Omega.cm^2$ after purging H_2 followed by improvement to 2.4 $\Omega.cm^2$ after 24 h of exposure. The EIS results of the symmetrical cell when CH_4 and H_2S (0.5%)-CH_4 purged the cell showed that the ASR_{pol} of the cell suddenly dropped from 78.35 $\Omega.cm^2$ to 8.6 $\Omega.cm^2$ when gas switched from CH_4 to H_2S (0.5%)-CH_4 which increased to 34.8 after 24 h exposure time (Figure 4.3). ASR_{pol} of the cell did not change after switching to H_2 and remained constant during 24 h exposure. In contrast to H_2S (0.5%)-H_2, no recovery was observed when H_2S (0.5%)-CH_4 fed the cell because of carbon deposition on the surface of the catalyst which could not be easily removed under OCV conditions when the cell is not biased.

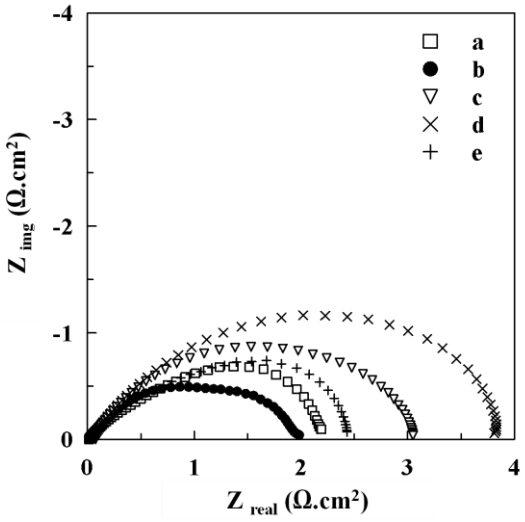

Figure 4. 2 EIS results for symmetrical cell when different gases fuelled the anode with the sequence of: (a) H_2, (b) H_2S (0.5%)-H_2, (c) H_2S (0.5%)-H_2 after 40 h, (d) H_2, (e) H_2 after 24 h at 800 °C.

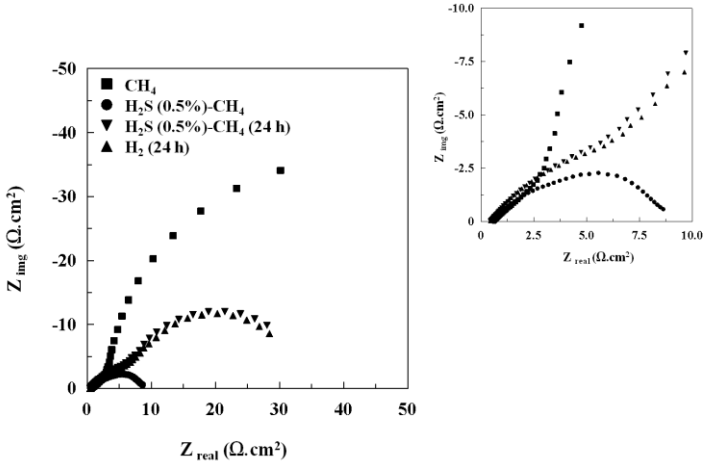

Figure 4. 3 EIS results for symmetrical cell when different gases fuelled the anode with the sequence of: (a) CH_4, (b) H_2S (0.5%)-CH_4, (c) H_2S (0.5%)-H_2 after 24 h, (d) H_2 after 24 h at 800 °C.

4.3.2. Performance

Figure 4.4 compares the power densities of the cell when H_2 and H_2S (0.5%)-H_2 fed the anode at 900 °C. The peak power densities of the cell improved from 161 mW.cm^{-2} to 256 mW.cm^{-2} when H_2S (0.5%) was added into the feed. Variations of peak power densities with H_2S concentrations at 800 °C are shown in Figure 4.5. Addition of H_2S (0.1%) improved the power density of the cell from 54 mW.cm^{-2} to 89 mW.cm^{-2}. Further addition of H_2S slightly improved the peak power density of the cell, and the maximum value of 110 mW.cm^{-2} was obtained for 0.5% H_2S.

Figure 4.6 illustrates the effect of H_2S addition on the power density of the cell when CH_4 fuelled the cell at 900 °C. The peak power densities of 27 mW.cm^{-2} and 158 mW.cm^{-2} were obtained when CH_4 and H_2S (0.5%)-CH_4, respectively, fuelled the cell.

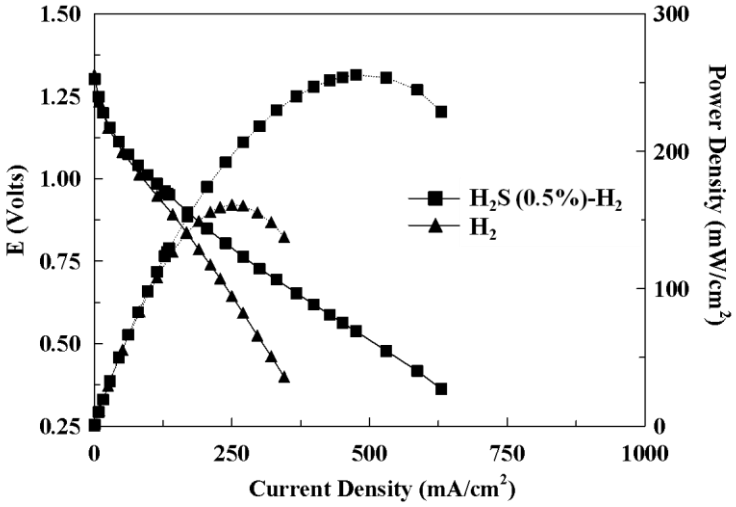

Figure 4. 4 Power density vs. current density curves when H_2 and H_2S (0.5%)-H_2 fuelled the cell at 900 °C.

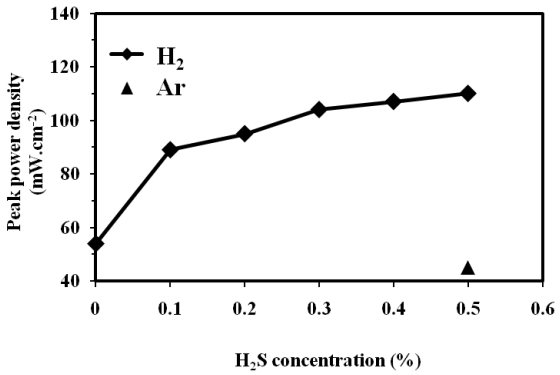

Figure 4. 5 Peak power density variations with H_2S concentrations when H_2 or Ar fed the anode compartment of the cell at 800 °C.

Table 4.1 compares the peak power densities of the cells with different anode materials when different feeds fuelled the cells. The co-impregnation of LDC with L4ST improved the electrochemical oxidation of different fuels compared to only impregnation of L4ST. For example, the peak power density of the cell containing LDC-L4ST was almost two fold higher than that with L4ST anode when they were fed by H_2S-containing CH_4 at 800 ^oC.

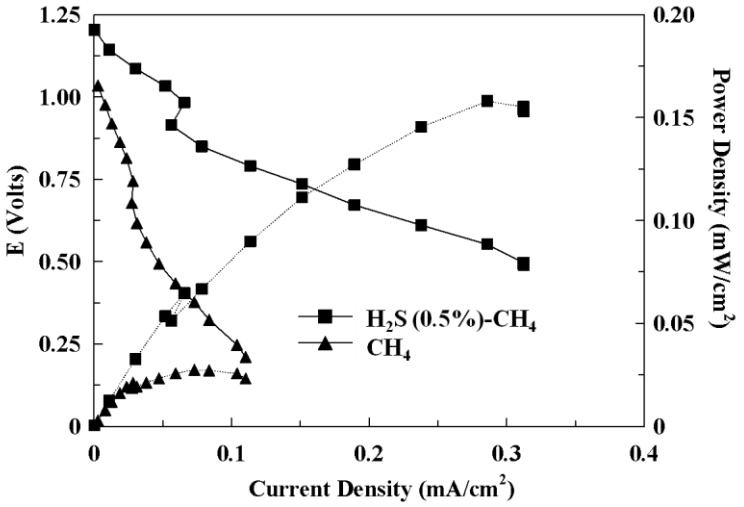

Figure 4. 6 Power density vs. current density curves when CH_4 and H_2S (0.5%)-CH_4 fuelled the anode at 900 °C.

Table 4. 1 Peak power densities (mW.cm^{-2}) for different anode materials when different feeds fuel the cell at 800 °C.

	H_2	H_2S (0.5%)-H_2	CH_4	H_2S (0.5%)-CH_4
L4ST	20	36	3	30
LDC	50	25	6	30
LDC-L4ST	76	110	7	75

It was previously proven that LDC enhanced the catalytic activity of the anode. In addition, the presence of LDC nano-particles (5-20 nm) improved the particle distribution of L4ST into the porous structure which enhanced the triple phase boundary for electrochemical reactions of fuels. The peak power densities of the cell was also improved when H_2S (0.5%)-containing H_2 fuelled the cells with L4ST and LDC-L4ST as the anode materials when compared with pure H_2. In

contrast, the cell with LDC as the anode material was poisoned in the presence of H_2S with the peak power density droping from 50 $mW.cm^{-2}$ to 25 $mW.cm^{-2}$. However, the addition of H_2S (0.5%) improved the electrochemical oxidation of CH_4 regardless of the anode material.

The L4ST is necessary for improving the stability of the cell against the poisoning effect of high concentration H_2S-containing feeds. The same power density improvements were obtained for L4ST containing anodes in the presence of high concentration of H_2S when either syngas or methane fed the cell [121,122]. The production of CO_2 was enhanced and no H_2S consumption was detected when H_2S was added into these feeds, indicating that the electrochemical oxidation of H_2S was not the main source of power improvement [121,122].

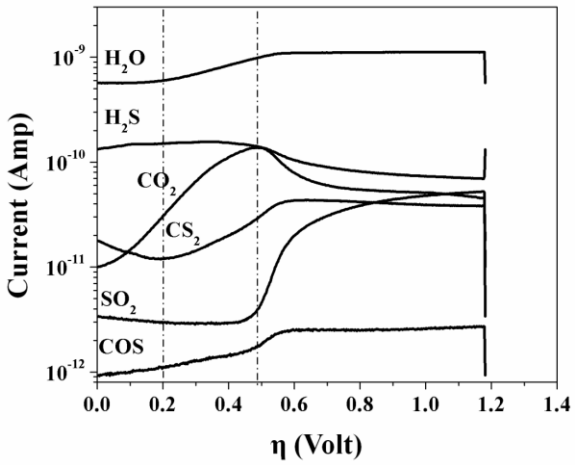

Figure 4. 7 Mass spectroscopy of the outlet vs. overpotential of the cell when H_2S (0.5)-CH_4 fuelled the cell containing LDC-L4ST anode material at 800 °C (0.2 $mV.s^{-1}$).

4.3.4 Mass spectroscopy

Figure 4.7 shows the mass spectrometry analyses for the outlet gas of cells with LDC-L4ST anode material fed by H_2S (0.5%)-CH_4 fuel. CO_2 production started first before H_2O released

and its production increased by increasing the polarization of the cell away from OCV (~1.2 V) to the highest production rate that occurred at 0.5 V of polarization. Further polarization led to lower CO_2 production which showed the lower electrochemical oxidation rate of CH_4. H_2O production started after 0.2 V of polarization which increased up to 0.5 V of polarization reaching a plateau till the end of the run. H_2S was another gas species included in the feed. The result showed that H_2S level was almost constant with no SO_2 production for polarization voltages lower than 0.5 V of polarization and a slight increase till 0.2 V of polarization. SO_2 production and H_2S consumption occurred after 0.5 V of polarization, the same potential with maximum CO_2 production. The results showed that the concentration of CS_2 decreased after running the cell up to 0.2 V of overpotential. Then it increased by increasing the overpotential up to 0.55 V and reached a plateau. COS with very low concentration was detected. Increasing the overpotential produced more COS up to 0.55 V where its concentration became constant. Different reaction paths could be followed to predict the possible reaction mechanisms to rationalized these observations. In order to explain these observations three regions were specified: region I (OCV to 0.2 V of polarization), region II (0.2 V to 0.5 V of polarization) and region III (0.5 V to 1.2 V of polarization). All possible reaction paths are shown in table 4.2.

Region I.

The surface of the catalyst was fully covered by sulfur species from thermally dissociated H_2S into sulfur species (reaction 1) including: HS, S and/or H at OCV. Besides, CH_4 can be thermally decomposed forming C and H_2 (reaction 4) resulting in coverage of the catalyst with carbon species. Consequently the surface of the catalyst was covered with sulfur and carbon species

which were ready to react. In addition, CH_4 could directly react with H_2S (Reaction 1) or S (Reaction 2) to produce CS_2 and H_2 as the by-products. C can also react with S from decomposition of H_2S to form CS_2 (reaction 5). Applying the potential oxidized the available C on the surface of the catalyst to produce CO_2 (reaction 6) which occurred before the electrochemical oxidation of CH_4 (reactions 7, 8) and/or H_2 (reaction 9). In this region, production of H_2O as the electrochemical oxidation of H_2 could not be observed because of its reaction with S (reaction 10), CS_2 (reactions 11, 12) and methane (reaction 13) which are thermodynamically viable at 800 °C. Reactions 10, 11 and 12 led the overall reaction path towards the production of H_2S which supports the slight increase in the H_2S responses and CS_2 consumption as well. In addition, CS_2 can be directly oxidized to produce CO_2 and remain S on the surface (reaction 14). Adrien et al. [122] reported that the CS_2 was a fuel, resulting in a peak power density around 6 $mW.cm^{-2}$ at 850 °C when its concentration was 200 ppm balanced with argon with no SO_2 production detected up to 0.5 V of polarization.

Region II.

In the second region, from 0.2 V to 0.5 V of polarization, H_2O production appeared and CS_2 production increased. H_2S line slightly changed and still no SO_2 production occurred. CO_2 production still increased and reached its maximum production rate at 0.5 V of polarization. As the electrochemical reaction moved towards the higher current (from 12 $mA.cm^{-2}$ to 90 $mA.cm^{-2}$), flux of oxygen increased which enhanced the electrochemical oxidation of CH_4 and also increased its cracking to C and H on the surface of the catalyst [79]. As a result, the production of H_2O and CO_2 as by-products of this reaction enhanced. In addition, CH_4 becomes more active

to react with sulfur to produce CS_2 and H_2 (reaction 2), later can be oxidized again to produce H_2O (reaction 9). In this region, the partial electrochemical oxidation of H_2S can produce H_2O and S (reaction 14). The surface of the catalyst is covered by sulfur species. In fact, the flux of oxygen was not enough to completely oxidize H_2S (reaction 15) and/or S (reaction 16) on the surface of the catalyst [151]. Consequently, the electrochemical oxidation of methane can be helped by producing intermediate species on the surface of the catalyst which can be easily oxidized compared to pure methane. Slight electrochemical oxidation of H_2S also can be compensated towards reaction 3 and/or reaction 17 for respective reactions of SO_2 with CH_4 and S with H_2O compensating the consumption of H_2S.

Table 4. 2 Possible chemical and electrochemical reactions with standard Gibbs free energy

No	Reaction	ΔG^0 ($KJ.mol^{-1}$)
1	$CH_4+2H_2S=CS_2+4H_2$	30.19
2	$CH_4+2S=CS_2+2H_2$	-348.82
3	$H_2O+S=H_2S$	-189.5
4	$CH_4=C+2H_2$	-27.1
5	$C+S_2=CS_2$	-17.8
6	$C+2O^{2-}=CO_2+4e^-$	-
7	$CH_4+4O^{2-}=CO_2+2H_2O+8e^-$	-
8	$CH_4+3O^{2-}=CO+2H_2O+6e^-$	-
9	$H_2+O^{2-}=H_2O+2e^-$	-
10	$H_2O+CS_2=COS+H_2S$	-47.7
11	$CS_2+2H_2O=2H_2S+CO_2$	-75.8
12	$CH_4+H_2O=CO+3H_2$	-45.2
13	$CS_2+2O^{2-}=CO_2+2S+4e^-$	-
14	$H_2S+O^{2-}=H_2O+S+2e^-$	-
15	$H_2S+3O^{2-}=H_2O+SO_2+6e$-	-
16	$S+2O^{2-}=SO_2+4e^-$	-
17	$SO_2+CH_4=H_2S+CO_2+H_2$	-177.1

Region III.

In the last region, with 0.5 V overpotential and 90 $mA.cm^{-2}$ current density, the SO_2 production occurred, resulting in H_2S consumption (reactions 15, 16). H_2O production remained constant and CO_2 production suddenly dropped and became stable after 0.8 V of polarization. CS_2 production also became stable, slightly dropped at 0.55 V of polarization after CO_2 production. In this region, current is high enough (90 $mA.cm^{-2}$ to 95 $mA.cm^{-2}$) to oxidize available sulfur species on the surface of the catalyst. Consequently, part of the sulfur species for CH_4 oxidation is removed which decreased its electrochemical oxidation, resulting in lower CO_2 production. At the same time, equilibrium can occur between production of CS_2 (reaction 2) and its consumption either electrochemically or chemically towards reaction 11 and reaction 13, respectively.

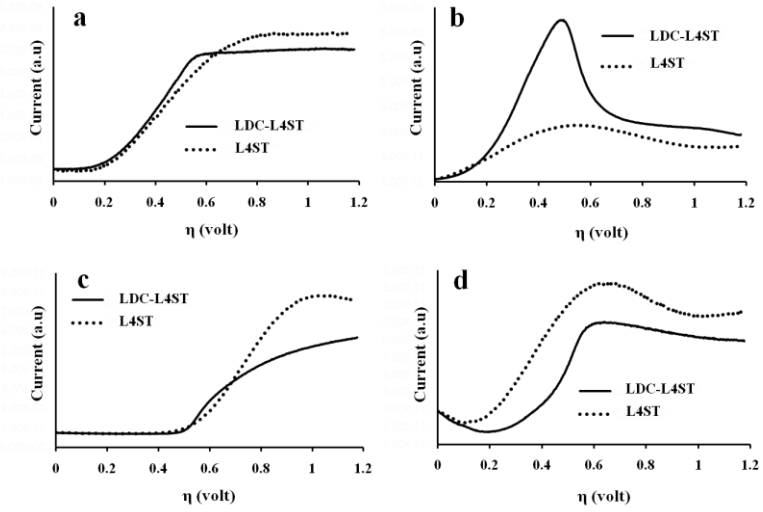

Figure 4. 8 Mass spectroscopy results of the outlet gas during potentiodynamic tests with 0.2 $mV.s^{-1}$ scan rate for : (a) H_2O, (b) CO_2, (c) SO_2, (d) CS_2 using L4ST and LDC-L4ST anode materials when H_2S (0.5%)-containing CH_4 fuelled the cells at 800 °C.

Figure 4.8 compares the different gas productions from the anode chamber of SOFCs when LDC-L4ST and LST were used as the anode materials. The H_2O production was slightly higher for the latter cell (Figure 4.8(a)). The production of CO_2 was significantly enhanced using LDC-L4ST as the anode material when compared to L4ST alone (Figure 4.8(b)). Production of SO_2 Figure 4.8(c) and CS_2 (Figure 4.8(d)) also were improved when LDC was co-impregnated with L4ST. SO_2 production occurred after 0.5 V for both samples. These results showed the effective role of LDC on electrochemical oxidation of CH_4 in the first and second regions of the electrochemical reactions where the electrochemical oxidation of H_2S and sulfur species did not start yet. Cerium based oxide materials are known as highly active catalysts toward oxidation of hydrocarbons [152,153]. They are also very active toward H_2S adsorption by forming an oxysulfide phase [154–156], which can be proven by the high production of SO_2 in the last region of the reaction for SOFCs with L4ST-LDC anode material (Figure 4.8(c)). In fact, the presence of more active sulfur species on the surface of the anode catalyst improved the electrochemical oxidation of CH_4. In contrast, in the last region of the reaction, sulfur species were oxidized. Consequently, the production of CO_2 decreased almost to the same level as observed for the cell using L4ST as the anode material.

4.3.5. Conductivity measurement

The conductivity (σ) of the porous YSZ structure without impregnated deposits was measured to be 0.01 $S.cm^{-1}$ at 900 °C in air (Figure 4.9(a)). This value dropped down to 6 $mS.cm^{-1}$ for LDC and 3 $mS.cm^{-1}$ for LDC-L4ST impregnated structures. L4ST with the perovskite structure has

low ionic conductivity when compared to other ion conductive materials for SOFC including YSZ, LSGM and cerium based structures [59,149,157]. In addition, impregnated particles are loosely connected to each other because of their lower sintering temperature (900 °C) when compared to the YSZ structure prepared at 1200 °C. Consequently, the ionic conductivities of the impregnated samples are lower than that of the main porous YSZ. Figure 4.9(b) compares the conductivities of these structures in reducing atmosphere (H_2). The results showed that the conductivity of the porous YSZ in H_2 had the same values (0.01 $S.cm^{-1}$) in air. The conductivity of the LDC impregnated porous YSZ slightly reduced from 6 $mS.cm^{-1}$ to 5 $mS.cm^{-1}$, indicating that LDC behaved the same manner as YSZ. The L4ST containing sample became more conductive in reducing environment which had 0.07 $S.cm^{-1}$ at 900 °C. The same conductivity improvement was observed for LDC-L4ST containing deposits, with the specific conductivity of 0.04 $S.cm^{-1}$ in H_2 at 900 °C. L4ST is an n-type semiconductor with higher conductivity in reducing atmosphere because of reducing of Ti^{4+} ions into Ti^{3+} which leaves electrons in the conduction band of the structure. Figure 4.9(c) compared the total conductivities of YSZ structure, LDC, L4ST and LDC-L4ST impregnated structures after exposure to H_2S (0.5%)-H_2. The conductivity of the YSZ structure was similar, with the value of 0.01 $S.cm^{-1}$, showing H_2S did not affect the conductivity of YSZ. The conductivity of LDC impregnated porous YSZ remained constant after changing H_2 to H_2S (0.5%)-H_2. In contrast, the total conductivities of the L4ST-containing materials were significantly improved at the presence of H_2S (0.5%), that were 0.14 $S.cm^{-1}$ and 0.078 $S.cm^{-1}$ for L4ST and LDC-L4ST at 900 °C, respectively. Their conductivities were improved by two orders of magnitude when compared to these in H_2. It has

been proven that the presence of high concentrations of H_2S did not change the structure of L4ST [122]. Consequently, adsorption of H_2S on L4ST could be the key for such a conductivity improvement. Conductivity variation in the presence of H_2S showed the interaction of either H_2S or sulfur species with L4ST surface. The same scenario was reported for the interaction of TiO_2 with H_2S (3%) which changed its conductivities in several steps [158]. L4ST is an n-type semiconductor, such that its electronic conductivity improves by donating an electron into its conduction bands. H_2S is an electron donor, could enhance the electronic conductivity of L4ST donating an electron into its conduction band. It also could be possible that sulfur interact with oxygen vacancies available on the surface and fills them, followed by forming SO_2 and leaving more oxygen vacancies which increased the reducibility of the structure and increases its conductivity. Replacing oxygen vacancies by sulfur on the surface of the L4ST might also be a reason for improving the catalytic activity toward oxidation of the feed.

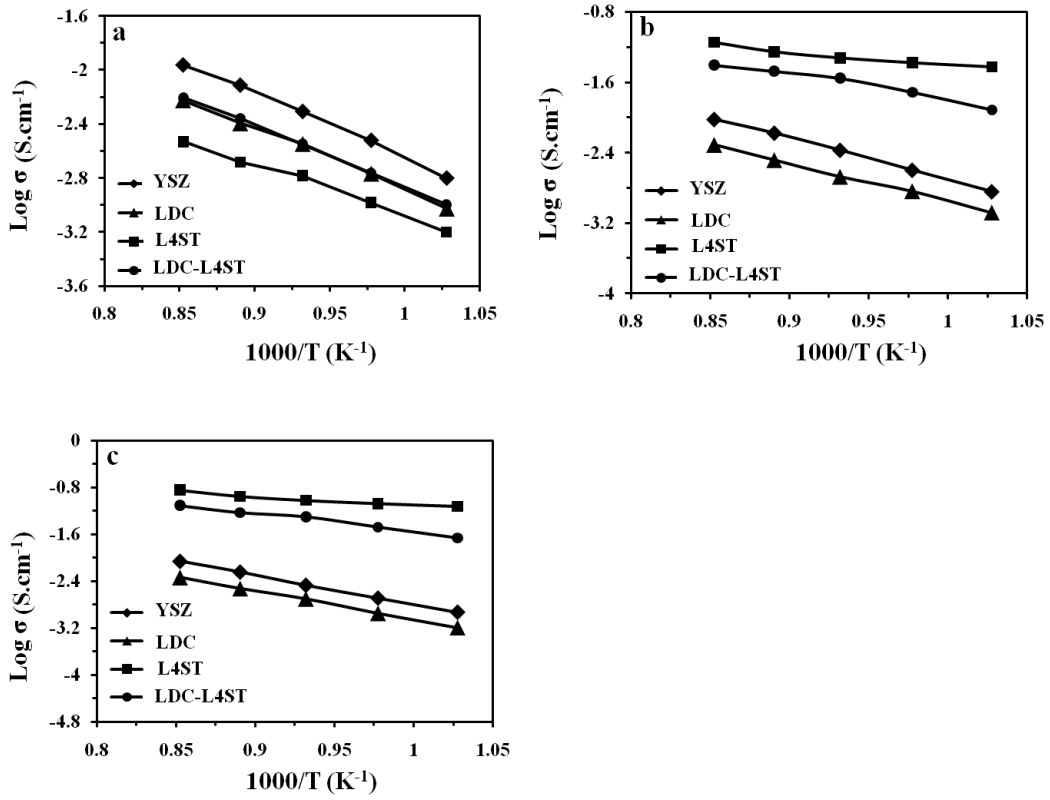

Figure 4. 9 4-point conductivity measurement results for YSZ, LDC, L4ST and LDC-L4ST samples in different atmospheres: (a) Air, (b) H_2, (c) H_2S (0.5%)-H_2 at different temperatures between 700 °C and 900 °C.

4.3.6 Electrochemical stability tests

In order to investigate the activation, deactivation and recovery of the cell, galvanostatic tests were performed for the cell containing LDC-L4ST as the anode material while the potential of the cell was recorded vs. Pt/air reference electrode. Figure 4.10(a) shows the variation of overpotential with time when the feed changed from H_2 to H_2S (0.5%)-H_2. The overpotential of the cell decreased from 286 mV to 270 mV after addition of H_2S (0.5%) into the H_2 feed. The

potential of the cell remained stable after 30 min exposure. Then the feed switched back to H_2 with a fast recovery of the overpotential to 270 mV. The same procedure was followed for H_2S (0.5%)-CH_4 at 800 °C (Figures 4.10(b)). The overpotential of the cell increased from 190 mV to 470 mV when the feed changed from H_2 to H_2S (0.5%)-CH_4 with a stability over 1 h exposure. It was expected that the oxidization activity of CH_4 was considerably lower than hydrogen. However, addition of high concentration H_2S significantly improved the oxidization activity when compared to pure CH_4. The cell showed deactivation after exposure to H_2S (0.5%)-CH_4, but the fast recovery occurred after switching the feed to H_2.

These results proved that the effect of H_2S and CH_4 on the anode catalyst are reversible and no permanent activation or deactivation happened by feeding the cell with either high concentrations H_2S or CH_4. Activation of the cell after addition of H_2S (0.5%) could be related to the surface interaction of H_2S with the catalyst surface which improved the oxidation of the fuel, presumably by the presence of sulfur active species on the surface of the catalyst (LDC and L4ST). This surface interaction could be a strong chemical adsorption of sulfur species which can permanently change the surface properties of the catalyst [158]. However, no phase change was observed when L4ST was exposed to high concentration H_2S-containing feeds. In contrast, LDC was not chemically stable when exposed to H_2S (0.5%)-containing feeds showing the appearance of cerium oxysulfide based phase. It might be the reason for electrochemical instability of the cell with LDC as the anode catalyst fed by H_2S (0.5%)-containing H_2 when compared to H_2. In contrast, the presence of LDC along with L4ST did not show any electrochemical deactivation and instability during exposure to H_2S (0.5%)- H_2. The presence of

L4ST as a part of the anode catalyst might help the stability of the other components (LDC) toward poisonous effect of high concentrations of H_2S.

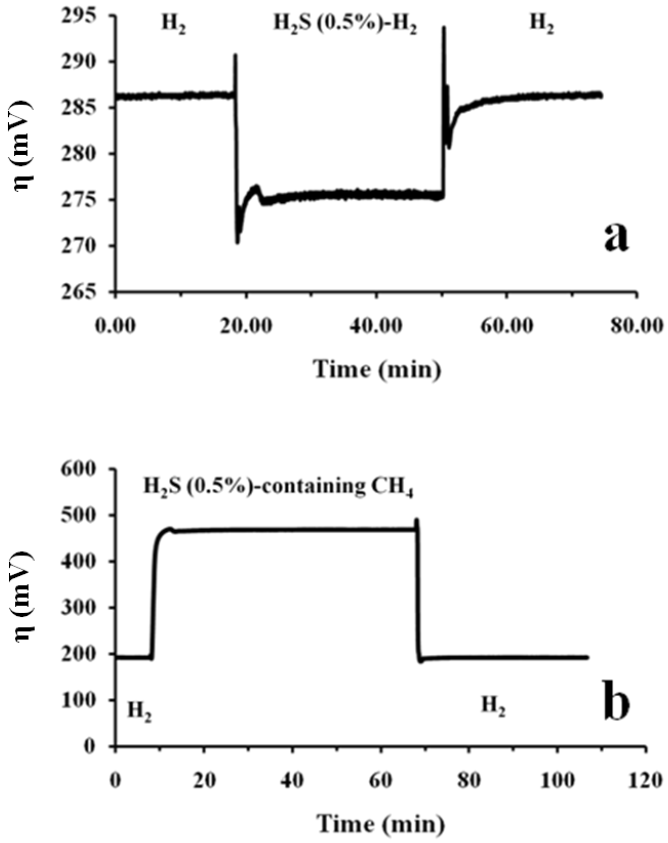

Figure 4. 10 Overpotential variations vs. time during galvanostatic stability tests (40 mA) when the feed switched from H_2 to (a) H_2S (0.5%)-H_2, (b) H_2S (0.5%)-CH_4 at 800 °C.

4.3.7 TPO analysis

Figure 4.11 compares the carbon deposition of the L4ST and LDC-L4ST anode materials after the cells exposure to H_2S (0.5%)-containing CH_4 at 800 °C under 0.7 V potentiostatic run for 20 h. A large peak of CO_2 release was observed at about 600 °C in the TPO curves for the L4ST anode material. The presence of carbon was a concentration of 1.1 mmol.g^{-1} of the L4ST anode material, while there was no obvious peak of CO_2 release for the LDC-L4ST anode material, showing the effective role of LDC on carbon deposition prevention.

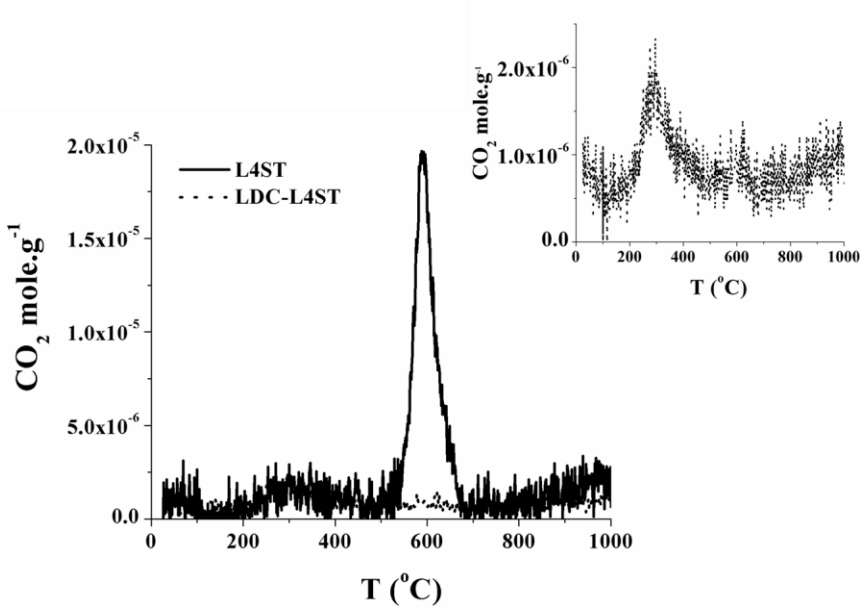

Figure 4. 11 TPO of the cells containing L4ST and LDC-L4ST anode materials after exposure to H_2S (0.5%)-CH_4 under 0.7 V potentiostatic run at 800 °C for 20 h.

4.4. Conclusions

LDC-L4ST was impregnated into a porous YSZ structure and successfully used as the anode material for SOFC fed by H_2S (0.5%)-containing H_2 and CH_4. The electrochemical tests revealed the effective role of high concentrations H_2S on the feed oxidation activation, especially when CH_4 fed the cell. This significant improvement was assigned for the catalytic activity of the sulfur species on the surface of the anode catalyst, which was observed using mass spectroscopy analysis. No SO_2 production and net H_2S consumption was observed for the overpotential lower than 0.5 V along with a CO_2 and H_2O production increase. The production of SO_2 was detected after 0.5 V overpotential. In this region, the CO_2 production reduced and the H_2O production became stable, showing the mass transfer effect which prevents the electrochemical oxidation of the CH_4. In addition, the conductivity improvement of the anodes containing L4ST in H_2S (0.5%)-containing H_2 revealed the strong interaction of H_2S and sulfur species with the catalyst surface, that can be responsible for such a catalytic activity improvement at the presence of H_2S at high operating temperatures (800 °C to 900 °C). The galvanostatic tests showed that the cell with LDC-L4ST as the anode material is stable after addition of H_2S into the feed with the fast recovery by switching to H_2. The presence of LDC along with L4ST in the anode structure improved the electrochemical stability of the cell and significantly reduced the carbon deposition during a potentiostatic run (0.7 V) at 800 °C after 20 h of operating.

4.5. References

[1] F. Alcaide, P.-L. Cabot, E. Brillas, Journal of Power Sources 153 (2006) 47–60.

[2] K. Eguchi, H. Kojo, T. Takeguchi, R. Kikuchi, K. Sasaki, Solid State Ionics 152–153 (2002) 411–416.

[3] S.P. Jiang, S.H. Chan, Journal of Materials Science 39 (2004) 4405–4439.

[4] T. Setoguchi, K. Okamoto, K. Eguchi, H. Arai, J. Electrochem. Soc. 139 (1992) 2875–2880.

[5] B.C.H. Steele, Solid State Ionics 86-88 (1996) 1223–1234.

[6] O.. Marina, L.. Pederson, In: J. Huijsmans, Editor, Fifth European Solid Oxide Fuel Cell Forum, European Fuel Cell Forum, Oberrohfdorf, Switzerland (2002) 481–489.

[7] R. Mukundan, E.L. Brosha, F.H. Garzon, Electrochem. Solid-State Lett. 7 (2004) A5–A7.

[8] S. Jiang, S. Chan, MATERIALS SCIENCE AND TECHNOLOGY 20 (2004) 1109–1118.

[9] T. Iida, M. Kawano, T. Matsui, R. Kikuchi, K. Eguchi, Journal of The Electrochemical Society 154 (2007) B234–B241.

[10] D. Mogensen, J.-D. Grunwaldt, P.V. Hendriksen, K. Dam-Johansen, J.U. Nielsen, Journal of Power Sources 196 (2011) 25–38.

[11] A. Cantos-Gómez, R. Ruiz-Bustos, J. van Duijn, Fuel Cells 11 (2011) 140–143.

[12] Y. Nabae, I. Yamanaka, Applied Catalysis A: General 369 (2009) 119–124.

[13] S.-I. Lee, K. Ahn, J.M. Vohs, R.J. Gorte, Electrochemical and Solid-State Letters 8 (2005) A48–A51.

[14] S. McIntosh, J.M. Vohs, R.J. Gorte, Electrochemical and Solid-State Letters 6 (2003) A240–A243.

[15] H. Sumi, K. Ukai, Y. Mizutani, H. Mori, C.-J. Wen, H. Takahashi, O. Yamamoto, Solid State Ionics 174 (2004) 151–156.

[16] N. Lakshminarayanan, U.S. Ozkan, Applied Catalysis A: General 393 (2011) 138–145.

[17] K. Sasaki, K. Susuki, A. Iyoshi, M. Uchimura, N. Imamura, H. Kusaba, Y. Teraoka, H. Fuchino, K. Tsujimoto, Y. Uchida, N. Jingo, J. Electrochem. Soc. 153 (2006) A2023–A2029.

[18] C.M. Grgicak, J.B. Giorgi, The Journal of Physical Chemistry C 111 (2007) 15446–15455.

[19] M. Gong, X. Liu, J. Trembly, C. Johnson, Journal of Power Sources 168 (2007) 289–298.

[20] Y. Matsuzaki, I. Yasuda, Solid State Ionics 132 (2000) 261–269.

[21] H. He, R.J. Gorte, J.M. Vohs, Electrochem. Solid-State Lett. 8 (2005) A279–A280.

[22] Y.M. Choi, C. Compson, M.C. Lin, M. Liu, Chemical Physics Letters 421 (2006) 179–183.

[23] S. Zha, P. Tsang, Z. Cheng, M. Liu, Journal of Solid State Chemistry 178 (2005) 1844–1850.

[24] X.J. Chen, Q.L. Liu, S.H. Chan, N.P. Brandon, K.A. Khor, J. Electrochem. Soc. 154 (2007) B1206–B1210.

[25] A.L. Vincent, J.-L. Luo, K.T. Chuang, A.R. Sanger, Applied Catalysis B: Environmental In Press, Accepted Manuscript (n.d.).

[26] M. Roushanafshar, J.-L. Luo, A.L. Vincent, K.T. Chuang, A.R. Sanger, International Journal of Hydrogen Energy (n.d.).

[27] L. Aguilar, S. Zha, Z. Cheng, J. Winnick, M. Liu, Journal of Power Sources 135 (2004) 17–24.

[28] J.N. Kuhn, N. Lakshminarayanan, U.S. Ozkan, Journal of Molecular Catalysis A: Chemical 282 (2008) 9–21.

[29] Z. Cheng, J.-H. Wang, Y. Choi, L. Yang, M.C. Lin, M. Liu, Energy Environ. Sci. 4 (n.d.) 4380–4409.

[30] K. Haga, S. Adachi, Y. Shiratori, K. Itoh, K. Sasaki, Solid State Ionics 179 (2008) 1427–1431.

[31] H. Kurokawa, L. Yang, C.P. Jacobson, L.C. De Jonghe, S.J. Visco, Journal of Power Sources 164 (2007) 510–518.

[32] L. Aguilar, S. Zha, S. Li, J. Winnick, M. Liu, Electrochemical and Solid-State Letters 7 (2004) A324–A326.

[33] O.A. Marina, L.R. Pederson, J. Huijsmans (Ed), Proceedings of the 5th European Solid Oxide Fuel Cell Forum, Lucerne, Switzerland (2002) 481.

[34] O.A Marina, Presented at SECA Core Technology Program Review Meeting, Boston, MA (2004).

[35] O.A. Marina, N.L. Canfield, J.W. Stevenson, Solid State Ionics 149 (2002) 21–28.

[36] S. Tao, J.T.S. Irvine, Nat Mater 2 (2003) 320–323.

[37] B.F. Flandermeyer, A.K. Agarwal, H.U. Anderson, M.M. Nasrallah, J Mater Sci 19 (1984) 2593–2598.

[38] S.A. Howard, J.K. Yau, H.U. Anderson, J. Appl. Phys. 65 (1989) 1492.

[39] D. Neagu, J.T.S. Irvine, Chemistry of Materials 22 (2010) 5042–5053.

[40] P.R. Slater, D.P. Fagg, J.T.S. Irvine, J. Mater. Chem. 7 (1997) 2495–2498.

[41] J. Canales-Vázquez, M.J. Smith, J.T.S. Irvine, W. Zhou, Adv. Funct. Mater. 15 (2005) 1000–1008.

[42] J.C. Ruiz-Morales, J. Canales-Vázquez, C. Savaniu, D. Marrero-López, W. Zhou, J.T.S. Irvine, Nature 439 (2006) 568–571.

[43] A. Vincent, J.-L. Luo, K.T. Chuang, A.R. Sanger, Journal of Power Sources 195 (2010) 769–774.

[44] O.A. Marina, M. Mogensen, Applied Catalysis A: General 189 (1999) 117–126.

[45] I.V. Yentekakis, C.G. Vayenas, Journal of The Electrochemical Society 136 (1989) 996–1002.

[46] N. Laosiripojana, S. Assabumrungrat, Applied Catalysis B: Environmental 60 (2005) 107–116.

[47] E. Ramírez-Cabrera, A. Atkinson, D. Chadwick, Applied Catalysis B: Environmental 36 (2002) 193–206.

[48] R.M. Ferrizz, R.J. Gorte, J.M. Vohs, Applied Catalysis B: Environmental 43 (2003) 273–280.

[49] Z. Wang, M. Flytzani-Stephanopoulos, Energy Fuels 19 (2005) 2089–2097.

[50] H.-T. Chen, Y. Choi, M. Liu, M.C. Lin, J. Phys. Chem. C 111 (2007) 11117–11122.

[51] M.E. Bowden, D.A. Jefferson, I.W.M. Brown, Journal of Solid State Chemistry 117 (1995) 88–96.

[52] T. Ishihara, Bulletin of the Chemical Society of Japan 79 (2006) 1155–1166.

[53] C. Yanxin, J. Yi, L. Wenzhao, J. Rongchao, T. Shaozhen, H. Wenbin, Catalysis Today 50 (1999) 39–47.

Chapter 5

Conclusions, recommendations and future work

In this thesis, the potential of different anode materials for electrochemical oxidation of H_2S (0.5%)-containing fuel was investigated. Different electrochemical and chemical analyses were employed to study the effect of H_2S on the performance, activity and stability of the cell. Moreover, the effect of H_2S presence on the electrochemical oxidation of feeds was studied using mass spectroscopy and chromatograph gas analyses.

In chapter 2, a composite of LST and YDC was used as the anode material when H_2S (0.5%)-containing syngas fed the cell. The results showed that the electrochemical oxidation of the feed components enhanced by the presence of H_2S (0.5%) when compared to H_2S free syngas feed. However, oxidation of H_2S did not occur over a wide potential range and no SO_2 production was observed. The electrochemical stability of the cell was examined under potentiostatic run for 75 h, with no cell degradation being observed. In addition, the performance of the cell returned to the value before the presence of H_2S when the feed was switched back to H_2S free syngas.

In chapter 3, a novel anode material was developed by means of an impregnation method. A porous YSZ structure with the average porosity of 70 vol.% was prepared. Different amounts of L4ST and LDC were impregnated into this porous structure using wet chemical method. The effect of different impregnation loading and composition on the electrochemical performance of

the cell was studied. In addition, the effect of LDC inclusions on the particle size distribution of the L4ST was studied using SEM and TEM analyses. The results showed the effective role of LDC inclusions on the performance enhancement of the cell when hydrogen was purging the cell. Moreover, the microscopy results revealed that the L4ST deposits were broken down into finely distributed particles after impregnation of LDC.

Chapter 4 was dedicated to the analysis of the effect of the presence of H_2S (0.5%) presence in hydrogen and methane using impregnated LDC-L4ST anode material (prepared in chapter 3). The performance of the cell was enhanced by the presence of H_2S (0.5%) in the feed when compared to the H_2S free feed. The mass spectroscopy analysis of the effluent gas revealed three regions for electrochemical oxidation of methane over different cell overpotentials. In region I and region II, the oxidation of the H_2S does not occur, while the oxidation of methane increases with overpotential. After 0.5 V, the electrochemical oxidation of H_2S occurs, resulting effluent of SO_2 (Region III). In this region, the production of CO_2 decreases and the H_2O signal reaches a plateau, indicating a drop in methane oxidation. The electrical conductivity of the anode structure was measured using 4-point probe. The result showed that the conductivity of the cell increased by two folds at the presence of H_2S (0.5%) in hydrogen feed.

Materials development of anode has been highly demanded for extending the application of SOFCs through using a wide range of available fuels. This study showed that the L4ST anode material would be a promising candidate for high concentration H_2S containing fuels; however, its catalytic activity needs to be improved. L4ST based materials do not offer high catalytic

activity towards fuel which would be related to their packed crystal structures. In addition, their negligible ionic conductivity is another challenging issue in front of catalytic activity improvement. Addition of other elements on the A site and B site would be one of the key points for developing an active anode material which needs to be taken into account especially in the high concentration H_2S fuels where the poisonous effect of such impurities may has an adverse effect on the stability of the structure. Furthermore, addition of other active catalysts into the anode would be another solution for improving the total catalytic activity and ionic conductivity of the anode. We showed that the presence of cerium based catalysts including YDC and LDC significantly improved the performance of the cell, not only in the presence of pure fuel but also and most importantly in the presence of high concentration of H_2S (0.5%) in the feed. It would be interesting to examine the effect of other active materials including Ni on the activity of the L4ST and investigate its stability toward electrochemical oxidation of the H_2S-containing fuels. Different concentrations of hydrogen sulfide can be investigated.

There are several recommendations for further research in this area including:

- Doping different elements on the A site and B site of the LST in order to improve its catalytic activity toward the electrochemical oxidation of feed.
- Study the effect of different dopants on the electrical conductivity of the LST in the presence of H_2S.
- Study the effect of dopant and H_2S addition on the ionic and electronic conductivities of the LST, using an appropriate method to separate these two parameters.

- Investigate the effect of different cerium oxide based catalysts on the performance, stability and feed oxidation.
- Study the surface interaction of the feed with anode materials in the presence of H_2S using precise characterization methods, such as XPS and Raman.
- Study the effect of anode microstructure on the performance and stability of the cell using different approaches including: adjusting porosity, sintering temperature, electrode thickness, etc.

Appendix A

Impedance circuit

All impedances results were fitted based on a model including ohmic resistance of the cell, capacitance and resistance in parallel representing different chemical and electrochemical reactions (Figure A1). The total polarization resistance of the cell was calculated by the summation of the all the resistances in the circuit except ohmic resistance of the cell (Equation A1):

$$R_{pol} = \sum_1^n R_n = R_1 + R_2 + \cdots + R_n \qquad (A.1)$$

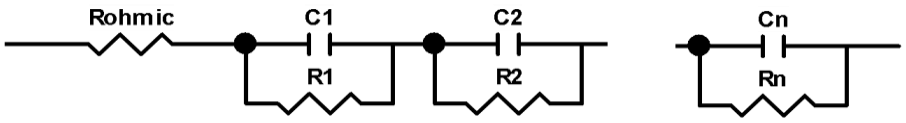

Figure A 1. Equivalent circuit for fitting EIS curves

In order to make the fitting calculations simple, it can be assumed that two reaction paths are included in the circuit (Figure A2), one related to the charge transfer electrochemical reaction and the other can be assigned to either the adsorption-desorption phenomena between fuel, reaction products and catalyst surface or diffusion of the reactants toward or products away from the reaction sites at the triple phase boundaries.

The ohmic resistance of the cell was measured using intersect of the impedance curve with the x-axis where Zimg equals to zero at high frequencies. The total polarization resistance was measured by the subtraction of the total impedance of the cell where the impedance curve

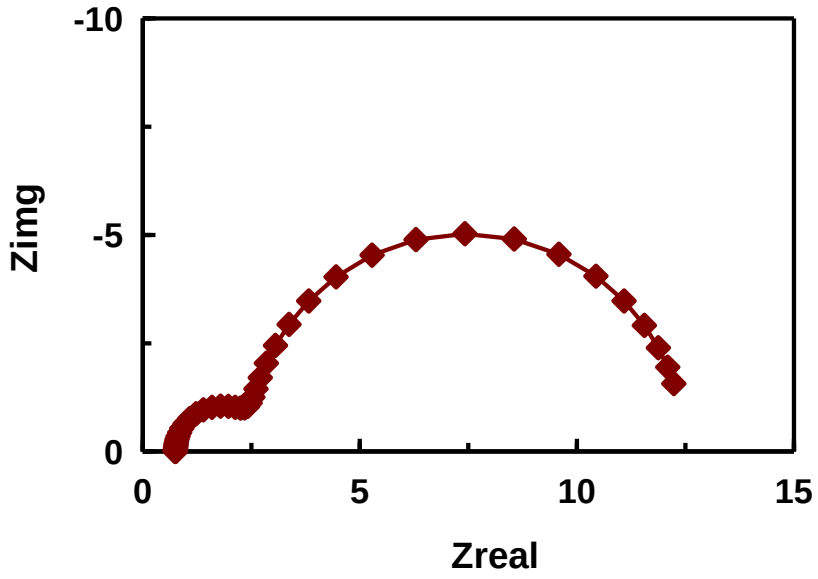

Figure A 2. EIS fitting curve for a electrochemical circuit containing two reaction paths.

intersects the x-axis at low frequency and the ohmic resistance of the cell. In most of the EIS results, the impedance curves do not intersect the x-axis at low frequencies. In these cases, the total impedances of the cells were calculated by the extrapolation of the curves using the equivalent circuit.